# Angular Analysis of $B \rightarrow K^{*}l^{+}l^{-}$ using the *BABAR* Detector

*A thesis submitted to the University of Edinburgh*
*for the degree of Doctor of Philosophy*
*in the College of Science and Engineering*

2010

**Jennifer Elizabeth Watson**

Particle Physics Experiment Group

# Contents

# List of Tables

# List of Figures

# Abstract

The decay $B \to K^{*}l^{+}l^{-}$, where the $l^{+}l^{-}$ can be $e^{+}e^{-}$ or $\mu^{+}\mu^{-}$, resulting from the $b \to s$ flavour changing neutral current decay is highly sensitive to the presence of new physics.

The angular observables describing the $K^{*}$ polarisation ($F_L$) and the forward backward asymmetry ($A_{FB}$) are first measured in two regions of di-lepton mass squared using a dataset of 384 million $B\overline{B}$ pairs collected by the BABAR detector on the PEP-II rings at SLAC. A second measurement was made in four regions of di-lepton mass squared using a dataset of 468 million $B\overline{B}$ pairs.

# Declaration

No portion of the work referred to in this thesis has been submitted in support of an application for another degree or qualification of this or any other university or other institute of learning.

Jennifer Elizabeth Watson
School of Physics and Astronomy
The University of Edinburgh
July 2009

*To my family.*

# Introduction

About fourteen billion years ago the universe was created in a big bang that produced equal amounts of matter and antimatter, whereas the universe that exists today consists almost entirely of matter. “Why do we live in a matter dominated universe?” and “What gives a particle mass?” are two basic questions that have provoked scientists to probe the universe around us. Particle physics is the study of the fundamental particles and their interactions that aims to answer these questions. The current theory used to describe particle physics is the Standard Model (SM), however, it is known that this is an incomplete theory and that New Physics (NP) must exist. Throughout the last 100 years we have built increasingly sophisticated experiments to probe the foundations of matter with the hope of discovering the secrets of the universe.

The *BABAR* experiment based at the Stanford Linear Accelerator Centre (SLAC) was designed to study the $B$ meson sector, where the decays of heavy $b$ quarks allow precision tests of the SM to be made. The PEP-II collider is an $e^+e^-$ collider that operates at a centre-of -mass energy of 10.58 GeV corresponding to the $\Upsilon(4S)$ resonance, that decays almost exclusively to $B\overline{B}$ pairs. The decay $B \to K^*l^+l^-$ resulting from the $b \to s$ flavour changing neutral current decay, is forbidden to occur at the tree level in the SM, however they can occur via loop diagrams. These decays are sensitive to NP particles that can enter the loop and enhance the SM predictions.

Angular observables such as the lepton forward-backward asymmetry ($A_{FB}$) and the fraction of longitudinal $K^*$ polarisation ($F_L$) have precise SM predictions. This thesis will present results for two analyses that measure $A_{FB}$ and

$F_L$. The first analysis will be referred to as the "Run 5" analysis, where measurements were made in two bins of di-lepton mass using a dataset of 384 million $B\overline{B}$ pairs collected by the BABAR detector. The second analysis will be referred to as the "Run 6" analysis, where measurements were made in four bins of di-lepton mass squared using the full $\Upsilon(4S)$ dataset of 468 million $B\overline{B}$ pairs. These analyses are "blind" meaning that the $B \rightarrow K^{*}l^{+}l^{-}$ data was not studied until the final fitting technique and event selection had been established. This must pass review by the BABAR Collaboration before the $B \rightarrow K^{*}l^{+}l^{-}$ data can be analysed. This method prevents human bias from entering the final measurement.

This thesis is structured as follows: Chapter 1 is an introduction to the Standard Model, with special reference to the angular measurements in the $B \rightarrow K^{*}l^{+}l^{-}$ decay; Chapter 2 describes the PEP-II collider and the BABAR detector; Chapter 3 describes the event selection for both the Run 5 and Run 6 analyses; Chapter 4 describes the fitting technique for the Run 6 analysis; Chapter 5 describes the validation of the Run 6 analysis; Chapter 6 describes the validation of the Run 5 analysis, presents the results for this analysis and discusses the associated systematic errors; Chapter 7 presents the results for the Run 6 analysis and the associated systematic errors; Chapter 8 summarises the Run 5 and Run 6 results, compares them to the recent experimental measurements from Belle and CDF and summarises predicted results from future and current experiments; and finally the Appendix contains supplementary plots and figures.

The author was based at SLAC for a two year period, where as a member of the BABAR collaboration she performed two service tasks. For a period of six months she was an electronics expert for the electromagnetic calorimeter (EMC) responsible for diagnosing and replacing any electronics boards that were not operational. For another six month period, the author was the operations manager for the EMC. This involved being on-call expert for the EMC, being responsible for the running and maintenance of the sub-detector, chairing weekly operations meeting and regular presentations to the rest of the collaboration.

# 1

# Theory

## 1.1 The Standard Model

The Standard Model (SM) is the current theory of particle physics that describes the fundamental properties of the elementary particles and the interactions between them. Matter is made up of fermions, with spin-1/2, and the force-mediating particles are bosons, with spin-1. Within the SM there is still one fundamental particle that has yet to be observed, the Higgs boson. This spin-0 particle is integral in explaining the origins of the masses of the particles. Thus far, all experimental results are consistent with the SM, however, it is known that it is an incomplete theory for reasons discussed in Section 1.2. Therefore, New Physics (NP) beyond the SM must exist.

In this chapter the fundamental particles and their mediating particles will be introduced in Section 1.1.1. Electromagnetic symmetry breaking is discussed in Section 1.1.3. The incompleteness of the SM and NP models will be introduced in Section 1.2. The theoretical background for the decay $B \to K^*l^+l^-$ will be discussed in Section 1.3. Lastly, Section 1.3.3 will discuss NP scenarios and how angular measurements of $B \to K^*l^+l^-$ can be used to probe these models.

| Generation | Flavour | Charge ($e$) | Mass (GeV/$c^2$) | Interactions |
|---|---|---|---|---|
| 1 | $u$ | +2/3 | 0.0015 to 0.003 | strong, weak, EM |
| | $d$ | -1/3 | 0.0035 to 0.007 | strong, weak, EM |
| 2 | $c$ | +2/3 | 1.27 ± 0.09 | strong, weak, EM |
| | $s$ | -1/3 | 0.105 ± 0.025 | strong, weak, EM |
| 3 | $t$ | +2/3 | 171.3 ± 1.1 | strong, weak, EM |
| | $b$ | -1/3 | 4.20 ± 0.07 | strong, weak, EM |

Table 1.1: Fundamental properties of the quarks. The unit of charge ($e$) is the charge of the electron. [1]

| Generation | Flavour | Charge ($e$) | Mass (GeV/$c^2$) | Interactions |
|---|---|---|---|---|
| 1 | $e^-$ | -1 | 0.000511 | weak, EM |
| | $\nu_e$ | 0 | $< 3 \times 10^{-9}$ | weak |
| 2 | $\mu^-$ | -1 | 0.106 | weak, EM |
| | $\nu_\mu$ | 0 | $< 1.9 \times 10^{-4}$ | weak |
| 3 | $\tau^-$ | -1 | $1.7770^{+0.00029}_{-0.00026}$ | weak, EM |
| | $\nu_\tau$ | 0 | $< 0.018$ | weak |

Table 1.2: Fundamental properties of the leptons. [1]

### 1.1.1 The Fundamental Particles

There are six strongly interacting particles in the SM that are listed in Table 1.1. They are divided into three generations, with each generation containing an up-type quark, with charge, $+2/3e$, and a down-type quark, with charge $-1/3e$, where $e$ is the charge of the electron. The mass of the quarks increases with the generation. For each of the quarks there is an associated anti-quark with opposite quantum numbers such as charge and helicity, but identical in mass. The quarks have three additional associated quantum numbers, colour. Quarks never exist freely but do exist in colour neutral bound states composed of 2 or 3 quarks; mesons consist of a quark ($q$), antiquark ($\overline{q}$) pair and baryons are made up of $qqq$ or $\overline{qqq}$.

There are also six different types of leptons in the SM, whose properties are

| Gauge boson | Charge ($e$) | Mass (GeV/$c^2$) | Mediates |
|---|---|---|---|
| $\gamma$ | 0 | $< 6 \times 10^{-17}$ | EM |
| $g$ | 0 | 0 | strong |
| $Z^0$ | 0 | $91.1876 \pm 0.0021$ | weak |
| $W^{\pm}$ | $\pm 1$ | $80.398 \pm 0.025$ | weak |

Table 1.3: Fundamental properties gauge bosons. [1]

listed in Table 1.2. The three generations each contain a lepton with charge $-1e$, and a neutrino with charge $0e$. Like the quarks, the higher generations of leptons are heavier. They also have corresponding anti-particles. Unlike the quarks they do not carry colour charge and therefore have no strong interaction and can exist as free particles. The neutrinos also have no electric charge and only interact via the weak interaction.

There are three fundamental forces in the SM, each associated with one or more "force carrying", spin-1 gauge bosons. The properties of the gauge bosons are listed in Table 1.3. The electromagnetic (EM) force between electrically charged particles is mediated by massless photons. The $W^{\pm}$ and $Z^0$ mediates the charged and neutral weak force, respectively. The strong force between quarks is mediated by massless gluons. There are eight varieties of gluons that have colour/anti-colour charges so gluons self-interact. Unlike the other two fundamental forces the strong force grows stronger with distance leading to colour confinement.

### 1.1.2 The Standard Model Lagrangian

The SM is a gauge theory for the strong and electroweak interactions denoted: $SU(3)_C \times SU(2)_L \times U(1)_Y$. The electroweak part of the Lagrangian for the SM can be written as:

$$\mathcal{L} = \mathcal{L}(f, W, B) + \mathcal{L}(f/\Phi) + \mathcal{L}(W, B, \Phi) - V(\Phi) \tag{1.1.1}$$

where $f, W, B$ and $\Phi$ represent the fermions, $W$ gauge boson, $B$ gauge boson and the Higgs field, respectively [2, 3]. The second term described the Higgs boson acting on the fermions, the third term describes the Higgs acting on the gauge bosons and the last term describes the Higgs field. The SM Lagrangian can be written in a way that is $SU(2)_L \times U(1)$ gauge invariant. In the SM it is assumed neutrinos are massless and that there are no right-handed neutrinos to ensure there is no lepton mixing. The left-handed fermion doublets and the right-handed singlets can be expressed in the form:

$$Leptons: \begin{pmatrix} \nu_e \\ e \end{pmatrix}_L, \begin{pmatrix} \nu_\mu \\ \mu \end{pmatrix}_L, \begin{pmatrix} \nu_\tau \\ \tau \end{pmatrix}_L ; e_R, \mu_R, \tau_R \tag{1.1.2}$$

$$Quarks: \begin{pmatrix} u \\ d \end{pmatrix}_L, \begin{pmatrix} c \\ s \end{pmatrix}_L, \begin{pmatrix} t \\ b \end{pmatrix}_L ; u_R, d_R, c_R, s_R, t_R, b_R \tag{1.1.3}$$

$$Gauge\ bosons: \begin{pmatrix} W_\mu^1 \\ W_\mu^2 \\ W_\mu^3 \end{pmatrix} ; B_\mu \tag{1.1.4}$$

$$Scalars: \Phi = \begin{pmatrix} \Phi^+ \\ \Phi^0 \end{pmatrix}, \Phi^T = \begin{pmatrix} \Phi^- \\ \overline{\Phi}^0 \end{pmatrix}. \tag{1.1.5}$$

### 1.1.3 The Electroweak Theory and Symmetry Breaking

The electroweak interaction is a gauge theory that can be denoted: $SU(2)_L \times U(1)_Y$. The fields in this model are massless, but this is not what is observed experimentally for the $W, Z$ bosons. Adding a mass term of the form $M_W W_\mu W^\mu$, directly would destroy gauge invariance. Instead, a spontaneous symmetry breaking, $SU(2)_L \times U(1)_Y \rightarrow U(1)_{EM}$, is introduced to generate the required mass terms. This process allows fermions, gauge bosons and scalar fields to acquire mass via the Higgs mechanism [4, 5] while still preserving the symmetry under U(1) of electromagnetism. A potential of the form:

$$V(\phi) = \mu^2\phi^T\phi + \lambda(\phi^T\phi)^2; \text{ with } \mu^2 < 0; \; \lambda > 0 \tag{1.1.6}$$

can account for the acquired mass without violating the local gauge invariance of the group. For $\mu^2 < 0$, $V(\phi)$ has a minimum at $|\phi| = v/\sqrt{2} = \sqrt{-\mu^2/2\lambda}$ where $v$ is the non-zero vacuum expectation value after symmetry breaking. By making the transformation $\phi \rightarrow \phi + v$ the mass of the W and Z boson can be found to be $M_W = \frac{1}{2}vg_2$ and $M_Z = \frac{1}{2}v\sqrt{g_2^2 + g_1^2}$, where $g_1$ and $g_2$ are the weak isospin and hypercharge coupling constants. When the expressions for the masses are evaluated they are in good agreement with the experimentally observed values, $M_W = (80.398 \pm 0.025)$ GeV/$c^2$ and $M_Z = (91.1876 \pm 0.0021)$ GeV/$c^2$. The photon field remains unbroken, thus still remaining massless.

After the symmetry is broken there is one physical degree of freedom that remains, it corresponds to a neutral Higgs boson of mass $M_H = \sqrt{-2\mu^2}$. The mass of the Higgs boson is not explicitly predicted by the SM, therefore it must be found experimentally. There have been many attempts to find the Higgs boson at the LEP experiments at CERN [6] and the Tevatron experiments at Fermilab [7]. Thus far, all attempts have been unsuccessful, however, the mass of the SM Higgs is now bounded between $114$ GeV/$c^2 < m_H < 160$ GeV/$c^2$ at a 95% confidence level. The LHC at CERN will find out whether or not the SM Higgs does exist.

### 1.1.4 The CKM matrix and CP Violation

The Cabibbo Kobayashi Maskawa (CKM) matrix [8, 9, 10] is a unitary 3 x 3 matrix that characterises quark flavour mixing by $W^{\pm}$ coupling in the Standard Model. The CKM matrix connects the weak eigenstates $(d', s', b')$ and the corresponding mass eigenstates $(d, s, b)$:

$$\begin{pmatrix} V_{ud}V_{us}V_{ub} \\ V_{cd}V_{cs}V_{cb} \\ V_{td}V_{ts}V_{tb} \end{pmatrix} \begin{pmatrix} |d\rangle \\ |s\rangle \\ |b\rangle \end{pmatrix} = \begin{pmatrix} |d'\rangle \\ |s'\rangle \\ |b'\rangle \end{pmatrix}. \tag{1.1.7}$$

Any unitary $3 \times 3$ matrix such as the CKM matrix can be parameterised by three angles and six complex phases. By performing the appropriate transformations five of the phases can be removed leaving only one irreducible phase and the three rotation angles. The irreducible phase allows for a combined CP asymmetry, where C is charge conjugation and P is parity reversal. In the SM, the only source of CP violating asymmetries in the quark sector is this weak phase [11, 12]. No flavour mixing or CP violation is expected in the lepton sector in the SM.

The CKM matrix can be written in terms of the the Wolfenstein parameterisation [15], shown below:

$$V_{CKM} = \begin{pmatrix} 1-\lambda^2/2 & \lambda & A\lambda^3(\rho - i\eta) \\ -\lambda & 1-\lambda^2/2 & A\lambda^2 \\ A\lambda^3(1-\rho-i\eta) & -A\lambda^2 & 1 \end{pmatrix} + \O(\lambda^4) \qquad (1.1.8)$$

where $\rho, \eta$ is a point in the complex plane and the Cabibbo angle $\sin\theta_C = \lambda = |V_{us}|$ is used as an expansion parameter.

There are twelve unitary conditions that constrain the CKM matrix. The first type of constraints are on any row or column of the matrix:

$$\sum_k |V_{ik}|^2 = 1. \qquad (1.1.9)$$

This implies that the sum of all the coupling of all the up-type quarks to all the down type quarks is the same for all generations, otherwise known as the weak universality. The second type of constraints can be written as:

$$\sum_k V_{ik}V^*_{jk} = 0. \qquad (1.1.10)$$

This can be represented by six unitary triangles in the complex plane that all have different angles and lengths of sides. Thus far all experimental measurements are consistent with a unitary CKM matrix [16, 17]. Any enhancement to the amount of CP violation could indicate a contribution from NP. Recent results for the elements of the CKM matrix are shown in Equation 1.1.11, and Figure 1.1 shows the current constraints on the unitary triangle from tree-level process and $B_d$ mixing.

$$V_{CKM} = \begin{pmatrix} 0.97419 \pm 0.00022 & 0.2257 \pm 0.0010 & 0.00359 \pm 0.00016 \\ 0.2256^{\pm}0.0010 & 0.97334 \pm 0.00023 & 0.0415^{+0.0010}_{-0.0011} \\ 0.00874^{+0.00026}_{-0.00037} & 0.0407 \pm 0.0010 & 0.999133^{+0.000044}_{-0.000043} \end{pmatrix} \tag{1.1.11}$$

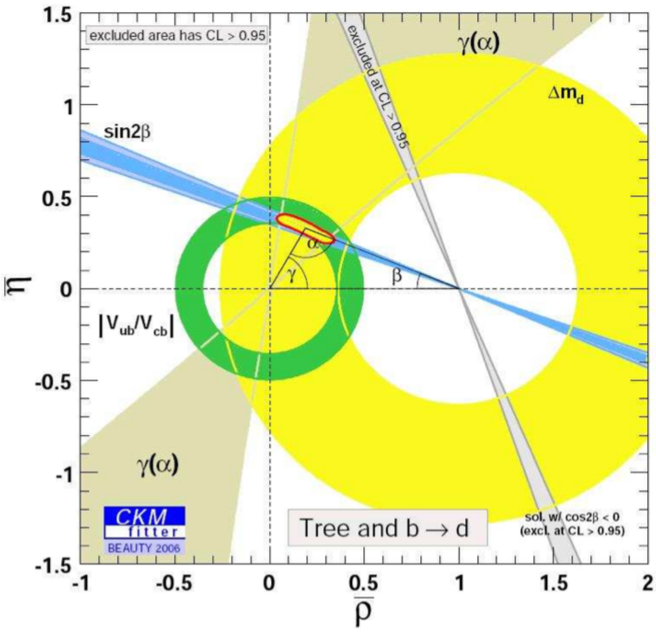

Figure 1.1: Current tree-level and $B_d$ mixing constraints on the unitary triangle. [17]

### 1.1.5 Flavour Changing Neutral Current Decay

Flavour changing neutral current (FCNC) [13] decays are processes that change one quark type to another with the same charge e.g. $b \to s$, $b \to d$, $s \to d$. They are forbidden to occur at tree level in the SM, however, they can proceed via

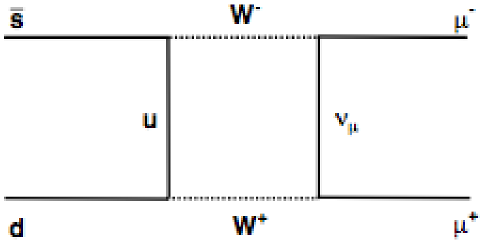

Figure 1.2: Example of an effective flavour changing neutral current kaon decay.

second order weak interactions with loop ("penguin") or box diagrams involving heavy virtual particles.

Using the decay $\overline{K}^0 \to \mu^+\mu^-$ as an example (Figure 1.2): from unitarity, the two-generation approximation is: $V_{us}V_{ud}^* + V_{cs}V_{cd}^* = \sin\theta_c \cos\theta_c - \cos\theta_c \sin\theta_c = 0$. Therefore, the contribution for the virtual *c* box diagram completely cancels with the virtual *u* box diagram. This cancellation is called the Glashow-Iliopoulos-Maiani (GIM) mechanism [18]. The third virtual quark, *t* has a very small CKM factor therefore only provides a small contribution to the amplitude. In the *b* system, where the *b* undergoes a flavour change, the CKM factors for the *t* quark is much larger: $V_{tb}V_{td}^* > V_{ts}V_{td}^*$. Therefore, the *t* quark provides the dominant contribution to the box diagram amplitude. The GIM mechanism breaks down at one-loop level and contributing penguin diagrams, although small, are not negligible. These second order weak processes have either electromagnetic or QCD vertices to conserve momentum, for example $b \to s\gamma$ or $b \to sg$, respectively.

## 1.2 Incompleteness of the SM and New Physics

There is impressive agreement between SM predictions and the experimental results. However, the SM is known not to be complete for the reasons discussed below, therefore, new physics beyond the SM must exist.

- Neutrinos are assumed to be massless. However, several experiments have observed neutrino mixing [19]. This indicates that the neutrinos do have masses, non-zero mixing angles and that the mass eigenstates are different from the weak eigenstates. Massive neutrinos would also imply that there are right handed neutrinos and Dirac left-handed anti-neutrinos or possibly Majorana neutrinos (where neutrinos and anti-neutrinos are the same particle) neither of which are in the SM. It is, however, possible that the right-handed neutrino is very heavy $\nu_R \sim 10^{11}$ GeV [20], due to the seesaw mechanism.

- Gravity is not included in the SM. Thus far, there is no way of combining this force with strong and electroweak interactions within the SM.
- In Section 1.1.3, it was stated that the Higgs mass is experimentally constrained to be ~160 GeV/$c^2$ or less [6, 7]. However, if the Higgs is not found in the mass range predicted in the SM, but is heavier, then the loop corrections to the mass are quadratically divergent and can be several orders of magnitude greater.
- The amount of CP violation that is predicted in the SM [14, 21] does not account for the matter anti-matter asymmetry that is present in the universe by an order of $\times 10^9$ [22]. In addition, baryon number violation is required which is not allowed in the SM and is not observed experimentally.
- Cosmologists have observed that the universe is made of more dark matter ($\sim 22\%$) than ordinary matter ($\sim 4\%$) [23]. By using many different methods such as studying the rotational speeds of galaxies and gravitational lensing of background objects by galaxy clusters, astronomers have detected dark matter at levels that can not be explained by the SM.
- Astronomers observe that universe is predominantly composed of dark energy [24] in order to explain that the universe appears to be expanding at an accelerated rate. The universe might actually be as much as 74% dark energy, this is not in the SM.

There are many different theories that describe physics beyond the SM; supersymmetry (SUSY) [25], string theory [26], extra-dimensions [27] and supergravity (SUGRA) [28] are a few of the more well studied theories. In SUSY for

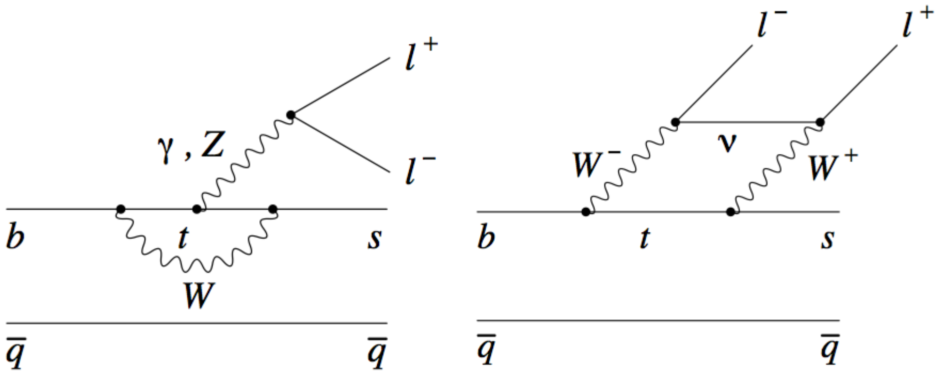

Figure 1.3: Photon penguin, $Z$ penguin and the $W$-box diagram.

every elementary particle there exists a corresponding supersymmetric particle that differs by half a unit of spin. Therefore, the SM quarks and leptons are paired with $spin = 0$ squarks and sleptons. The SM bosons are paired with $spin = 1/2$ neutralinos and charginos. The most studied SUSY theory is the Minimal Supersymmetric Standard Model (MSSM). In this model the Higgs sector is expanded to include two Higgs doublets with tan$\beta$ as the ratio of the vacuum expectation values.

There are many different SUSY models that are in agreement with the experimental results. SUSY ensures that the strong, electromagnetic and weak gauge couplings are unified at an energy scale of order ($\sim 10^{14}$ GeV).

## 1.3 The Decay $B \to K^{(*)}l^+l^-$

The decays $B \to Kl^+l^-$ and $B \to K^*l^+l^-$ where the $l^+l^-$ are charged lepton pairs, $e^+e^-$ or $\mu^+\mu^-$ result from $b \to s$ flavor-changing neutral currents (FCNC). As discussed in Section 1.1.5, they are forbidden to occur at tree level, however, they can occur in the SM via highly suppressed loop and box interactions, shown in Figure 1.3. All three diagrams involve the emission and reabsorption of W bosons with the heavy top quark dominating over the lighter $c$ and $u$ quarks.

### 1.3.1 The Effective Hamiltonian

The effective Hamiltonian for the process $b \rightarrow s l^+ l^-$ can be written as [29]:

$$H_{eff} = -4\frac{G_F}{\sqrt{2}} V_{ts}^* V_{tb} \sum C_i(\mu) O_i(\mu) \tag{1.3.1}$$

where $O_i(\mu)$ are the local renormalised operators with different topologies calculated at the energy scale $\mu$ and the $C_i(\mu)$ are the Wilson coefficients [30, 31]. $G_F$ is the Fermi coupling constant and $V_{ts}^* V_{tb}$ are the CKM matrix elements associated with the $b \rightarrow t \rightarrow s$ transition.

The Wilson coefficients are generally calculated at the $M_W$ scale and then evolved down to the mass of the $b$ [32]. The observables can be written in terms of the "effective" Wilson coefficients, $C_i^{eff}$. These coefficients absorb higher order contributions from the operator mixing and would be independent of the renormalisation scheme if they were calculated to all orders. However, they are usually presented in next to leading order (NLO) or next to next to leading order (NNLO) calculations. There are three Wilson coefficients that are relevant to the $b \rightarrow s l^+ l^-$ decay; $C_7^{eff}$ corresponding to the electromagnetic operator, and $C_9^{eff}$ and $C_{10}^{eff}$, which are the vector and axial vector terms of the electroweak penguin and box diagrams.

From an experimental viewpoint measurements of exclusive modes are easier to make than inclusive decays. However, the theoretical predictions [33, 34] are more complicated due to strong interaction effects from the $B \rightarrow K^*$ transition. These hadronic effects are described by form factors that have a large theoretical uncertainty. Another theoretical uncertainty discussed above is from the calculation of the Wilson coefficients. This uncertainty decreases as the order at which the calculation is made increases. There are also theoretical uncertainties from $c\bar{c}$ contributions in the high di-lepton mass-squared ($q^2$) region.

The branching fraction as a function of $q^2$ depends on the Wilson coefficients [34]:

| Coefficient | Value |
|---|---|
| $C_7^{eff}$ | -0.31 |
| $C_9^{eff}$ | 4.30 |
| $C_{10}^{eff}$ | -4.43 |

Table 1.4: Effective Wilson coefficients in the SM, evaluated at the scale $\mu = 4.6$ GeV. [34]

$$\begin{aligned}\frac{d\Gamma(b \to X_s l^+ l^-)}{d\hat{q}^2} \propto\, & (1-\hat{q}^2)^2((1+2\hat{q}^2)(|C_9^{eff}|^2 + |C_{10}^{eff}|^2) \\ & +4(1+\frac{2}{\hat{q}^2})|C_7^{eff}|^2 + 12Re(C_7^{eff} C_9^{eff*})).\end{aligned}$$

where $X_s$ refers to any hadronic system that contains one or three $s$ quarks and $\hat{q}^2 = m^2_{l^+l^-}/m^2_b$. At low $q^2$, the photon is nearly on mass-shell and the partial branching fraction will be sensitive to $C_7^{eff}$, whereas $C_9^{eff}$ and $C_{10}^{eff}$ will dominate at larger $q^2$, and at the intermediate $q^2$ there are interference effects. The SM values for the effective Wilson coefficients evaluated at $\mu = 4.6$ GeV are shown in Table 1.4.

Prior to the discovery of $B \to K^* l^+ l^-$, searches were conducted at a number of experiments, CLEO [35, 36, 37], CDF [38, 39], Belle [40] and *BABAR* [41, 42] until it was eventually discovered at Belle [43]. To date, all experimental results are consistent with the SM predictions [44]-[46]. The semi-inclusive analysis of the $B \to X_s l^+ l^-$ branching fraction, where $X_s$ is a final state with a kaon plus up to three pions was measured at both *BABAR* [47] and Belle [48]. The world average experimental measurement for the $B \to K^* l^+ l^-$ branching fraction is $(1.08^{+0.12}_{-0.11}) \times 10^{-6}$. Figure 1.4 shows the shows the current *BABAR*, Belle and CDF branching fraction results for each of the $B \to X_s l{+}l{-}$ modes.

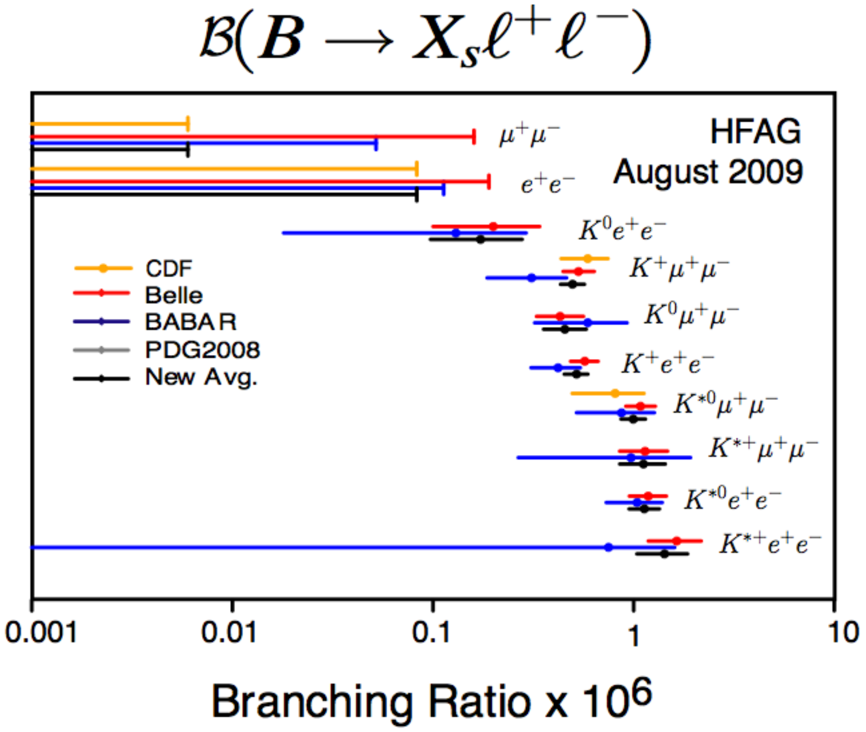

Figure 1.4: Current *BABAR*, Belle and CDF branching fraction results for each of the $B \to X_s l{+}l{-}$ modes. [49]

### 1.3.2 $K^*$ Polarisation, Forward-backward Asymmetry and Decay Angle

Angular distributions, such as the fraction of longitudinal $K^*$ polarisation ($F_L$), the forward-backward asymmetry ($A_{FB}$), and the decay plane angle ($\phi$) are measurements that allow both the magnitudes and phases of the Wilson coefficients to be constrained. For some variables, such as the branching fraction, some of the Wilson coefficients enter quadratically, and only their magnitudes can be deduced.

The angular measurements are made in the helicity frame, shown in Figure 1.5:

- $\theta_{K^*}$ is the kaon angle relative to the $B$ in the $K^*$ rest frame, from which the $K^*$ polarisation $F_L$ can be determined.

- $\theta_l$ is the lepton angle relative to the $B$ in the di-lepton rest frame, from which the forward-backward asymmetry $A_{FB}$ can be determined.
- $\phi$ is the angle between the $K^*$ and di-lepton decay planes.

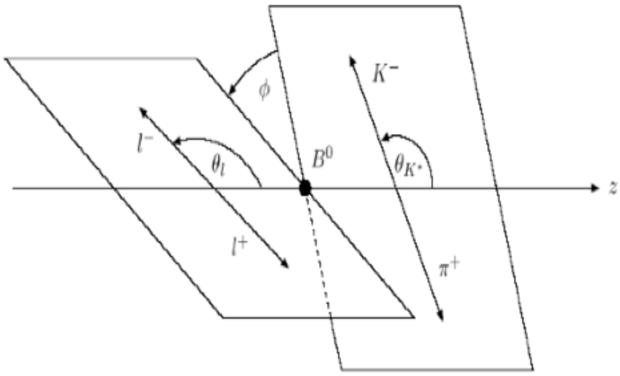

Figure 1.5: Definition of the helicity angles

The forward backward asymmetry as a function of $\hat{q}^2$ is defined as:

$$A_{FB}(\hat{q}^2) = \frac{\int_0^1 d\cos\theta_l \frac{d^2\Gamma(B\to K^{(*)}l^+l^-)}{d\cos\theta_l d\hat{q}^2} - \int_{-1}^0 d\cos\theta_l \frac{d^2\Gamma(B\to K^{(*)}l^+l^-)}{d\cos\theta_l d\hat{q}^2}}{d\Gamma(B\to K^{(*)}l^+l^-)/d\hat{q}^2}. \tag{1.3.2}$$

"Forward" decays correspond to $\cos\theta_l > 0$ and "backward" decays correspond to $\cos\theta_l < 0$, where $\theta_l$ is defined as the angle between the direction of the $B$ and negatively charged lepton for a $B^+$ or $B^0$ or between a $B$ and positively charged lepton for $B^-$ or $\overline{B}^0$ [50].

The distribution of $A_{FB}$ as a function of $\hat{q}^2$ depends on the Wilson coefficients as [51]:

$$\frac{dA_{FB}}{d\hat{q}^2} \propto C_{10}\left[Re(C_9^{eff}) + \frac{C_7^{eff}}{\hat{q}^2}\right]. \tag{1.3.3}$$

The differential decay distribution of $B^0 \to K^{*0}l^+l^-$ can be written in the general form below by summing over the spins of the final particles:

$$d^4\Gamma = \frac{9}{32\pi} I(q^2, \theta_l, \theta_{K^*}, \phi) dq^2 d\cos\theta_l d\cos\theta_{K^*} d\phi \tag{1.3.4}$$

where $I(q^2, \theta_l, \theta_{K^*}, \phi)$ is:

$$I_1 + I_2 \cos 2\theta_l + I_3 \sin^2\theta_l \cos 2\phi + I_4 \sin 2\theta_l \cos\phi + I_5 \sin\theta_l \cos\phi + I_6 \cos\theta_l$$
$$+ I_7 \sin\theta_l \sin\phi + I_8 \sin 2\theta_l \sin\phi + I_9 \sin^2\theta_l \sin 2\phi. \tag{1.3.5}$$

The functions $I_{1-9}$ can be written in terms of $A_0$, $A_\perp$ and $A_\|$ that represent the longitudinal amplitude, the transverse amplitude and the parallel amplitude. The six $I$ coefficients below are $L/R$ symmetric:

$$\begin{array}{ll} I_1 = \frac{3}{2}(|A_\perp^2| + |A_\|^2|)\sin^2\theta_K + |A_0|^2\cos^2\theta_K & I_4 = Re(A_0 A_\|^*)\sin 2\theta_K \\ I_2 = (|A_\perp^2| + |A_\||^2)\sin^2\theta_K - |A_0|^2\cos^2\theta_K & I_8 = Re(A_0 A_\perp^*)\sin 2\theta_K \\ I_3 = (|A_\perp^2| + |A_\|^2|)\sin^2\theta_K & I_9 = -2Re(A_\| A_\perp^*)\sin^2\theta_K. \end{array}$$

The remaining three $I$ coefficients can produce forward-backward asymmetries because they are $L/R$ antisymmetric:

$$I_5 = 2Re(A_0 A_\perp^*)\sin 2\theta_K \quad I_6 = 4Re(A_\| A_\perp^*)\sin^2\theta_K \quad I_7 = 2Im(A_0 A_\|^*)\sin 2\theta_K.$$

In this thesis, the $K^*$ polarisation and forward-backward asymmetry will be measured using two different approaches. The first method will be referred to as the "1D fits" because it uses two one-dimensional distributions for $\cos\theta_K$ and $\cos\theta_l$ to extract the values of $F_L$ and $A_{FB}$. By integrating Equation 1.3.4 over $\cos\theta_l$ and $\phi$ to get a one dimensional angular distribution for $\cos\theta_K$ [52]:

$$\frac{1}{\Gamma}\frac{d\Gamma}{d\cos\theta_K} = \frac{3}{2}F_L\cos^2\theta_K + \frac{3}{4}(1 - F_L)(1 - \cos^2\theta_K). \tag{1.3.6}$$

From this angular distribution $F_L$ can be measured. Then, by integrating 1.3.4 over $\cos\theta_K$ and $\phi$ a one dimensional angular distribution can be found for $\cos\theta_l$ [52]:

$$\frac{1}{\Gamma}\frac{d\Gamma}{d\cos\theta_l} = \frac{3}{4}F_L(1-\cos^2\theta_l) + \frac{3}{8}(1-F_L)(1+\cos^2\theta_l) + A_{FB}\cos\theta_l. \qquad (1.3.7)$$

Using the value of $F_L$ from Equation 1.3.6, $A_{FB}$ can then be found.

The second approach is referred to as the "2D fit" because it uses the two dimensional distribution of $(\cos\theta_K, \cos\theta_l)$ to extract the values of $F_L$ and $A_{FB}$. This second method uses the correlation that exists between the two angles and is a more accurate model. Since $B \to K^* l^+ l^-$ is a rare decay, and the second method will be challenging with low statistics, it was decided that $F_L$ and $A_{FB}$ will be measured using both techniques. By integrating over $\phi$ the two dimensional angular distribution for $\cos\theta_l$ and $\cos\theta_K$ is [52]:

$$\begin{aligned}\frac{1}{\Gamma}\frac{d^2\Gamma}{d\cos\theta_l d\cos\theta_K} &= \frac{9}{8}F_L\cos^2\theta_K\sin^2\theta_l + \frac{9}{32}F_T\sin^2\theta_K(1+\cos^2\theta_l)\\ &+\frac{3}{4}A_{FB}\sin^2\theta_K\cos\theta_l \qquad (1.3.8)\end{aligned}$$

where $F_T = 1 - F_L$.

The decay plane angle measurement will be referred to as the "$\phi$ fit". By integrating Equation 1.3.4, over $\cos\theta_{K^*}$ and $\cos\theta_l$ the angular distribution for $\phi$ can be found:

$$\frac{d\Gamma}{d\phi} \propto (|A_0|^2 + |A_\perp|^2 + |A_\||^2) - Re(A_\| A_\perp^*)\cos 2\phi - Im(A_\| A_\perp^*)\sin 2\phi \qquad (1.3.9)$$

where $|A_0|^2 + |A_\perp|^2 + |A_\||^2 = |A|^2$ is the total rate of the decay.

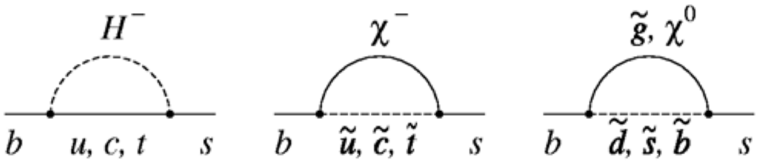

Figure 1.6: Possible new SUSY particles contributing to $b \rightarrow sl^+l^-$. These particles are: charged Higgs, chargino, gluino and neutralino, respectively.

### 1.3.3 $B \rightarrow K^*l^+l^-$ as a Probe for New Physics

Flavour changing neutral current decays provide an excellent probe in the search for physics beyond the SM. In many of the NP models, including supersymmetry, there could be changes in the decay amplitudes leading to different rates and kinematic distributions in FCNC decays. NP models would allow other bosons or particles to contribute to the loop, such as a charged Higgs boson, topcolor, weak-scale supersymmetry, fourth-generation fermions or leptoquarks. The Feynman diagrams for SUSY are shown in Figure 1.6.

There has been no experimental observation of superparticles or any other new physics contribution. The experimental results have ruled out superpartners with a mass below a hundred $\mathrm{GeV}/c^2$ [53, 54], however, many phenomenological models predict that superpartners should be found at the TeV energy scale. If this is true then the LHC experiments could find and identify the superpartners.

The forward-backward asymmetry is an excellent probe for new physics [51] - [60]. The relative signs, magnitudes and phases of the Wilson coefficients dramatically change the distribution of $A_{FB}$. For the case of change in relative signs, the four scenarios shown in Figure 1.7 are:

- $C_7^{eff} < 0, C_9^{eff} C_{10}^{eff} < 0$: $A_{FB} < 0$ for $q^2 < 4.2$ GeV$^2/c^4$ and $A_{FB} > 0$ for $q^2 > 5$ GeV$^2/c^4$. This case includes the SM (Table 1.5 contains the SM predictions).
- $C_7^{eff} < 0, C_9^{eff} C_{10}^{eff} > 0$: $A_{FB} < 0$ for all $q^2$.
- $C_7^{eff} > 0, C_9^{eff} C_{10}^{eff} < 0$: $A_{FB} > 0$ for all $q^2$.

| Mode | $A_{FB}$ (low) | $A_{FB}$ (high) | $F_L$ (low) | $F_L$ (high) |
|---|---|---|---|---|
| $B \to K^+ l^+ l^-$ | 0 | 0 | N/A | N/A |
| $B \to K^* l^+ l^-$ | 0.03 | 0.36 | 0.67 | 0.48 |

Table 1.5: Predictions for $A_{FB}$ and $F_L$ from SM calculations corresponding the "low" $q^2$ region ($0.1 < q^2 < 6.5$ GeV$^2/c^4$) and "high" $q^2$ region ($q^2 > 10.24$ GeV$^2/c^4$) in Figure 1.7.

- $C_7^{eff} > 0, C_9^{eff} C_{10}^{eff} > 0$: $A_{FB} > 0$ for $q^2 < 4.2$ GeV$^2/c^4$ and $A_{FB} < 0$ for $q^2 < 5$ GeV$^2/c^4$.

From Equation 1.3.3 is can be seen that for the low $q^2$ region, $q^2 < 4.2$ GeV$^2/c^4$, $C_7^{eff}$ is the dominant term where as in the high $q^2$ region, $q^2 > 4.2$ GeV$^2/c^4$, $C_9^{eff} C_{10}^{eff}$ are dominant. Therefore, when $C_7^{eff}$ has the opposite sign relative to the SM the distribution of $A_{FB}$ is positive at low $q^2$. A similar effect occurs at high $q^2$ when the sign of $C_9^{eff} C_{10}^{eff}$ has the opposite sign relative to the SM. The magnitude, phase and sign of the Wilson coefficients are all model dependent. Many of the SUSY models have an admixture of Wilson coefficients from the left-handed SM, $C_{iL}$, and possible right-handed NP contributions, $C_{iR}$.

The zero-point crossing is theoretically the most precisely predicted point of the distribution of $A_{FB}$. At this point the form factors have essentially no hadronic uncertainty therefore the precision on the zero point is essentially determined by the accuracy of the effective coefficients and $m_b$. In the SM the zero point crossing is at 4.2 ± 0.6 GeV$^2/c^4$ [61]. In many NP models it is predicted that there will be no zero point crossing therefore experimentally determining the value for $A_{FB}$ accurately in the low $q^2$ region will provide the highest sensitivity to NP.

Since the distribution of $F_L$ is always positive, it is only the magnitude that changes between different physics models. Figure 1.7 shows that $F_L$ is large at low $q^2$ in the SM. The value for $F_L$ is smaller for models with the wrong sign $C_7^{eff}$. At high $q^2$ different scenarios are almost indistinguishable.

At low $q^2$ the angular distribution of the decay plane angle can be written as:

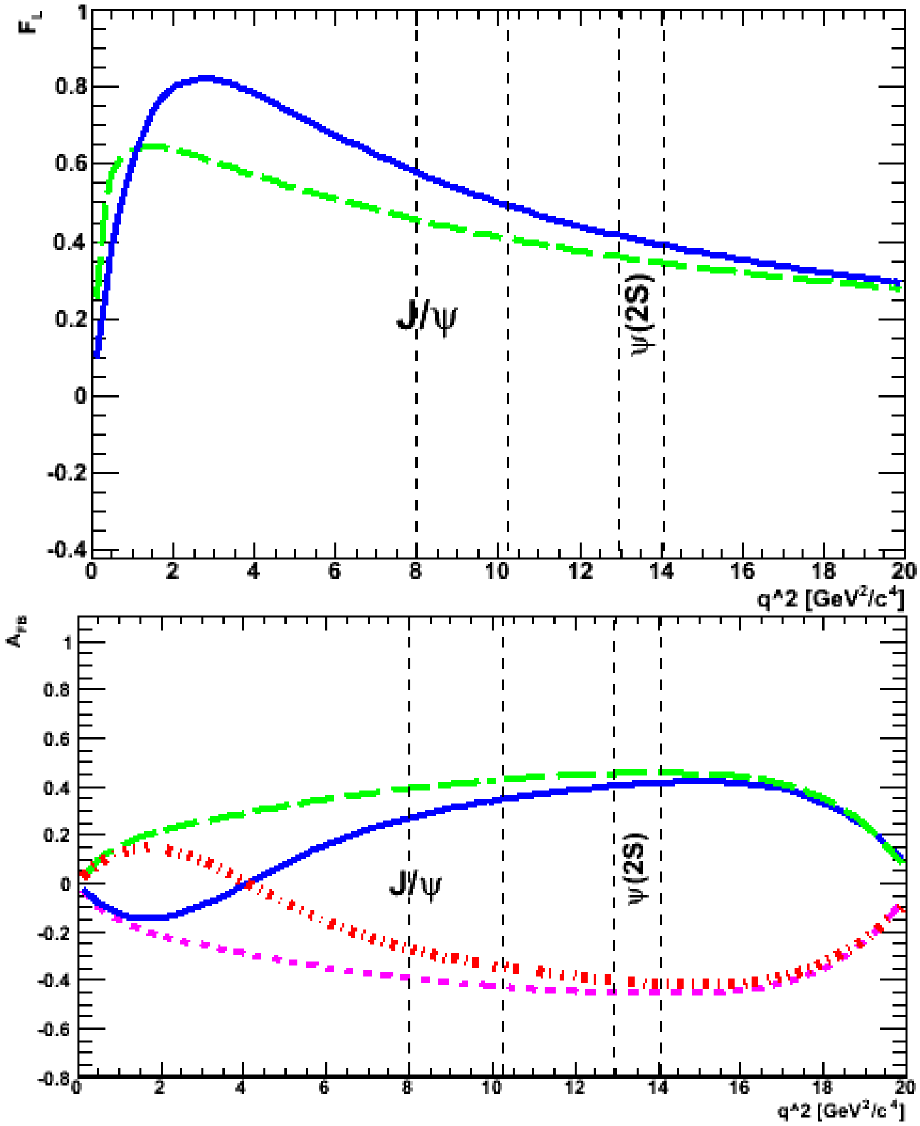

Figure 1.7: Top: The distribution of $F_L$ over $q^2$ for different Wilson coefficients: SM (blue) and $C_7 = -C_7(SM)$ (green). Bottom: The distribution of $A_{FB}$ over $q^2$ for different Wilson coefficients: SM (blue), $C_7 = -C_7(SM)$ (green), $C_9C_{10} = -C_9C_{10}(SM)$ (magenta) and $C_7 = -C_7(SM), C_9C_{10} = -C_9C_{10}(SM)$ (red).

$$\frac{d\Gamma}{d\phi} \propto 1 + \frac{Re(C_{7R}C_{7L})}{|C_{7L}|^2 + |C_{7R}|^2} \cos 2\phi = A + B \cos 2\phi. \tag{1.3.10}$$

In the SM $C_{7R}$ is predicted to be small therefore leading to a flat distribution at low $q^2$. At high $q^2$ the $\cos 2\phi$ term becomes significant due to the $C_9$ and $C_{10}$ contributions.

Previous angular measurements of $K^*l^+l^-$ and the study of other decays, such as $b \to s\gamma$ [62], have constrained the values of the Wilson coefficients. The experimental results provide upper limits that are used to bound possible new physics models.

## 1.4 Conclusion

This chapter gave an overview of the current knowledge of the SM and the reasons why NP beyond the SM must exist. The angular analysis of $B \to K^*l^+l^-$ is an excellent probe that can be used to search for NP contributions. A precise measurement of the distribution of $F_L$ and $A_{FB}$ as a function $q^2$ would require a large amount of data. In Chapter 6, a result for the $F_L$ and $A_{FB}$ in two regions of $q^2$: a "low" region above the photon pole but below the $J/\Psi$ resonance 0.1 $< q^2 <$ 6.5 GeV$^2/c^4$ and a "high" region above the $J/\Psi$ resonance excluding the $\Psi(2S)$ resonance $q^2 >$ 10.24 GeV$^2/c^4$. These measurement will be made using a dataset of 384 million $B\overline{B}$s is referred to as the "Run 5" analysis. In Chapter 7, the "Run 6" analysis will make measurements the four $q^2$ bins from Table 1.6, using the full BABAR dataset of 468 million $B\overline{B}$. These measurements allow the general shape of the $F_L$ and $A_{FB}$ as a function of $q^2$ to be determined. Table 1.6 also lists the excluded regions for the $J/\Psi$ and $\Psi(2S)$ resonances.

| Region | $q^2$ min (GeV$^2/c^4$) | $q^2$ max (GeV$^2/c^4$) |
|---|---|---|
| POLE | 0.00 | 0.10 |
| **q0** | **0.10** | **4.00** |
| **q1** | **4.00** | **8.0** |
| $J/\psi$ | 8.00 | 10.24 |
| **q2** | **10.24** | **12.96** |
| $\psi(2S)$ | 12.96 | 14.06 |
| **q3** | **14.06** | $(m_B - m_{K^{(*)}})^2$ |

Table 1.6: $F_L$ and $A_{FB}$ will be measured in the four $q^2$ regions (in bold) for the Run 6 analysis. The vetoed charmonium and POLE regions are listed for reference.

# 2

# The BaBar Detector

This chapter will describe the PEP-II collider and the BABAR detector [63]. Section 2.1 will detail the design requirements for the PEP-II collider and the performance over the lifetime of the experiment. Section 2.2 will give an overview of the BABAR detector and describe the six constituent sub-detectors. The remainder of the chapter will discuss the physics and design requirements of each of the sub-detectors, with a summary of the achieved performance.

## 2.1 The PEP-II Collider

PEP-II is an $e^+e^-$ collider that operates at or near the center of mass (CM) energy of 10.58 GeV and a peak luminosity of $\sim 10^{34}$ cm$^{-2}s^{-1}$. This corresponds to the $\Upsilon(4S)$ resonance that decays to approximately equal numbers of $B^0\overline{B}^0$ and $B^+B^-$ pairs. The energies of the $e^-$ and $e^+$ beams are asymmetric, 9 GeV and 3.1 GeV, respectively, therefore the CM is moving in the laboratory frame of reference, with a boost of $\beta\gamma = 0.56$. The CM energy is just above the threshold energy to produce $B\overline{B}$, therefore they do not travel far in the CM frame before decaying. An asymmetric collider is required in order to boost the B mesons in the laboratory frame. Many other processes occur at a high rate including Bhabha events where $e^+e^- \rightarrow e^+e^-$ or $e^+e^- \rightarrow e^+e^-\gamma$, and continuum background processes, $e^+e^- \rightarrow \mu^+\mu^-$, $e^+e^- \rightarrow \tau^+\tau^-$ and $e^+e^- \rightarrow q\overline{q}$, where $q = udsc$ quarks. Bhabha and $e^+e^- \rightarrow \mu^+\mu^-\gamma$ can be easily identified

| $e^+e^- \rightarrow$ | Cross-section (nb) |
|---|---|
| $b\bar{b}$ | 1.10 |
| $c\bar{c}$ | 1.30 |
| $s\bar{s}$ | 0.35 |
| $u\bar{u}$ | 1.39 |
| $d\bar{d}$ | 0.35 |
| $\tau^+\tau^-$ | 0.94 |
| $\mu^+\mu^-$ | 1.16 |
| $e^+e^-$ | 40 |

Table 2.1: Production cross-sections at $\sqrt{s} = 10.58$ GeV.

and are used to calibrate parts of the detector. The production cross sections for the continuum backgrounds are shown in Table 2.1. These events can be distinguished from the $B\overline{B}$ events because of their smaller masses and, therefore, more jet-like distribution. About 10% of the time the accelerator runs at a center of mass energy ∼40 MeV below the $\Upsilon(4S)$. At this energy no $B\overline{B}$ are produced and the continuum backgrounds can be studied.

The electrons are produced in bunches by a polarised electron gun and accelerated in the 3 km Stanford linear accelerator. The accelerator uses klystrons that produce microwaves to create an oscillating electric and magnetic field. Some of the electrons are separated and collided with a tungsten target to produce $e^+e^-$ pairs. The positrons can then be collected and accelerated out of phase with the electrons until they have both reached their target energies. They are then injected into the two PEP-II storage rings, the High Energy Ring (HER) and Low Energy Ring (LER) where they travel in opposite directions and collide at the interaction point, IR-2, shown in Figure 2.1 . Although most of the electrons and positrons do not collide, the luminosity of the beam does decrease over time. At the beginning of the experiment data-taking was stopped every 45 minutes to allow the rings to be refilled. In 2004, trickle injection started allowing bunches to be continuously injected. This ensured that the luminosity stayed constant and that data-taking was uninterrupted.

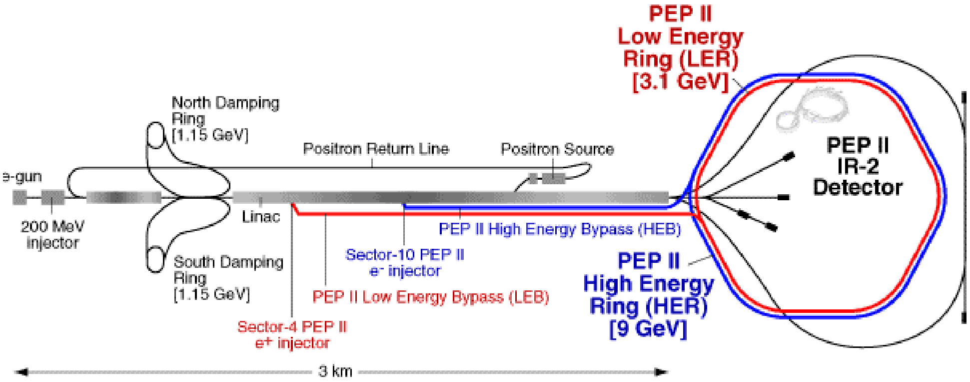

Figure 2.1: Layout of the PEP-II storage rings and linear accelerator.

The beams are split into about 1500 bunches to reduce the amount of beam-beam interference. The beams are separated in the horizontal plane using a dipole magnet B1 just before the interaction region, shown in Figure 2.2 and eventually the LER and HER are separated vertically in the rest of the ring. The *BABAR* solenoid is also used to separate the beams because it is slightly off axis to the beampipe. Quadrupole magnets QD1 and QD2 are used to focus the LER beam in both the vertical and horizontal planes. The QD4 and QD5 quadrupole magnets are used to focus the HER beam.

When the beams pass through the B1 and QD1 magnets the deflection causes synchrotron radiation at the IR. The geometry of the IR was designed such that most of the synchrotron radiation passes through the detector without interaction. A diagram of the horizontal view of the *BABAR* IR is shown in Figure 2.2. Other background events can be produced by beam particles interacting with gas molecules and losing momentum. The particles can then collide with the beam pipe and cause an electromagnetic shower. This can be reduced by maintaining a good vacuum in the beam pipe. The last main source of background comes from Bhabha scattering ($e^+e^- \rightarrow e^+e^-\gamma$) a short distance before the IR causing an electromagnetic shower, this effect scales with luminosity.

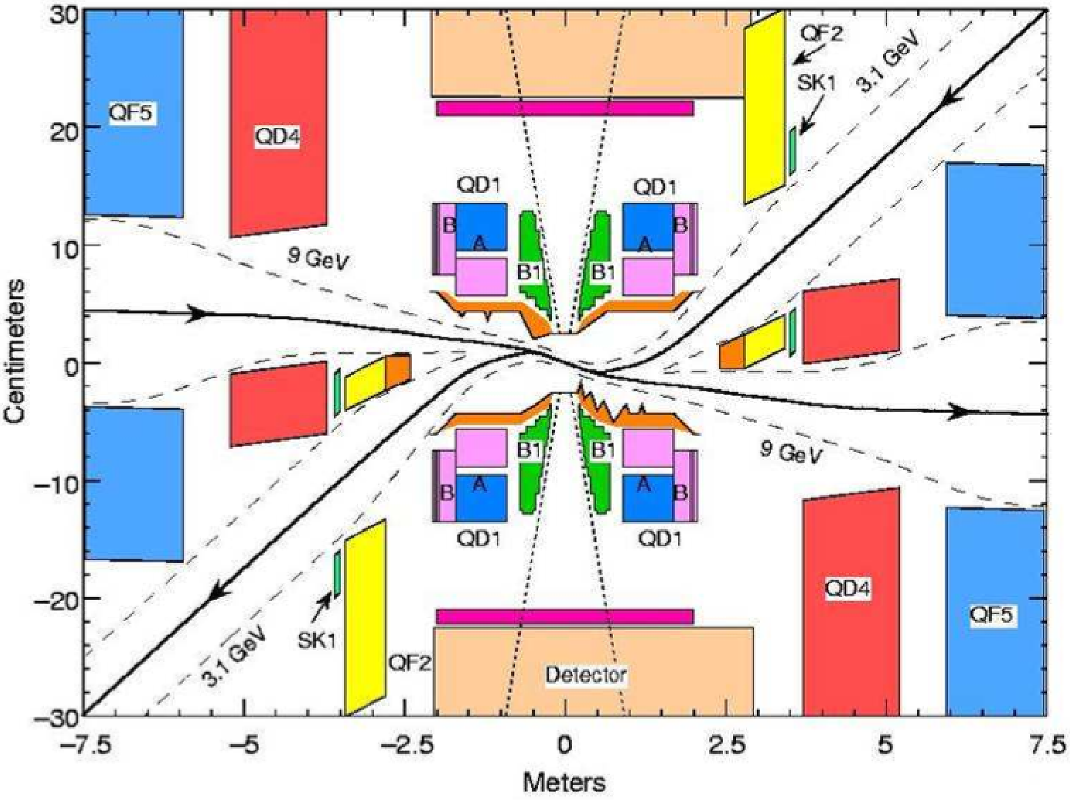

Figure 2.2: Horizontal view of the *BABAR* interaction region (IR).

### 2.1.1 Performance

The PEP-II accelerator has surpassed both its original design luminosity of $3 \times 10^{33}$ cm$^{-2}$s$^{-1}$ and integrated luminosity of $30\ fb^{-1}$. The achieved integrated luminosities are shown in Figures 2.3 and 2.4.

## 2.2 The *BABAR* Detector

The *BABAR* detector is made up of six constituent parts forming layers out from the interaction point. There are five sub-detectors: the Silicon Vertex Tracker (SVT), the Drift Chamber (DCH), the Detector of Internally Reflected Cherenkov Radiation (DIRC), the Electromagnetic Calorimeter (EMC) and the Instrumented Flux Return (IFR), and a superconducting magnet. The layout of the *BABAR* detector is shown in Figure 2.5.

The vertex detector is the only part of *BABAR* that is mounted inside the 20 cm support tube that is attached to the PEP beampipe and magnets. The detector is asymmetric about the interaction point to account for the asymmetric $e^+e^-$ interactions.

To achieve the maximum physics potential [10] the *BABAR* detector provides:

- The maximum coverage of acceptance angles in the centre-of mass frame.
- High resolution of the SVT, essential for the measurement of the $B$ decay vertex and the extraction of CP asymmetries. Background rejection is also improved by a higher resolution, which increases the efficiency and purity of the data.
- Good position and momentum resolution for charged particles over the transverse momentum range $0.06 < p_t < 4$ GeV$/c$.
- Good energy and angular resolution for photons over the energy range, $0.02 < E_\gamma < 4$ GeV. This is essential for detecting $\pi^0$ and $\eta$ particles.
- Particle identification over a wide kinematic range (0.2-4 GeV) for $e, \mu, \pi, K$ and $p$. This is necessary for flavour tagging and allows final states such

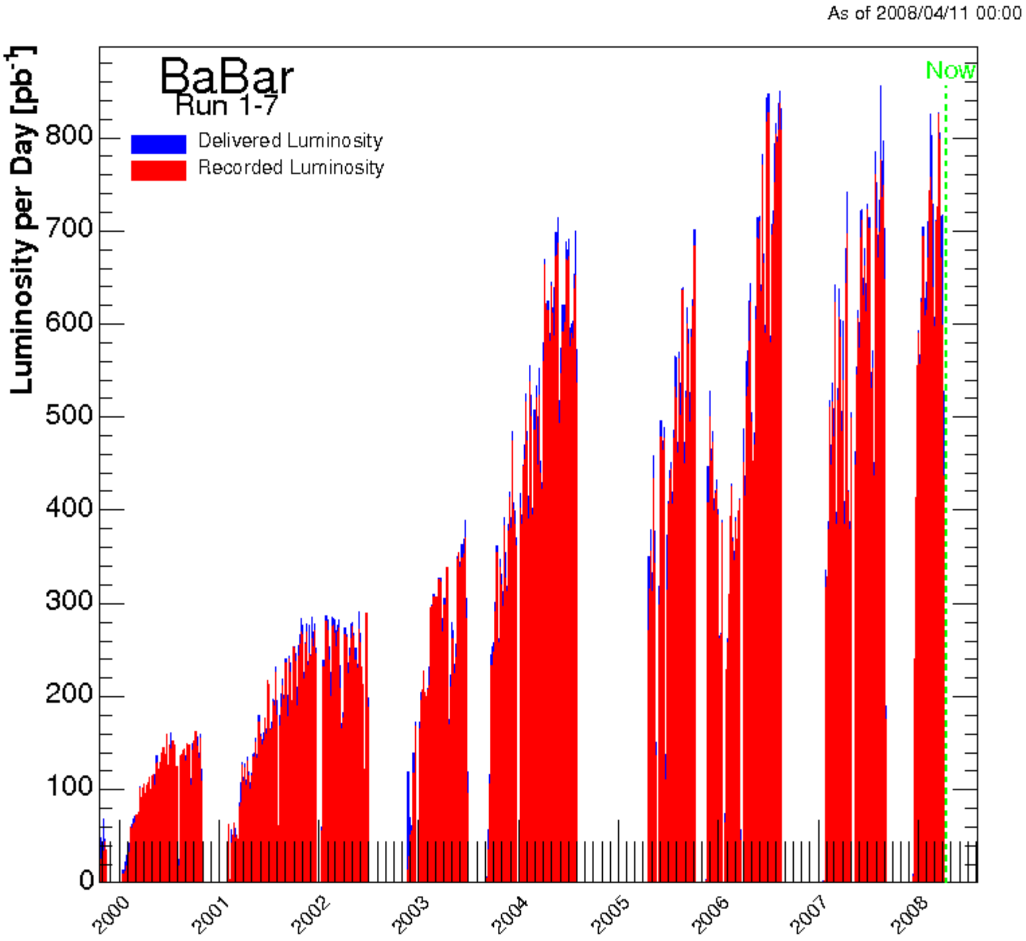

Figure 2.3: Daily luminosity (delivered and recorded) over the lifetime of the *BABAR* experiment.

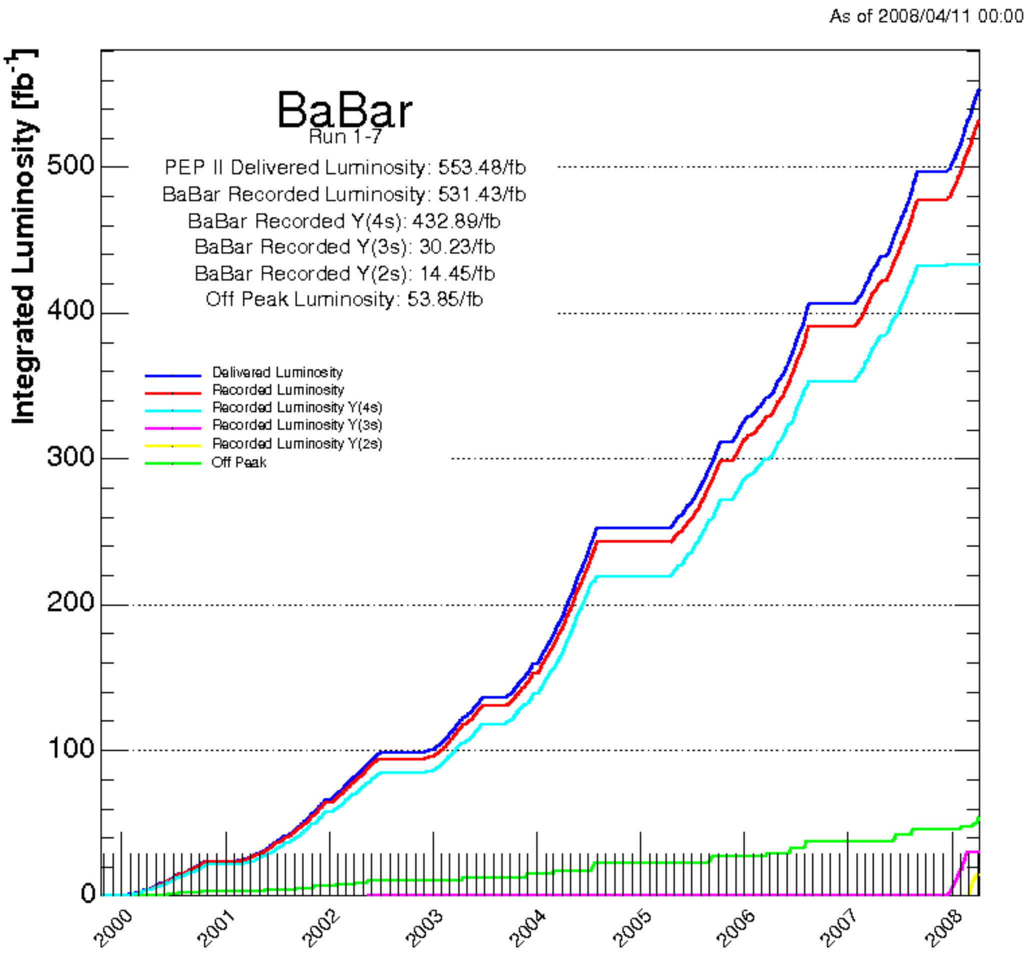

Figure 2.4: Integrated luminosity (delivered and recorded) over the lifetime of the *BABAR* experiment.

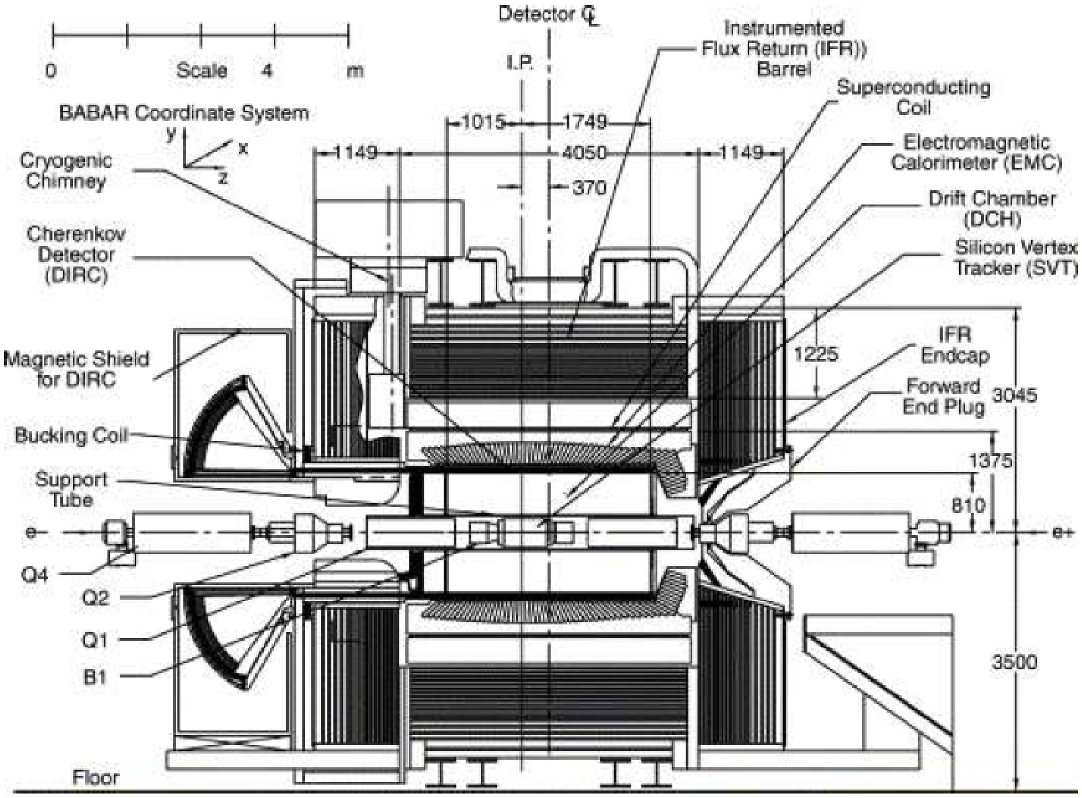

Figure 2.5: The layout of the *BABAR* detector.

as $K^+\pi^-$ and $\pi^+\pi^-$ to be separated.

In the standard coordinate system that is used when describing the BABAR detector the $z$-axis is along the solenoid's magnetic field direction, with $+z$ in the direction of travel of the electrons. The $y$-axis points vertically up and the $x$-axis horizontally away from the centre of the PEP-II rings. Polar coordinates $(\theta, \phi)$ are also used, with $\theta = 0$ being the $+z$-axis and $\phi = 0$ the $x$-axis.

## 2.3 Silicon Vertex Tracker (SVT)

### 2.3.1 SVT Physics Requirements

The primary job for the vertex tracker is to make precise measurements of the impact parameter and track directions for B meson decay vertices. The SVT provides information about the initial charged track and the track angle. For particles with transverse momentum $p_t < 100$ MeV/$c$ that do not reach the DCH, the SVT provides the only source of tracking data. For particles with $p_t < 700$ MeV/$c$ the ionisation losses ($dE/dx$) in the SVT aid in the particle identification process.

### 2.3.2 SVT Design

The SVT was designed to withstand an integrated radiation of 2 Mrad over its lifetime. The amount of material is kept to a minimum to reduce the effect of multiple scattering and bremsstrahlung to ensure that the performance of the DCH will not be degraded. Its design is restricted by the layout of the IR but it still has an acceptance angle in polar coordinates of 20.1° to 150.2°, encompassing 90% of the solid angle in the center of mass frame. Diagrams of the transverse and longitudinal cross section are shown in Figure 2.6 and 2.7.

The SVT is made up of five concentric layers of double-sided silicon microstrip sensors in both the $z$ and $\phi$ directions. Each silicon sensor is a 300 $\mu$m thick high resistivity n-type silicon wafer. Measurements of the decay vertices are most accurate near the IR, as the particles have not undergone multiple

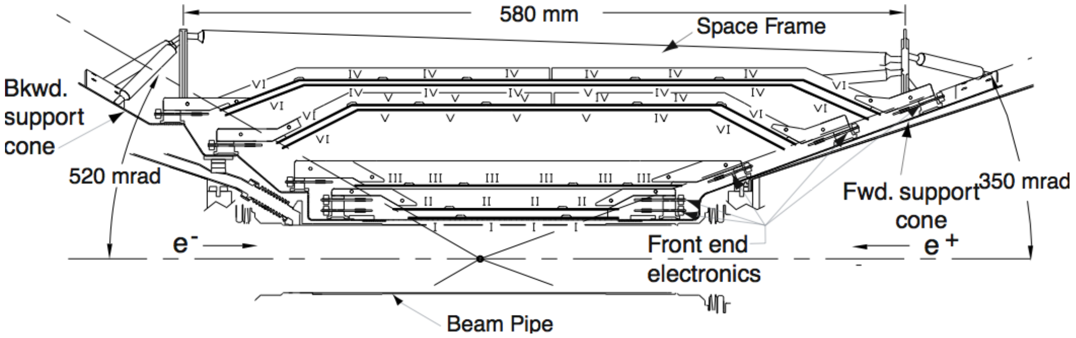

Figure 2.6: Transverse (r/z) cross section of the SVT.

scattering. Therefore, the first three layers responsible for measuring initial track parameters are located as close to the beampipe as possible. The outer two layers are closer to the DCH allowing tracks to be more easily matched between the sub-detectors. Each of the 5 layers are made up of overlapping modules. The inner layers are tilted by 5° in $\phi$. The outer layers ensure complete coverage whilst keeping the amount of material to a minimum.

When a high energy particle passes through an SVT module, the orbital electrons of the Si are excited. This produces positive holes and conducting electrons that travel when a voltage is applied. The electronic signal goes to the readout chip where it is amplified and sent to the front end electronics. A time over threshold technique is used to find the total charge that was deposited in the sensor. This technique supplies both position and $dE/dx$ measurements.

Both the local alignment, the position of each sensor, and the global alignment of the SVT relative to the rest of the detector, must be well known. These are essential when trying to measure track information about a particle. The global alignment is measured by fitting tracks that have a large number of SVT and DCH hits. These fits are performed for each of the systems individually and then alignment parameters can be obtained.

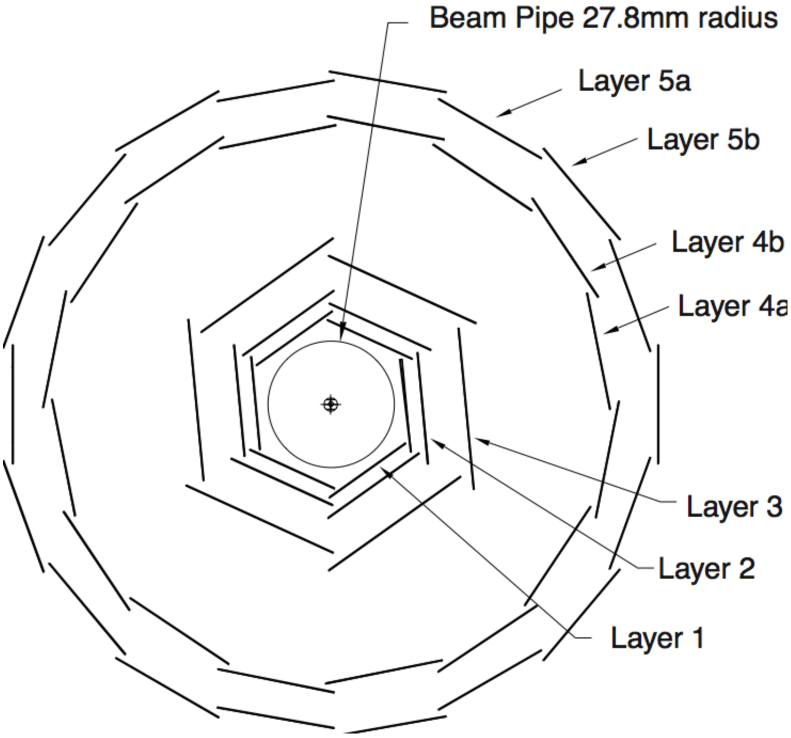

Figure 2.7: Longitudinal ($r/\phi$) cross section of the SVT.

### 2.3.3 SVT Performance

The longitudinal ($z$) and azimuthal ($\phi$) spatial resolution for a layer in the SVT is calculated by studying Bhabha and di-muon events, using only the data from the surrounding layers [64]. The inner layers have a hit resolution between 12-35 $\mu$m in both $z$ and $\phi$, whilst the outer two layers have a $z$ resolution of 35-50 $\mu$m and a $\phi$ resolution of $\sim$15 $\mu$m.

The $dE/dx$ resolution for the SVT is 14%, therefore $K/\pi$ and $K/p$ with a momentum less than 500 MeV$/c$, can be separated with a 2 $\sigma$ significance. Finally, the average track reconstruction efficiency for the SVT is 97%.

## 2.4 The Drift Chamber (DCH)

### 2.4.1 DCH Physics Requirements

The DCH is the primary charged particle detector at *BABAR*. It compliments the measurements of directions and impact parameter of charged tracks from the SVT, and allows extrapolation of the charged tracks into the DIRC, EMC and IFR. The DCH must precisely measure the momenta and track angle for particles with momenta in the range $0.1 < p_t < 5.0$ GeV/$c$. This requires maximal solid angle coverage and good momentum resolution over all momenta. The reconstruction of $B$ and $D$ decays requires a spatial hit resolution of about 140 $\mu$m and the momentum resolution to be $\sigma_{P_T}/p_T < 0.3\%$. The major limiting factor on the track resolution comes from multiple scattering in the DCH. To reduce this effect the amount of material in the DCH is kept to a minimum.

For particles that do not reach the DIRC the DCH provides $dE/dx$ measurements for charged tracks to allow particle identification. This requires a resolution of about 7% to allow $K/\pi$ separation up to $p_t < 700$ MeV/$c$.

*BABAR* has several “golden modes” that are used to study the time dependent CP asymmetry, for example the decay $B \to J/\Psi K^0_s$. The DCH and SVT are the main source of information in the reconstruction of $K^0_s$. In addition, the DCH provides one of the primary triggers for the experiment.

### 2.4.2 DCH Design

The DCH is a 280 cm long cylinder, with an inner radius of 23.6 cm and an outer radius of 80.9 cm. A longitudinal view is shown in Figure 2.8. It is asymmetric about the interaction point to give an increased coverage in the forward direction. It is designed in such a way to reduce the amount of material in front of the forward end of the calorimeter. The forward endplate is made up of 12 mm thick of aluminium whereas, the backward endplate is 24 mm and the electronics are all mounted on the backward endplate. The inner cylinder consists of 1 mm beryllium, which is 0.28% of radiation length ($X_0$), and the outer cylinder is made up of 2 layers of carbon fiber on a honeycomb core,

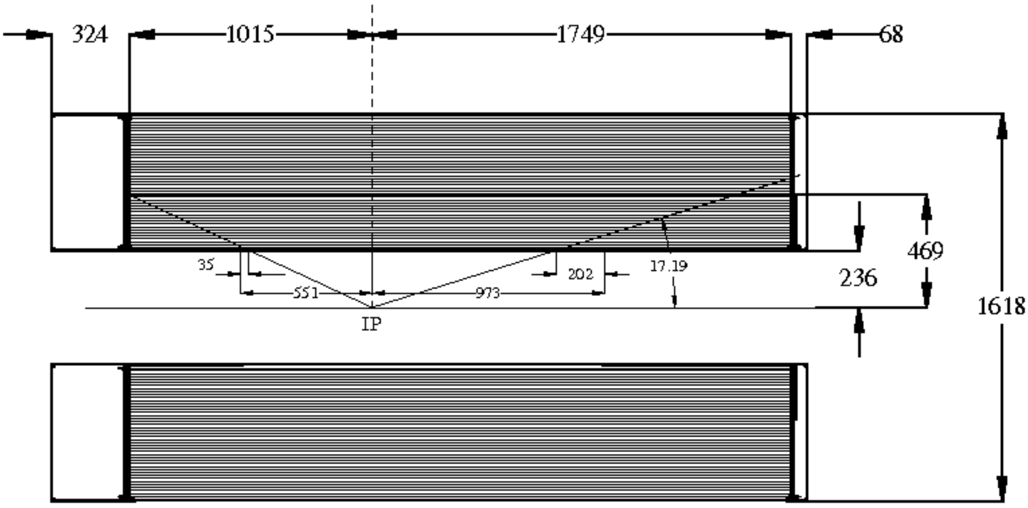

Figure 2.8: Longitudinal view of the DCH.

with 1.5% $X_0$. The chamber is filled with a mixture of helium and isobutane in a ratio of 4:1, chosen for its low mass. The gas mixture has a short drift time of 10-500 ns and good $dE/dx$ and spatial resolution. 0.3% of water vapour is added to the mixture to prolong the life of the chamber. The gas and the wires contribute 0.2% $X_0$ for tracks at normal incidence.

The DCH is built up from 7104 hexagonal drift cells. To minimise the drift time their average size is $1.2 \times 1.8$ cm$^2$. Each cell has a single 20 $\mu$m diameter gold-plated tungsten-rhenium sense wire surrounded by six 120 $\mu$m or 80 $\mu$m gold plated aluminium field wires. The sense wires are at a voltage of between 1900 and 1960 V and the field wires are grounded. The cells form 40 circular layers around the axis of the drift chamber. A "superlayer" is made up of four of these layers, therefore, the DCH is made up of ten superlayers. Each layer is staggered by half a cell with respect to the previous layer. This is beneficial if one of the four signals is missing. Six out of ten of the superlayers are rotated with respect to the $z$-axis to allow longitudinal position measurements. The stereo angle of the superlayers alternates between axial (A) and positive and negative stereo (U,V). They make a pattern AUVAUVAUVA from the inner layer outwards. The stereo angles increase from 45 mrad in the innermost layer to 76 mrad in the outermost layer. The structure of the superlayers ensures the Level 1 trigger can use information from the A layers to make decisions quickly.

When charged particles pass through a cell in the DCH they ionise the gas mixture. This produces electrons that are then accelerated in the electric field. The electrons further ionise the gas as they travel to the sense wire causing a charge avalanche. The leading edge of the signal is detected by the sense wire with a time resolution of $\sim$1 ns. The signal is amplified, digitised and a single bit is sent to the trigger for every A sense wire with a signal. The readout electronics provides a discriminator output for the drift time measurement and a shaped analogue signal for the $dE/dx$ measurement. The $dE/dx$ for a track is calculated by finding the truncated mean of the charge deposited on each sense wire.

### 2.4.3 DCH Performance

The drift time to distance relation and $dE/dx$ are calibrated for each cell in the DCH to remove any bias due to changes in gas pressure or temperature [66]. Charged tracks in the DCH can be defined by 5 parameters ($d_0, \phi_0, w, z_0, tan\lambda$). $d_0$ and $z_0$ parameterise the point of closest approach to the z-axis, $\phi_0$ is the azimuthal angle of the track, $\lambda$ is the dip angle relative to the transverse plane and $w = 1/p_t$ is related to the track curvature. $e^+e^-$ and $\mu^+\mu^-$ events can be used to find the track parameter resolutions. The best values that have been achieved are given below:

$$\begin{aligned} \sigma_{d_o} &= 23\ \mu\mathrm{m}, \quad \sigma_{\phi_0} = 0.43\ \mathrm{mrad} \\ \sigma_{z_0} &= 29\ \mu\mathrm{m}, \quad \sigma_{tan\lambda} = 0.53 \times 10^{-3}. \end{aligned}$$

The resolution of the measured transverse momentum determined from cosmic rays can be written in the form below:

$$\frac{\sigma(p_t)}{p_t} = (0.13 \pm 0.01)\% \times \frac{p_t}{1\mathrm{GeV}/c} \oplus (0.45 \pm 0.03)\%. \qquad (2.4.1)$$

The overall track efficiency is $(96 \pm 1)\%$ for tracks above 200 MeV/$c$ and polar angle $\theta > 500$ mrad. The $dE/dx$ distribution as a function of track momentum

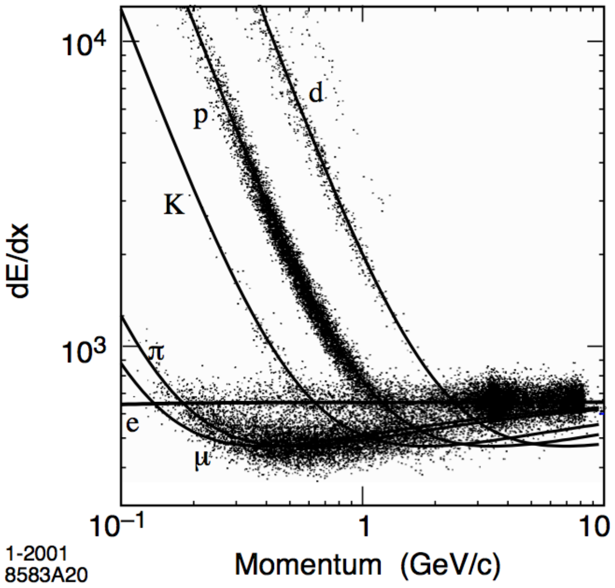

Figure 2.9: $dE/dx$ in the DCH as a function of track momentum for different charged particles.

is shown in Figure 2.9. It can be seen that good momentum separation can be achieved up to 600 MeV/$c$. For $e^+e^-$ events the $dE/dx$ resolution is 7.5%.

## 2.5 The Detector of Internally Reflected Cherenkov Light (DIRC)

### 2.5.1 DIRC Physics Requirements

The DIRC provides the primary particle identification in the detector. One of BABAR's key studies is the measurement of time dependent CP asymmetries. This requires the ability to tag the flavour of one of the $B$ mesons in the event (the one that is not reconstructed in a CP eigenstate). The best way to do this is to use the cascade decay $b \rightarrow c \rightarrow s$ and identify the final charged kaons, which have a momentum up to about 2 GeV/$c$, with most of them below 1 GeV/$c$. The DIRC provides $\pi/K$ separation of 2.5 $\sigma$ or more over a 700 MeV/$c$ - 4.2 GeV/$c$ momenta range, where the high momentum range is essential for

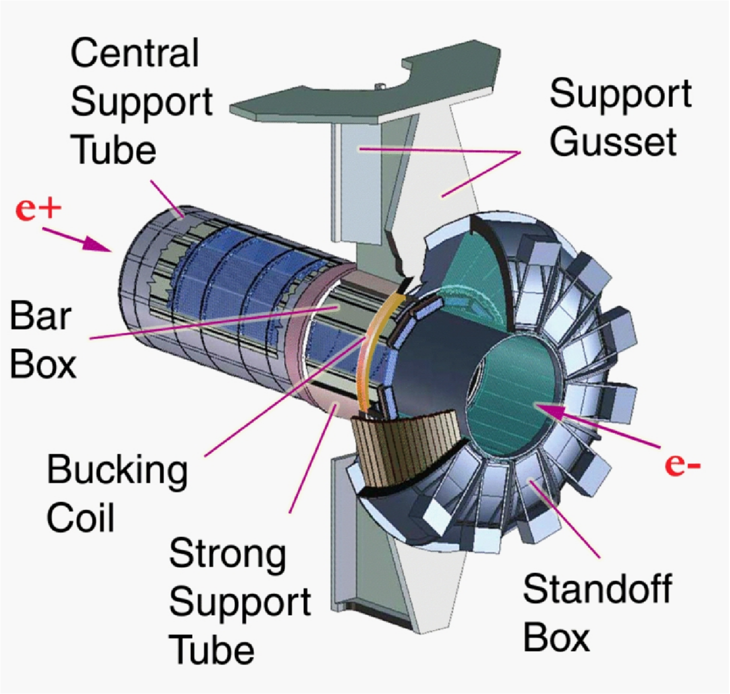

Figure 2.10: Schematic layout of the DIRC.

rare $B$ decay analyses, for example $B \rightarrow K\pi/\pi\pi$ separation. The DCH provides separation up to 700 MeV$/c$, therefore the DIRC must provide complete particle identification over the higher momentum range.

The DIRC must be as small as possible in terms of both physical size and radiation lengths. The first ensures the internal radius of the EMC is small and therefore the cost is minimised. The second constraint is to reduce the impact on the resolution of the EMC due to preshowers. The beams collide every 4.2 ns, therefore, it must have a fast response time to still be effective with high backgrounds.

### 2.5.2 DIRC Design

The DIRC detects Cherenkov radiation and uses the principle that the magnitude of the Cherenkov angle is conserved under internal reflection. A schematic layout is shown in Figure 2.10. The measurement of this angle in addition to the track and momentum information from the DCH allows the particles velocity to be found. A charged particle will emit Cherenkov photons if its velocity is $\beta > 1/n$ when it passes through one of the 144 radiators that are 4.9 m long, 17 mm thick, and 35 mm wide rectangular synthetic fused silica (quartz) bars with refractive index, $n$ = 1.473. The radiation forms a cone of light with angle $\cos(\theta_C) = (\beta n)^{-1}$. The number of photons emitted varies with the polar angle and can range from about 20 at $\theta = 90°$ to $65°$ at large polar angles. The light is carried through internal reflection to the backward end of the bars. The readout devices are only at one end to make room for the EMC forward endcap therefore there are mirrors at the forward ends of the bars to reflect the photons to the readout end. Having reached the backward end the photons enter a region, called the standoff box, filled with purified water, Figure 2.11. Here the Cherenkov image expands until the photons reach the photomultiplier tubes (PMTs) outside of the magnetic field. Purified water has a similar refractive index to that of quartz, therefore minimising the total internal reflection at the boundary. Between the standoff box and the quartz bar there is a wedge of quartz that reflects photons at a large angle relative to the bar axis, thus reducing the size of the PMT detection surface and recovering some of the photons that would have otherwise been lost at the boundary between the bar and standoff box. The 10, 752 PMTs are arranged in an array, each with its own light catcher cone which increases the detection area. There are 16 ways in which the light could have travelled to the PMT: top/bottom, left/right, forward/backward and wedge reflection/no wedge reflection. The correct photon path must be inferred so the original Cherenkov angle can be correctly determined.

### 2.5.3 DIRC Performance

To identify the type of particle ($e, \mu, \pi, K, p$), an unbinned maximum likelihood technique is performed using all the space and time information from the DIRC. The track time of flight and photon propagation time for quartz are both used to calculate the expected arrival time. A likelihood value is calculated for each of the five particle types. The dependance of the measured Cherenkov angle $\theta_C$ in the DIRC on the momentum for different charged particles is shown in Figure 2.12. The angular resolution of a single DIRC photon is 10.2 mrad and the timing resolution is 1.7 ns. For a typical track the Cherenkov angle

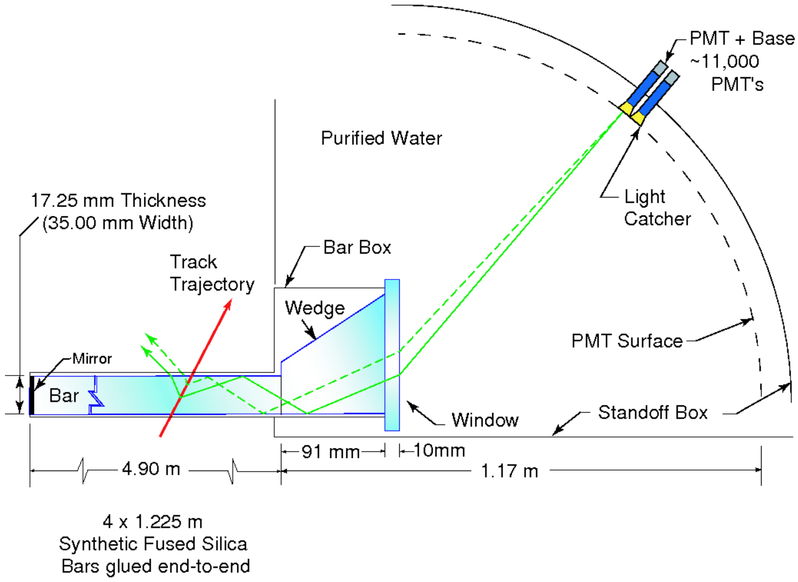

Figure 2.11: Geometry of the DIRC.

resolution is 2.5 mrad, therefore the expected separation between kaons and pions is 2.5 $\sigma$ at 4.2 GeV/$c$ and 4.2 $\sigma$ at 3 GeV/$c$. The parameter $\Delta t$ is defined as the difference between the expected and the measured arrival time. $\Delta t$ can be used to reduce the number of quartz reflection ambiguities and to reject background hits.

## 2.6 The Electromagnetic Calorimeter (EMC)

### 2.6.1 EMC Physics Requirements

The EMC is designed to efficiently detect electromagnetic showers over an energy range of 0.02 to 9 GeV. The lower bound on the energy is due to the need to reconstruct $B$ and $D$ decays that involve $\pi^0$ or $\eta$ particles that decay into photons. Electron identification in the EMC plays an important part in flavour-tagging of neutral $B$ mesons via semi-leptonic decays. It is also important for the study of rare decays of $B$ and $D$ mesons. The upper bound on the energy limit is determined by the desire to measure processes such as $e^+e^- \rightarrow e^+e^-(\gamma)$ and $e^+e^- \rightarrow \gamma\gamma$ which are important for calibration and monitoring luminosity.

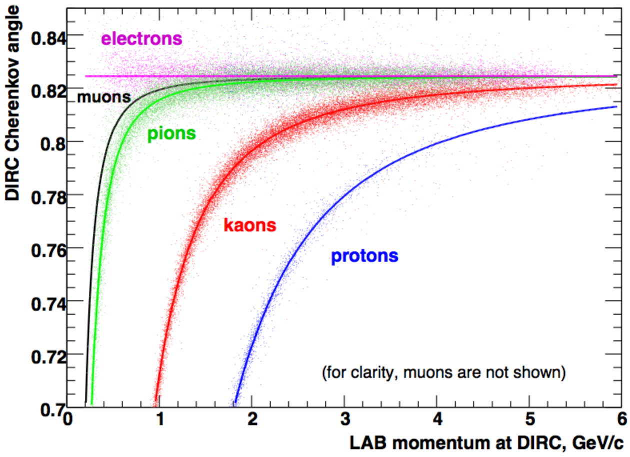

Figure 2.12: DIRC Cherenkov angle versus momentum with curves for various particle hypotheses. Muon points are not shown, however the hypothesis curve is.

### 2.6.2 EMC Design

The EMC is designed to measure the total deposited energy. It is made up of 6580 Caesium Iodide crystals doped with Thallium (CsI(Tl)) arranged in a finely segmented array in a barrel and a forward endcap. The polar angle coverage in the EMC ranges from $\theta = 15.8^\circ$ to $141.8^\circ$, corresponding to 90% of the solid angle in the CM frame. CsI(Tl) was chosen because it has a high light yield and therefore an excellent energy resolution. It also has a small Molière radius that produces high angular resolution. There are 5760 crystals in the barrel, arranged into 48 rows in $\theta$ and 120 rows in $\phi$. The length of the crystals ranges from 29.6 cm ($16X_0$) in the backward to 32.4 cm ($17X_0$) in the forward direction. The difference in length is to limit the effect of shower leakage from high energy particles. There are 820 crystals in the forward endcap, arranged into 8 rows in $\theta$, and with a radiation length of 32.55 cm ($17.5X_0$). A cross sectional view of the top half of the EMC showing the arrangement of the crystals is shown in Figure 2.13. The crystals are not only a scintillating material, but they also act as a light guide. Each crystal is wrapped in 2 layers of tyvek, 165 $\mu$m thick, to reflect the scintillation light. Another layer of aluminium, 25 $\mu$m thick, provides RF shielding.

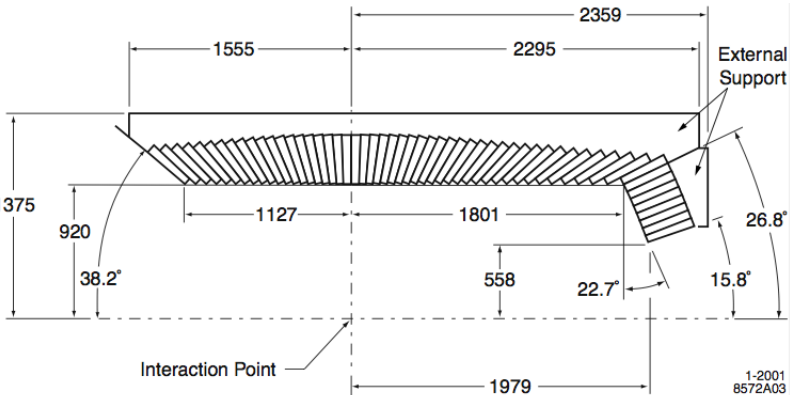

Figure 2.13: Cross sectional view of the top half of the EMC showing the arrangement of the crystals.

An electromagnetic shower will spread over several crystals in a cluster. The scintillation light is collected by two photo-diodes mounted on the rear surface of the crystals. The signal is then amplified and filtered by low-noise preamplifiers before travelling through ribbon cables to the rest of the electronics on the ends of detector. Figure 2.14 shows a schematic of a crystal and preamplifier.

In the barrel the backward 24 rings of crystals are read out to the minicrates at the backward face of the detector and the forward 24 rings are read out to the minicrates at the forward end of the detector. The endcap crystals are read out to the minicrates adjacent to them on the forward face. Each barrel minicrate contains 6 Analogue-to-Digital Boards (ADB), and each endcap minicrate contains 4 ADBs, every ADB reads 12 crystals. An ADB contains 3 Custom AutoRange Encoding (CARE) chips that amplify the signal for 4 of the crystals and select one of the four different 12-bit ADC ranges. The signal from a minicrate of ADBs is then passed on to the Input-Output-Boards (IOB), from there the signal travels through optical fibres to the Readout Modules (ROMs) that are in the electronics hut. Energy sums from towers are passed into the Level 1 trigger from the ROMs, where they are processed to find the total energy and peak time.

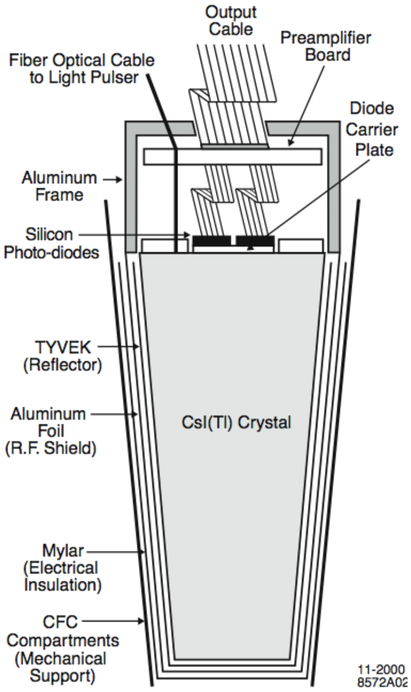

Figure 2.14: Diagram of an CsI(Ti) crystal.

### 2.6.3 EMC Performance

There are two relationships that have to be parameterised in order to correctly calibrate the EMC [67, 68]. The first is the relationship between the measured signal in a crystal and the true energy that was deposited. This is determined by a single crystal constant calibration. At low energies it is found by the source calibration. A d-t (deuterium-tritium) generator tube generates neutrons that irradiate fluorinert liquid to produce $^{16}O^{*}$. The fluorinert is carried in tubes across the front faces of all the crystals where the $^{16}O^{*}$ decays and generates photons with energy 6.13 MeV. This gives a low energy absolute calibration point with $\sigma_E/E = (5.0 \pm 0.8)\%$. At high energies Bhabha events are used to calibrate the crystals. The energy of the $e^{+}$ and $e^{-}$ events can be calculated from their polar angles. The measured energy resolution is $\sigma_E/E = (1.90 \pm 0.07)\%$ at 7.5 GeV. Throughout the lifetime of the experiment the radiation will damage the crystals and alter this relationship.

The second relationship is between the cluster energy and the energy of the electromagnetic showers, as well as the angular resolution of the EMC. This relationship parametises effects on the deposited energy in the crystals from absorption in material in front of the EMC and between crystals, and leakage of energy out of the back of the crystals. This relationship is determined by a shower calibration. Control samples of BhaBha scattering, $\pi^0 \rightarrow \gamma\gamma$, $e^+e^- \rightarrow \mu+\mu^-\gamma$, and $\eta \rightarrow \gamma\gamma$ decays are used to determine the energy resolution, shown in Figure 2.15. The resolution can be expressed as:

$$\frac{\sigma_E}{E} = \frac{(2.32 \pm 0.30)\%}{\sqrt[4]{E(GeV)}} \oplus (1.85 \pm 0.12)\%.$$

Angular resolution improves as $E^{-\frac{1}{2}}$ up to a limit of ~2 mrad at 3 GeV. The lateral shower shape can be used to discriminate between electromagnetic showers and hadrons. It is defined as:

$$LAT = \frac{\sum_{i=3}^{N} E_i r_i^2}{\sum_{i=3}^{N} E_i r_i^2 + E_1 r_0^2 + E_2 r_0^2} \tag{2.6.1}$$

where N is the number of crystals associated with a shower, $E_i$ is the energy deposited in the $i$-th crystal, $r_i$ is the lateral distance from the center of the shower and the $i$-th crystal, and $r_0$ is the average distance between the two central crystals.

## 2.7 The Instrumental Flux Return (IFR)

### 2.7.1 IFR Physics Requirements

The IFR is the primary detector for muons and aids in the identification of long-lived neutral hadrons such as the $K_L^0$. The muon identification is essential for flavour tagging, and when studying semi-leptonic decays and rare decays of $B$ and $D$ mesons. The IFR must have an efficiency of greater than 90% when detecting muons and the pion misidentification rate should be a maximum of 2-3% over a momentum range of $1.5 < p < 3.0$ GeV/$c$.

Initially, Resistive Plate Chambers (RPCs) were used throughout the entire IFR

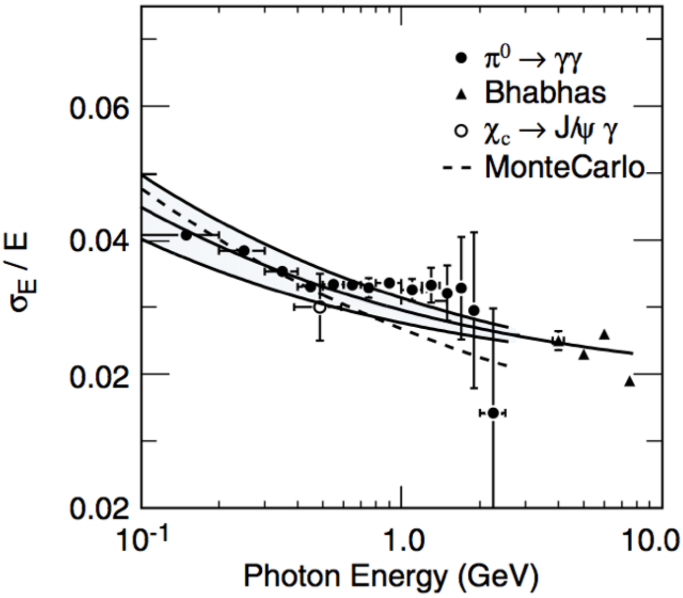

Figure 2.15: Energy resolution for the EMC for photons from different decay modes.

but after a few months of running the detectors their efficiency was badly degraded. The forward endcap was refitted in 2002 with improved RPCs. The RPCs in the barrel were partially replaced in 2005 with Limited Streamer Tubes (LST) and the remainder of the barrel was replaced in 2006. The backward endcap was left because its acceptance in the CM frame is small, therefore the incentive to replace it was not as great. After all the work was completed the IFR once again met the physics requirements.

### 2.7.2 IFR Design

The IFR is made up of a hexagonal barrel as well as forward and backward endcaps, Figure 2.16. Originally the barrel was made up of 19 layers of steel and RPCs and the endcaps were made up of 18 layers. The steel reduces the effect of pion misidentification by acting as a hadron absorber. The chambers are made of 2 mm bakelite sheets, each with a 2 mm separation from the next and kept at a potential of 8000 V, Figure 2.17. To prevent any dark current or discharges in the gas, linseed-oil was used to coat the bakelite. The space between

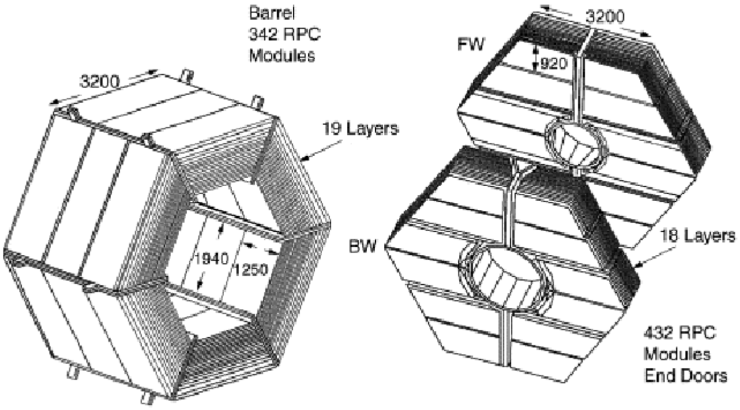

Figure 2.16: IFR barrel and endcap

the sheets is filled with a non-flammable gas mixture (56.7% argon, 38.8% freon 134a and 4.5% isobutane). High-energy particles cause an avalanche to turn into a streamer (electrical discharges in the gas) that is detected in the RPCs and readout. Although the technology had been tested, after only a short time of running the amount of dark current had increased dramatically making large areas of the detector very inefficient thus greatly reducing the muon identification rate. It was found that high temperatures caused the linseed oil to collect and bridge the gap between the different layers leading to high levels of dark current. When the forward endcap was refitted additional cooling was added and the new RPCs had thinner layers of linseed oil and were more thoroughly tested before being fitted.

In 2005 in two sextants of the barrel the RPCs were replaced with LSTs and in 2006 the remaining sextants were replaced. The barrel is now made up of 12 layers of LSTs, 6 layers of brass and the remaining layer of steel. The layers of brass were fitted to improve hadron absorption. The LSTs are about 3.5 m long and made up of eight 15 mm by 17 mm cells. Each cell is covered in graphite and has a 100 $\mu$m gold-plated beryllium-copper wire at a voltage of 5500 V. All of the above is contained in a PVC sleeve. The gas mixture is different from the RPCs and is made up of 3.5% argon, 8% isobutane and 88.5% carbon dioxide.

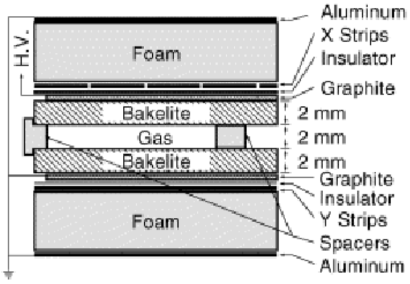

Figure 2.17: Schematic drawing of a *BABAR* RPC

### 2.7.3 IFR Performance

Figure 2.18 shows the IFR performance before and after the replacement of the RPCs. The LSTs have been performing well since their installation, with a failure rate of below 0.5%. The efficiencies of all layers are now at the level of 90%. The muon identification has improved dramatically thus allowing more precise measurements of decays with muons [69].

## 2.8 Trigger

The electronics for each of the subsystems are capable of collecting data in realtime, this data is extensively buffered to avoid any deadtime losses while making the trigger decisions. The *BABAR* trigger is a two level trigger and is designed to reject background events and retain physics events.

The Level 1 trigger is a hardware trigger designed to select events based on simple detector signals and has a maximum acceptance rate of about 5.0 kHz. Not all of the sub-detectors contribute, only the DCH, EMC and IFR provide information to the Level 1 trigger. Input parameters to the Level 1 trigger include the track segments from the DCH, energy deposited in the EMC and hits in the IFR. If the Level 1 trigger requirements are met the event is then passed to the Level 3 trigger.

The Level 3 trigger is a software trigger that is designer to further reject the

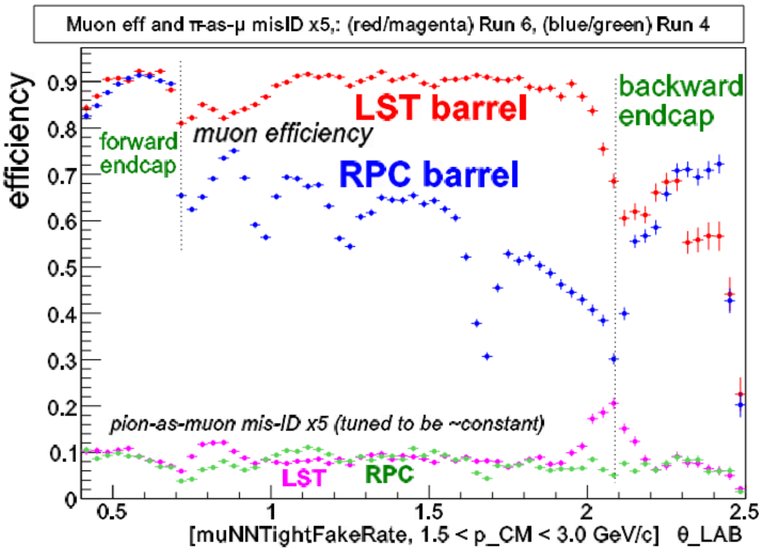

Figure 2.18: Muon efficiency before the LSTs (blue) and after the LST upgrade (red) and pion misID before the LSTs (green) and after the LST upgrade (magenta).

background events without the loss of physics events. This trigger uses information from all sub-detectors such as track counting and primary vertex in the SVT to reduce the amount of data. The Level 3 trigger selects the events to be written to mass storage at a rate of no more than 100 Hz, as required by the online computing system.

The trigger is designed to not only be highly efficient at recording physics events but to also retain BhaBha events that are used to calibrate the EMC and to select random samples of the beam backgrounds. The trigger rates for different event types at the $\Upsilon(4S)$ are listed in Table 2.2. Once the data has passed the Level 1 and Level 3 triggers it is sent to the online event processing computing farm that is used to check the quality of the data and monitor the hardware of the sub-detectors.

At this stage the data can be passed through a set of algorithms that select the physics events of interest. The techniques used to extract the $B \rightarrow K^{*}l^{+}l^{-}$ events are described in detail in Chapter 3.

| Event type | Cross-section (nb) | Production Rate (Hz) | L1 Trigger Rate (Hz) |
|---|---|---|---|
| $b\bar{b}$ | 1.10 | 3.2 | 3.2 |
| other $q\bar{q}$ | 3.4 | 10.2 | 10.1 |
| $\tau^+\tau^-$ | 0.94 | 2.8 | 2.4 |
| $\mu^+\mu^-$ | 1.16 | 3.5 | 3.1 |
| $e^+e^-$ | $\sim 40$ | 159 | 156 |

Table 2.2: The cross section of an event, the rate at which it is produced and the rate at which it passes the Level 1 trigger for the $\Upsilon(4S)$.

# 3

# Event Selection

This chapter describes the reconstruction and selection of signal events. The selection for the Run 5 analysis (384 million $B\overline{B}$s), will be discussed in Section 3.1 to 3.9. The selections have been re-optimised for the Run 6 analysis using the full BABAR dataset of 468 million $B\overline{B}$, to account for the increase in data and improvements in the performance of the detector. These selections will be discussed in Section 3.10 onward, highlighting any changes to the previous analysis and the justification for these changes.

The signal modes are reconstructed from their decay products which are detected as clusters of energy or as charged tracks in the sub-detectors. Pions, kaons and leptons are identified by combining the information from each of the sub-systems and using multi-variate techniques, such as likelihood ratios, neural networks or boosted decision trees. This chapter describes the identification process for each of the different particles as well as final event selection details.

## 3.1 Reconstructed Modes

There are six decay modes that are measured in the Run 5 analysis:

- $B^+ \rightarrow K^{*+}l^+l^-$ where $K^{*+} \rightarrow K^+\pi^0$ and $\pi^0 \rightarrow \gamma\gamma$

- $B^+ \to K^{*+}l^+l^-$ where $K^{*+} \to K^0_S\pi^+$ and $K^0_S \to \pi^+\pi^-$
- $B^0 \to K^{*0}l^+l^-$ where $K^{*0} \to K^+\pi^-$

where the $l^+l^-$ are dilepton pairs and can be either $e^+e^-$ or $\mu^+\mu^-$. Charge conjugation is implied unless otherwise stated. The $B^\pm \to K^\pm l^+l^-$ modes are reconstructed, but are only used as a control sample. There are also lepton number violating, $B \to K^* e^\pm\mu^\mp$, and charmonium, $B \to J/\Psi(\text{or } \Psi(2S))K^*$, control samples.

## 3.2 Monte Carlo Samples

Monte Carlo (MC) samples are used throughout this analysis in order to study reconstruction efficiencies, expected signal and background shapes and fitting techniques. The MC samples are generated to be in the same form as the BABAR data. Therefore, every selection that is described will be applied to both MC and the BABAR data. The MC is produced using two packages: GEANT4 [70] simulates the BABAR detector and the behaviour of the particles as they travel through the detector; EvtGen generator [71] simulates the decays of the $B$ mesons and continuum hadronic events; PHOTOS [72] generates QED effects.

A higher luminosity of MC can be generated compared to the raw data collected by the detector. The larger statistics allows processes with low cross sections to be better understood. There were three main types of MC that were generated for this analysis, the number of events generated for each of the samples compared to the BABAR data are listed in Tables 3.1, 3.2 and 3.3:

- ″generic“ $B\overline{B}$ background to study the random combinatoric background from $B$ mesons.
- ″generic“ $uds$ and $c\overline{c}$ backgrounds to study the random combinatoric background from continuum events.
- ″Exclusive signal“ for each of the signal decay mode final states and for the $J/\Psi$ and $\Psi(2S)$ resonances.

| Mode | BF($10^{-6}$) | Events | Data/MC (/$10^{-3}$) |
|---|---|---|---|
| $K^+\pi^-e^+e^-$ | 1.58 | 587000 | 0.29 |
| $K^+\pi^-\mu^+\mu^-$ | 1.19 | 901000 | 0.14 |
| $K^0_s\pi^+e^+e^-$ | 1.48 | 587000 | 0.78 |
| $K^0_s\pi^+\mu^+\mu^-$ | 1.11 | 901000 | 0.38 |
| $K^+\pi^0e^+e^-$ | 1.58 | 587000 | 0.42 |
| $K^+\pi^0\mu^+\mu^-$ | 1.19 | 901000 | 0.21 |

Table 3.1: Number of simulated signal events by mode and their ratio to the number of $B\overline{B}$ decays in data. The branching fractions are taken from the previous BABAR analysis [73].

| Mode | BF($10^{-3}$) | Events | Data/MC (/$10^{-3}$) |
|---|---|---|---|
| $J/\Psi K^+\pi^-$ | 0.8 | 11670000 | 4.22 |
| $J/\Psi K^+\pi^0$ | 0.47 | 11590000 | 2.25 |
| $J/\Psi K^0_s\pi^+$ | 0.32 | 11670000 | 1.55 |
| $\Psi(2S)K^+\pi^-$ | 0.48 | 1164000 | 2.87 |
| $\Psi(2S)K^+\pi^0$ | 0.21 | 1164000 | 1.33 |
| $\Psi(2S)K^0_s\pi^+$ | 0.14 | 1164000 | 0.92 |

Table 3.2: Number of simulated charmonium events by mode and their ratio to the number of $B\overline{B}$ decays in data.

| Mode | Cross-sec. (nb) | Events | Data/MC |
|---|---|---|---|
| Generic $B^+B^-$ | 0.525 | 555572000 | 0.33 |
| Generic $B^0\overline{B^0}$ | 0.525 | 552414000 | 0.33 |
| Continuum $c\bar{c}$ | 1.30 | 591198000 | 0.77 |
| Continuum $uds$ | 2.05 | 695820000 | 1.03 |

Table 3.3: Number of simulated generic events and scaling to the number of $B\overline{B}$ decays, or for the continuum events to the appropriate cross-section.

## 3.3 Particle Identification

In order for a candidate to be reconstructed as a $B \rightarrow K^{(*)}l^{+}l^{-}$ signal event, it must have well reconstructed tracks and photons [74]. Charged tracks must have a distance-of-closest approach (doca) to the primary vertex of less than 1.5 cm in the $x-y$ plane and less than 10 cm in the $z$ direction. Leptons must have a minimum of 12 hits in the DCH and are required to pass particle identification. There is strict particle identification for kaons. The charged pions from the $K^{*}$ candidate must fail the kaon identification requirements. Photons must deposit a minimum energy of 30 MeV in the EMC and must not be associated with tracks in the DCH.

### 3.3.1 Electron Identification

The electrons must have a momentum greater than 300 MeV/c. They are identified using a likelihood ratio combining the following information from the EMC, DIRC and DCH:

- The ratio $E/p$ of the shower energy deposited in the EMC to the track momentum measured in the DCH.
- The shower shape of the cluster in the EMC.
- The difference between the $dE/dX$ measured in the DCH and the expected $dE/dX$ for an electron.
- The Cherenkov angle $\theta_C$ measured in the DIRC.

Bremsstrahlung radiation occurs when high energy electrons emit photons. The Bremsstrahlung radiation is recovered by combining the electron candidate with any nearby photons. The photons must lie within an angular region in the polar angle $|\theta_e - \theta_\gamma| < 35$ mrad and within azimuth angle ($\phi_0^{e-} - 50$ mrad) $< \phi_\gamma < \phi_{cent}^{e-}$ and $\phi_{cent}^{e+}$ mrad $< \phi_\gamma <$ ($\phi_0^{e+} + 50$ mrad). Where, $(\theta_0, \phi_0)$ is the initial direction of the electron track evaluated at the interaction point and $(\theta_{cent}, \phi_{cent})$ is the centroid position of the shower in the calorimeter. This ensures that the electrons are reconstructed to have the correct energy.

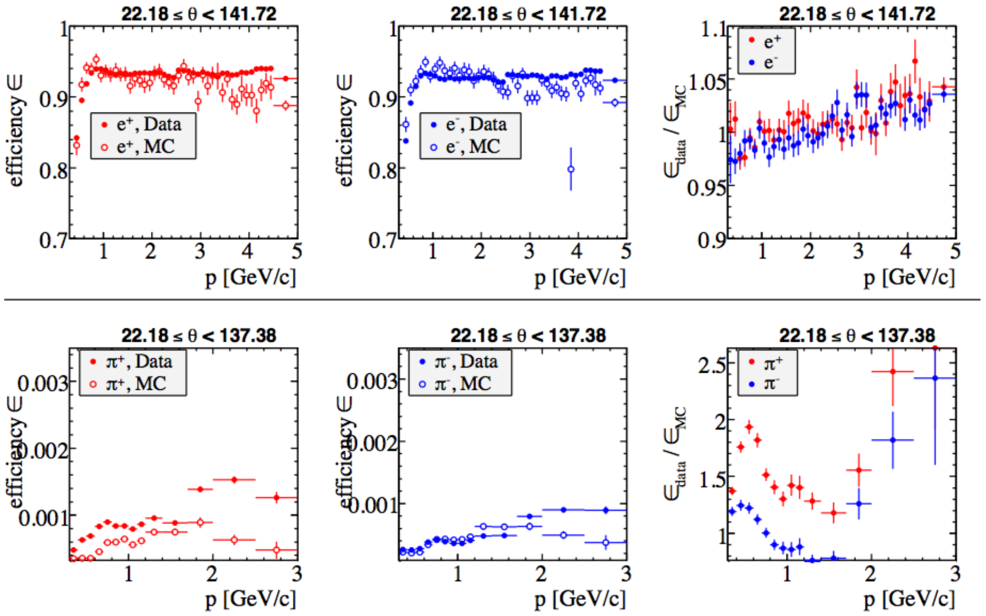

Figure 3.1: Electron selection efficiency as a function of momentum (top). Pion misidentification rate of the electron selector (bottom).

Radiative $e^+e^- \rightarrow e^+e^-\gamma$ events are used to evaluate the electron selection efficiency. Pion misidentification is determined from $\tau$ and $K_S^0$ decays. The selection efficiency from the likelihood function is above 92%, with a pion misidentification rate of less than 2%, Figure 3.1.

### 3.3.2 Muon Identification

Muons are identified by using information from the DCH, EMC and IFR as an input to a neural network algorithm [75]. The muons most distinguishing feature is their penetrating depth in the IFR. The following quantities are needed:

- The energy deposited in the EMC.
- The goodness of fit with respect to the track extrapolation from the DCH.
- The number of measured interaction lengths of the muon candidate in the IFR.

- The difference between the number of interaction lengths and the number of interaction lengths expected for a muon candidate.
- The standard deviation of the average IFR strip multiplicity.
- The average multiplicity of the strip hits per layer.
- The goodness of fit ($\chi^2/dof$) of a third order polynomial fit to the hits in the three-dimensional cluster.
- The continuity of the track in the IFR, which is defined as:

  $$\text{continuity} = \frac{\mathrm{N}_{\text{layers}}}{\mathrm{L}_{\text{last}} - \mathrm{L}_{\text{first}} + 1},$$

  where $\mathrm{L}_{\text{first}}$ is the innermost layer hit, $\mathrm{L}_{\text{last}}$ is the outermost layer hit, and $\mathrm{N}_{\text{layers}}$ is the total number of layers hit in a three-dimensional cluster.

The efficiency of the muon being correctly identified is found by studying the control sample $e^+e^- \to \mu^+\mu^-\gamma$. Pions are most often misidentified as muons; this rate can be evaluated by examining a control sample from clean $D^*$ decays. Different neural network outputs correspond to different levels of muon efficiency and pion rejection. For this analysis a strict muon selection was imposed, corresponding to an efficiency of about 70% for a muon momenta above 1 GeV/$c$, with a pion misidentification of 2-3%, Figure 3.2.

### 3.3.3 K and $\pi$ Identification

Information from the SVT, DCH and DIRC is combined into a likelihood function:

$$L_K = L_K^{SVT} \times L_K^{DCH} \times L_K^{SVT}$$

The required quantities are:

- The difference between the $dE/dx$ measured in the DCH and the expected $dE/dx$ if a kaon candidate is assumed.

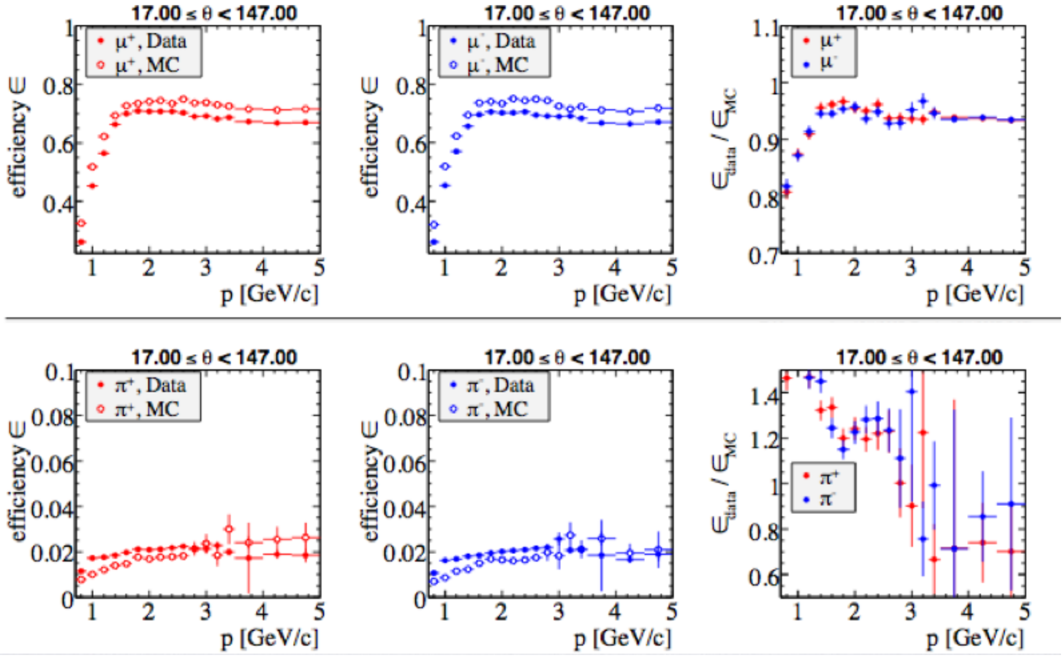

Figure 3.2: Muon selection efficiency as a function of momentum (top). Pion misidentification rate of the muon selector (bottom).

- The difference between the $dE/dx$ measured in the SVT and the expected $dE/dx$ if a kaon is assumed.
- The Cherenkov angle $\theta_C$ measured in the DIRC.
- The number of observed photons in the DIRC.
- The quality of the track prior to reaching the DIRC.

Kaons are also required to fail the electron identification algorithm in Section 3.3.1. The efficiency of the kaon selection is determined from the decay $D \rightarrow K\pi$, where the $D$ is a daughter product from a $D^*$ decay. Kaons are most frequently misidentified as pions, the same $D$ decays can be used to evaluate this rate. The kaon efficiency for most of the momentum range is more than 80% and the misidentification rate from pion is 2-3%, shown in Figure 3.3. The pions are required to fail the kaon selection.

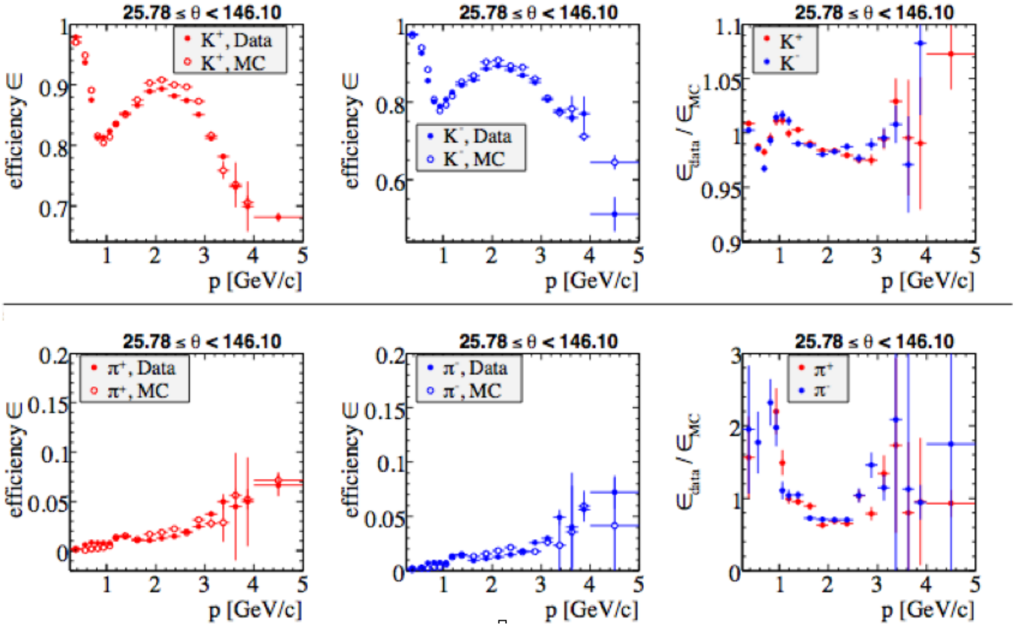

Figure 3.3: Kaon selection efficiency as a function of momentum (top). Pion misidentification rate of the kaon selector (bottom)

## 3.4 Kinematic Selection

The $B$ meson candidates are reconstructed by combining the daughter products of the decay. The $B$ meson must meet the following requirements:

- Electron momentum: $p_{LAB} \geq 0.3$ GeV$/c$.
- Muon momentum: $p_{LAB} \geq 0.7$ GeV$/c$.
- $K_S^0$ candidates must satisfy $0.4887 < M_{\pi\pi} < 0.5073$ GeV$/c^2$.
- $\pi^0$ candidates must pass the following cuts to the photons:
  - $0.115 < M_{\gamma\gamma} < 0.150$ GeV$/c^2$
  - $E_\gamma > 0.05$ GeV
  - $LAT_\gamma < 0.9$

The following two nearly uncorrelated kinematic quantities:

$$m_{ES} = \sqrt{\frac{s}{2} + \frac{(p_0.p_B)^2}{E_0^2} - p_B^2} \tag{3.4.1}$$

$$\Delta E = E_B^* - \frac{\sqrt{s}}{2} \tag{3.4.2}$$

are used to distinguish $B \to K^{(*)}l^+l^-$ events from other $B$ decays, where $\sqrt{s}$ is the total center-of-mass (CM) energy, $E_0$ and $p_0$ are the energy and momentum of the $\Upsilon(4S)$ in the lab frame, $p_B$ is the $B$ momentum in the lab frame, and $E_B^*$ is the $B$ energy in the CM frame. A correctly reconstructed decay will result in an $m_{ES}$ equal to the mass of the $B$ meson and $\Delta E \sim 0$. For decay modes that contain a $K^*$ in the final state, requirements on the mass of the $K\pi$ ($m_{K\pi}$) can be used to constrain the mass of the daughter candidates.

## 3.5 Kinematic Regions

- The fit region is defined by:
  - $5.2\ \mathrm{GeV}/c^2 < m_{ES} < 5.29\ \mathrm{GeV}/c^2$
  - $-0.08 < \Delta E < 0.05\ \mathrm{GeV}$
  - $0.82\ \mathrm{GeV}/c^2 < m_{K\pi} < 0.97\ \mathrm{GeV}/c^2$ for $K^*l^+l^-$ modes
- The signal region is used for the measurements of the angular variables. The signal region is defined by:
  - $5.27\ \mathrm{GeV}/c^2 < m_{ES} < 5.29\ \mathrm{GeV}/c^2$
  - $-0.08 < \Delta E < 0.05\ \mathrm{GeV}$
  - $0.82\ \mathrm{GeV}/c^2 < m_{K\pi} < 0.97\ \mathrm{GeV}/c^2$ for $K^*l^+l^-$ modes
- The sideband region is a wide region that surrounds but excludes the signal region. This region is primarily dominated by the combinatoric background and is useful for studying these background events. The region used is:
  - $5.2\ \mathrm{GeV}/c^2 < m_{ES} < 5.27\ \mathrm{GeV}/c^2$

- $\Delta E < -0.08$ GeV and $\Delta E > 0.05$ GeV
- $0.82$ GeV$/c^2 < m_{K\pi} < 0.97$ GeV$/c^2$ for $K^* l^+ l^-$ modes

## 3.6 Background Suppression

There are two types of backgrounds that are relevant to this analysis: combinatoric backgrounds that have approximately flat distributions in $m_{ES}$ and $\Delta E$; and other backgrounds that peak in at least one of these variables. A neural network is used to suppress the combinatoric background and the remaining background is modelled using the $m_{ES}$ sideband region in data. There are two sources of peaking events that are removed by vetoes: $B \to J/\Psi(\Psi(2S))K^{(*)}$ where the $J/\Psi$ or $\Psi(2S)$ decay into $l^+l^-$; and $B \to K^{(*)}h^+h^-$, where $h$ is a kaon or pion. These events are predominantly from $B \to D\pi$ decays where the $D \to K^*\pi$ and the pions are misidentified as muons. The remaining peaking background is modelled using data or Monte Carlo samples.

### 3.6.1 Combinatoric Background

Combinatoric background includes continuum events from $uds$, $c\bar{c}$ and $B\overline{B}$. The neural networks are trained using the MC samples in Section 3.2, after they have passed all of the selection criteria. In order to remove as many combinatoric events as possible the neural networks are trained for each of the signal modes, and in both the high and low di-lepton mass regions defined in Table 1.6.

Event shape variables are used to categorise an event. $B$ decays tend to be spherical, whereas continuum events are more jet-like in the LAB frame. The following variables are inputs to the neural network [76]:

- The ratio of Fox-Wolfram moments $R_2 = H_2/H_0$ [77], computed in the CM using all tracks and neutral clusters in the event.
- The ration of Legendre moments $L_2/L_0$ [78], computed in the CM using all tracks and neutral clusters in the event.

- The $m_{ES}$ of the rest of the event (ROE), $m_{ES}^{ROE}$, computed in the LAB frame by summing all tracks and neutral clusters which are not used to reconstruct the signal candidate.
- The $\Delta E$ of the ROE, $\Delta E^{ROE}$, computed in the CM from the same recoiling $B$ candidate used in the calculation of $m_{ES}^{ROE}$.
- The magnitude of the total transverse vector momentum of an event, computed in the lab frame using all tracks and neutral clusters.
- The distance of closest approach along the $z$-axis to the primary interaction point by the di-lepton system.
- The distance of closest approach in the $xy$-plane to the primary interaction point by the di-lepton system.
- The vertex probability of the $B$ candidate.
- The vertex probability of the di-lepton system.
- The value $\cos\theta_B$, where $\theta_B$ is the angle between the $B$ candidate's momentum and the $z$ axis in the CM frame.
- The value $\cos\theta_{thrust}$, where $\theta_{thrust}$ is the angle between the event's thrust axis and the $z$ axis in the CM frame.
- The value $\cos\theta_{thrust}^{ROE}$, where $\theta_{thrust}^{ROE}$ is the angle between the ROE thrust axis and the $z$ axis in the CM frame.
- The value $\Delta\cos\theta_{thrust}$, which is the cosine of the opening angle in the CM frame between the angles which are the arguments of the $\cos\theta_{thrust}^{ROE}$ and the $\cos\theta_{thrust}$.

### 3.6.2 Peaking Background - Charmonium Vetoes

The charmonium resonances are the largest source of peaking background, with a branching fraction that is 1000 times larger than $B \rightarrow K^{(*)}l^+l^-$. The events are vetoed, but they do provide an excellent control sample in Section 5.1. In the electron modes the $J/\Psi$ events are removed by the following three vetoes in the $\Delta E - m_{ll}$ plane, Figure 3.4:

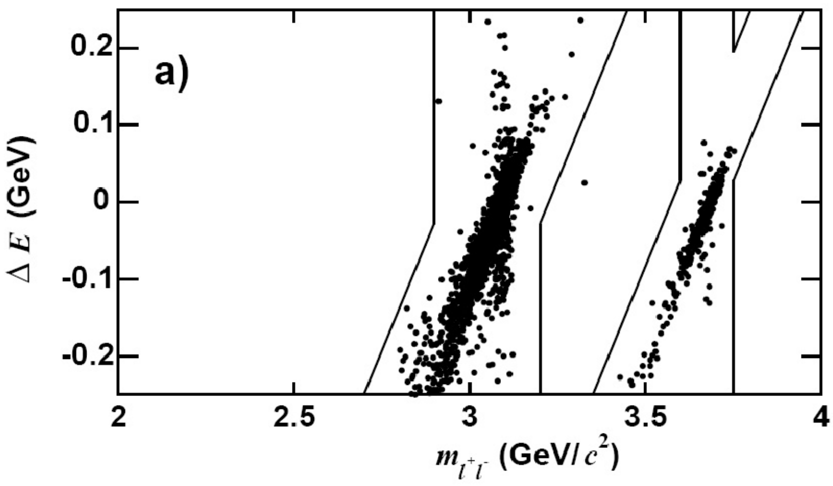

Figure 3.4: $B^+ \to K^+e^+e^-$ Charmonium Veto Region.

- 2.90 < $m_{ll}$ < 3.20 GeV/$c^2$.
- For $m_{ll}$ > 3.20 GeV/$c^2$: 1.11$m_{ll}$− 3.58 < $\Delta E$ < 1.11$m_{ll}$− 3.25 GeV.
- For $m_{ll}$ < 2.90 GeV/$c^2$: $\Delta E$ < 1.11$m_{ll}$− 3.25 GeV.

In the muon modes the following three regions of the $\Delta E - m_{ll}$ planes are vetoed to remove $J/\Psi$ events:

- 3.00 < $m_{ll}$ < 3.20 GeV/$c^2$.
- For $m_{ll}$ > 3.20 GeV/$c^2$: 1.11$m_{ll}$− 3.53 < $\Delta E$ < 1.11 $m_{ll}$− 3.31 GeV.
- For $m_{ll}$ < 3.00 GeV/$c^2$: $\Delta E$ < 1.11$m_{ll}$− 3.31 GeV.

The $\Psi(2S)$ events are removed from both electron and muon modes using the following vetoes:

- 3.60 < $m_{ll}$ <3.75 GeV/$c^2$.
- $m_{ll}$ > 3.75 GeV/$c^2$: 1.11$m_{ll}$− 4.14 < $\Delta E$ < 1.11$m_{ll}$− 3.97 GeV.
- For $m_{ll}$ < 3.60 GeV/$c^2$: $\Delta E$ <1.11$m_{ll}$− 3.97 GeV.

### 3.6.3 Peaking Background - $B \to D\pi$ Vetoes

If both pions in $B \to D(\to K^*\pi)\pi$ are misidentified as muons this produces a peaking background for both $Kll$ and $K^*ll$ modes. For the $Kll$ modes a triple fake can occur, where the charged kaon and the oppositely charged pion are misidentified as muon and the second pion is misidentified as a kaon.

This background only occurs in the di-muon modes due to the higher misidentification rate for pions. The invariant mass of the $K^*\mu$ is calculated assuming the muon is a pion, if the mass is between 1.84 and 1.90 GeV/$c^2$ the event is vetoed. The triple fakes are vetoed in a similar way but assuming one of the muons to be a kaon and the other is a pion.

### 3.6.4 Multiple Candidate Vetoes

Once all of the above selections have been applied, $\sim 1-2\%$ of the events have more than one reconstructed $B$ candidate per event. This generally occurs more frequently for the $K^*$ modes and is up to $20\%$ for the $\pi^0$ modes. To select the final candidate the following criteria must be met:

- For $B^\pm \to K^\pm l^+ l^-$: the selected candidate must have the largest number of DCH hits on the $K^\pm$ track.
- For $B^0 \to K^{*0} l^+ l^-$, $K^{*0} \to K^+\pi^-$ and $B^{*+} \to K^{*+} l^+ l^-$, $K^{*+} \to K_s\pi^+$: the selected candidate must have the largest number of SVT hits on the $\pi^\pm$ track.
- For $B^+ \to K^{*+} l^+ l^-$, $K^{*+} \to K^+\pi^0$: the selected candidate must have the mass of its $\pi^0$ closest to 135 MeV/$c^2$.
- If there are still more than one candidate for an event, the first candidate to be found is chosen.

## 3.7 Optimization

The last stage of the event selection is to optimise the cuts on the neural network and $\Delta E$ selections in each di-lepton mass region to get the highest signal significance. In the Run 5 analysis it was found that trying to make measurements in four bins of $q^2$ was too optimistic. The $q0$ and $q1$ bins were concatenated into a single "low" bin, $0.1 < q^2 < 6.5$ GeV$^2/c^4$, and the $q2$ and $q3$ bins form a "high" bin, $q^2 > 10.24$ GeV$^2/c^4$. The neutral network selections and the $\Delta E$ window were varied for each mode and the hadronic mass is also varied for the $K^*$ modes. The figure of merit $S/\sqrt{S+B}$, where $S$ and $B$ are the number of signal and combinatoric background events is calculated in the region $m_{ES} >$ 5.27 GeV$^2/c^4$. The cuts that produced the highest signal significance are used in the final analysis.

## 3.8 Efficiency

After all the optimisation has been fixed the selection efficiency can be found. The efficiency is calculated by dividing the number of signal Monte Carlo events that pass the event selection by the number of events that are generated. The efficiencies for each mode and $q^2$ bin are shown in Table 3.4.

## 3.9 Expected Signal and Background Yields

The expected number of signal and background yields are calculated assuming the previous BABAR measurement of the branching fraction [79] and using the efficiency calculated above then scaling to a luminosity of 348 fb$^{-1}$. Table 3.5, shows the expected yield for each of the modes and Table 3.6 shows the yields after the $K^*$ and $K$ modes are concatenated, where the signal region is defined as 5.27 $< m_{ES} <$ 5.29 GeV$/c^2$ and the fit region is $m_{ES} >$ 5.2 GeV$/c^2$ .

| Mode | $q^2$ bin | Reconstruction Efficiency (%) |
|---|---|---|
| $B^+ \to K^+\mu^+\mu^-$ | q0 | $6.2 \pm (6.8 \times 10^{-4})$ |
| | q1 | $14.0 \pm (6.8 \times 10^{-4})$ |
| | q2 | $15.3 \pm (1.3 \times 10^{-3})$ |
| | q3 | $15.4 \pm (1.0 \times 10^{-3})$ |
| $B^+ \to K^+e^+e^-$ | q0 | $21.6 \pm (1.1 \times 10^{-3})$ |
| | q1 | $21.8 \pm (8.4 \times 10^{-4})$ |
| | q2 | $21.3 \pm (1.5 \times 10^{-3})$ |
| | q3 | $19.5 \pm (1.1 \times 10^{-3})$ |
| $B^+ \to K^+\pi^0\mu^+\mu^-$ | q0 | $1.5 \pm (3.2 \times 10^{-4})$ |
| | q1 | $3.2 \pm (6.7 \times 10^{-4})$ |
| | q2 | $4.3 \pm (6.0 \times 10^{-4})$ |
| | q3 | $5.7 \pm (5.1 \times 10^{-4})$ |
| $B^+ \to K^0_s\pi^+\mu^+\mu^-$ | q0 | $3.6 \pm (4.9 \times 10^{-4})$ |
| | q1 | $6.1 \pm (1.0 \times 10^{-4})$ |
| | q2 | $6.0 \pm (7.3 \times 10^{-4})$ |
| | q3 | $8.4 \pm (7.1 \times 10^{-4})$ |
| $B^0 \to K^+\pi^-\mu^+\mu^-$ | q0 | $4.5 \pm (5.6 \times 10^{-4})$ |
| | q1 | $6.6 \pm (1.0 \times 10^{-3})$ |
| | q2 | $9.4 \pm (9.5 \times 10^{-4})$ |
| | q3 | $9.5 \pm (8.1 \times 10^{-4})$ |
| $B^+ \to K^+\pi^0e^+e^-$ | q0 | $5.3 \pm (6.6 \times 10^{-4})$ |
| | q1 | $7.0 \pm (1.2 \times 10^{-3})$ |
| | q2 | $6.5 \pm (8.4 \times 10^{-4})$ |
| | q3 | $12.4 \pm (8.6 \times 10^{-4})$ |
| $B^+ \to K^0_s\pi^+e^+e^-$ | q0 | $11.2 \pm (8.5 \times 10^{-4})$ |
| | q1 | $8.5 \pm (1.2 \times 10^{-3})$ |
| | q2 | $7.7 \pm (8.7 \times 10^{-4})$ |
| | q3 | $10.6 \pm (8.5 \times 10^{-4})$ |
| $B^0 \to K^+\pi^-e^+e^-$ | q0 | $8.7 \pm (9.5 \times 10^{-4})$ |
| | q1 | $10.0 \pm (1.5 \times 10^{-3})$ |
| | q2 | $10.9 \pm (1.2 \times 10^{-3})$ |
| | q3 | $12.6 \pm (1.1 \times 10^{-3})$ |

Table 3.4: Final reconstruction efficiency for signal events by mode and $q^2$ bin.

| Mode | $q^2$ bin | Signal Events | Background | Fit Region |
|---|---|---|---|---|
| $B^+ \to K^+\mu^+\mu^-$ | q0 | 1.7 | 0.3 | 6.0 |
| | q1 | 4.0 | 0.7 | 33.0 |
| | q2 | 2.6 | 0.7 | 19.2 |
| | q3 | 4.3 | 2.1 | 32.3 |
| $B^+ \to K^+e^+e^-$ | q0 | 6.4 | 2.2 | 42.1 |
| | q1 | 6.3 | 0.3 | 44.2 |
| | q2 | 3.5 | 0.3 | 48.0 |
| | q3 | 5.0 | 0.0 | 15.5 |
| $B^+ \to K^+\pi^0\mu^+\mu^-$ | q0 | 0.4 | 1.4 | 9.8 |
| | q1 | 0.6 | 1.0 | 9.2 |
| | q2 | 0.7 | 0.3 | 17.2 |
| | q3 | 1.2 | 5.0 | 28.9 |
| $B^+ \to K^0_s\pi^+\mu^+\mu^-$ | q0 | 0.6 | 0.0 | 7.2 |
| | q1 | 0.8 | 0.3 | 9.0 |
| | q2 | 0.7 | 0.3 | 5.6 |
| | q3 | 1.2 | 1.0 | 26.6 |
| $B^0 \to K^+\pi^-\mu^+\mu^-$ | q0 | 2.1 | 0.8 | 17.7 |
| | q1 | 2.7 | 1.0 | 16.8 |
| | q2 | 3.0 | 2.8 | 52.5 |
| | q3 | 3.9 | 2.2 | 33.4 |
| $B^+ \to K^+\pi^0e^+e^-$ | q0 | 1.3 | 1.4 | 9.2 |
| | q1 | 1.4 | 1.8 | 26.6 |
| | q2 | 1.0 | 1.0 | 16.1 |
| | q3 | 2.3 | 2.2 | 50.5 |
| $B^+ \to K^0_s\pi^+e^+e^-$ | q0 | 1.8 | 0.3 | 21.2 |
| | q1 | 1.1 | 0.7 | 5.5 |
| | q2 | 0.8 | 0.3 | 8.1 |
| | q3 | 1.3 | 1.0 | 5.6 |
| $B^0 \to K^+\pi^-e^+e^-$ | q0 | 2.8 | 2.6 | 17.2 |
| | q1 | 2.7 | 0.7 | 13.7 |
| | q2 | 2.2 | 1.4 | 23.1 |
| | q3 | 3.1 | 1.0 | 17.6 |

Table 3.5: Expected signal and combinatorial background yields in signal region $5.27 < m_{\mathrm{ES}} < 5.29$ GeV/$c^2$ and in the fit region $5.2 < m_{\mathrm{ES}} < 5.29$ GeV/$c^2$ in each mode and each $q^2$ bin. The error on these yields is negligible.

| Mode | $q^2$ bin | Signal Events | Background | Fit Region |
|---|---|---|---|---|
| $B^+ \to K^+ l^+ l^-$ | q0 | 8.1 | 2.5 | 48.1 |
| | q1 | 10.3 | 1.0 | 77.2 |
| | q2 | 6.1 | 1.0 | 67.2 |
| | q3 | 9.4 | 2.1 | 47.8 |
| $B \to K^* l^+ l^-$ | q0 | 8.9 | 6.5 | 82.3 |
| | q1 | 9.4 | 5.6 | 80.9 |
| | q2 | 8.4 | 6.2 | 122.7 |
| | q3 | 13.0 | 12.4 | 162.6 |

Table 3.6: Expected concatenated signal and combinatorial background yields in the signal region $5.27 < m_{\mathrm{ES}} < 5.29$ GeV/$c^2$, and the fit region 5.2 GeV/$c^2 < m_{\mathrm{ES}}$. The error on these yields is negligible.

## 3.10 Run 6 Event Selection

After the Run 5 analysis, the *BABAR* dataset increased by a factor of 1.2 and the up-grades to the IFR discussed in Section 2.7 improved the muon identification significantly. Since this analysis is statistics limited any increase to $S/\sqrt{S+B}$ is beneficial. Therefore, it was necessary to re-optimise the event selection. The optimisation was carried out in the low and high $q^2$ bins. It is hoped that the increase in statistics and efficiency will ensure that the Run 6 measurement will be made in four $q^2$ bins.

Only four of the previous six decay modes are measured in the Run 6 analysis:

- $B^+ \to K^{*+} l^+ l^-$ where $K^{*+} \to K^0_S \pi^+$ and $K^0_S \to \pi^+ \pi^-$
- $B^0 \to K^{*0} l^+ l^-$ where $K^{*0} \to K^+ \pi^-$

The modes $B^+ \to K^{*+} l^+ l^-$ where $K^{*+} \to K^+ \pi^0 (\to \gamma\gamma)$ is no longer used because it does not significantly improve the signal significance.

For each particle several different multi-variate techniques were investigated to find which one provided the highest efficiency. The particle identification for the pions is the same as described in Section 3.3. For the muons, kaons and

| Mode | $q^2$ bin | Reconstruction Efficiency (%) |
|---|---|---|
| $B^+ \to K_s^0\pi^+\mu^+\mu^-$ | low | 9.7 $\pm(7.6 \times 10^{-4})$ |
| | high | 8.6 $\pm(7.4 \times 10^{-4})$ |
| $B^0 \to K^+\pi^-\mu^+\mu^-$ | low | 11.9 $\pm(4.9 \times 10^{-4})$ |
| | high | 13.9 $\pm(5.1 \times 10^{-4})$ |
| $B^+ \to K_s^0\pi^+e^+e^-$ | low | 12.1 $\pm(8.3 \times 10^{-4})$ |
| | high | 9.7 $\pm(9.0 \times 10^{-4})$ |
| $B^0 \to K^+\pi^-e^+e^-$ | low | 14.9 $\pm(5.4 \times 10^{-4})$ |
| | high | 16.0 $\pm(6.1 \times 10^{-4})$ |

Table 3.7: Final reconstruction efficiency for signal events by mode and $q^2$ bin.

electrons the selection has changed, in particular the muon identification has improved significantly, therefore allowing a lower momentum on the muons to be applied.

There are two differences to the kinematic selection. The lower muon momentum cut is now $p_{LAB} \geq 0.3$ GeV/$c$ compared to $p_{LAB} \geq 0.7$ GeV/$c$ in the previous analysis and the $\Delta E$ window in the $m_{ES}$ sideband region now extends to $-0.1 < \Delta E < 0.1$ GeV where previously it was $-0.08 < \Delta E < 0.05$ GeV.

The combinatoric background from continuum $uds$ and $c\bar{c}$, and $B\overline{B}$ events are suppressed using boosted decision trees (BDTs) [80]. The BDT is an alternative method to the neural network that is used to separate the signal and the combinatoric background. All of the same kinematic input variables are used with the addition of the variable $\Delta E$. The BDTs are trained in two regions of di-lepton mass, for each lepton flavour, and for both continuum and $B\overline{B}$ backgrounds. The performance from the BDTs was found to provide a slightly better performance compared to neural networks.

The lower cut on the di-lepton mass for the $J/\Psi$ veto has been moved to $m_{ll} >$ 2.83 GeV/$c^2$ from $m_{ll} >$ 2.90 (3.00) GeV/$c^2$ for the electron (muon) modes. The other veto regions remained the same as in Section 3.6.2.

The efficiency is calculated for each mode and for both the high and low $q^2$ regions. The efficiencies are shown in Table 3.7.

| | Signal | | Background | | | |
|---|---|---|---|---|---|---|
| | $m_{ES} > 5.27$ | | $m_{ES} > 5.27$ | | $m_{ES} > 5.2$ | |
| Mode | low | high | low | high | low | high |
| $B^+ \to K^+\pi^0\mu^+\mu^-$ | $5 \pm 1$ | $6 \pm 1$ | $60 \pm 8$ | $25 \pm 4$ | $419 \pm 65$ | $167 \pm 21$ |
| $B^+ \to K^0_s\pi^+\mu^+\mu^-$ | $5 \pm 1$ | $4 \pm 1$ | $20 \pm 4$ | $9 \pm 2$ | $135 \pm 26$ | $58 \pm 11$ |
| $B^0 \to K^+\pi^-\mu^+\mu^-$ | $15 \pm 3$ | $18 \pm 3$ | $40 \pm 4$ | $30 \pm 3$ | $270 \pm 30$ | $199 \pm 22$ |
| $B^+ \to K^+\pi^0e^+e^-$ | $5 \pm 1$ | $4 \pm 1$ | $5 \pm 1$ | $5 \pm 1$ | $34 \pm 6$ | $21 \pm 4$ |
| $B^+ \to K^0_s\pi^+e^+e^-$ | $6 \pm 1$ | $4 \pm 1$ | $5 \pm 1$ | $3 \pm 1$ | $30 \pm 4$ | $21 \pm 3$ |
| $B^0 \to K^+\pi^-e^+e^-$ | $19 \pm 3$ | $19 \pm 3$ | $7 \pm 1$ | $10 \pm 11$ | $49 \pm 5$ | $70 \pm 8$ |
| All $K^*ll$ | $55 \pm 9$ | $55 \pm 9$ | $137 \pm 19$ | $82 \pm 11$ | $937 \pm 121$ | $549 \pm 71$ |

Table 3.8: Expected signal and combinatorial background yields in signal region $5.27 < m_{\mathrm{ES}} < 5.29$ GeV/$c^2$ and in the fit region $5.2 < m_{\mathrm{ES}} < 5.29$ GeV/$c^2$ in each mode and each $q^2$ bin.

The number of signal and background events is calculated using all of the above information and scaled to the number of $B \to K^*l^+l^-$ events produced by 468 million $B\overline{B}$ pairs, this is shown in Table 3.8.

From Table 3.8, it can be seen that the $B^+ \to K^{*+}l^+l^-$ where $K^{*+} \to K^+\pi^0(\to \gamma\gamma)$ modes have the smallest value of $S/\sqrt{S+B}$. These modes have the largest number of background events from combinatoric events and peaking charmonium. It was decided that these modes should be removed. The predicted number of signal events is 65 if these modes are included and 50 when they are excluded. It is hoped that the reduction in the number of background events will be enough to achieve a successful measurement in all four $q^2$ bins.

## 3.11 Conclusion

This chapter detailed the final event selection for the Run 5 and Run 6 analyses. The Run 5 dataset is 384 million $B\overline{B}$ pairs and the event selection was optimised for this dataset. For the Run 6 analysis the dataset had increased to 468 million $B\overline{B}$ pairs, ~1.22 larger than the Run 5 dataset. In addition, there were improvements make to the detector, described in Section 2.7, that greatly enhanced its performance. The event selection was re-optimised for the Run 6 analysis to account for these changes.

# 4

# Fitting Technique

From Section 1.3.2, the angles of interest in the helicity frame are: $\theta_{K^*}$, the kaon angle relative to the $B$ in the $K^*$ rest frame; and $\theta_l$, the $l^+$ angle relative to the $B$ in the di-lepton rest frame, as shown in Figure 1.5. By fitting the distributions of these angles the following can be measured: the fraction of $K^*$ longitudinal polarisation, $F_L$, and the forward-backward asymmetry, $A_{FB}$. In Section 1.3.2 two different methods to extract $F_L$ and $A_{FB}$ were described. The first strategy involved two one-dimensional angular distributions for $\cos\theta_K$ and $\cos\theta_l$, the second used one two-dimensional angular distribution in $(\cos\theta_K, \cos\theta_l)$. For the Run 5 analysis $F_L$ and $A_{FB}$ were measured using only the first strategy. For the Run 6 analysis both techniques are used. This chapter will show the signal, background and efficiency fit components for the Run 6 analysis, however the Run 5 analysis is analogous. Any difference between the fitting strategies for the two analyses will be highlighted in the relevant section.

There are four extended maximum likelihood fits that are performed in each bin of $q^2$:

- Fit One - a one-dimensional fit to $m_{ES}$, to extract the signal and background yields.
- Fit Two - $\cos\theta_{K^*}$ is added as an extra dimension to Fit One, to extract $F_L$. This a one-dimensional fit, all of the parameters determined from Fit One are fixed.

- Fit Three - $\cos\theta_l$ is added as an extra dimension to Fit Two, to extract $A_{FB}$. This a one-dimensional fit, all of the parameters determined from Fit One and Two are fixed.
- Fit Four - $(\cos\theta_{K^*}, \cos\theta_l)$ are added as extra dimensions to Fit One, to extract $F_L$ and $A_{FB}$. This is a two-dimensional fit, all parameters determined from Fit One are fixed.

Fits Two and Three use one-dimensional angular distributions for $\cos\theta_{K^*}$ and $\cos\theta_l$, this first strategy of extracting $F_L$ and $A_{FB}$ will be referred to as the "1D fits". Fit Four uses the two-dimensional angular distribution for $(\cos\theta_{K^*}, \cos\theta_l)$, the second strategy will be referred to as the "2D fit". In this section the construction of the probability density functions (PDF) for the signal and background components are discussed.

The extended maximum likelihood function for the fit to $B \to K^* l^+ l^-$ data is:

$$\mathcal{L} = \exp\left(-\sum_{i=1}^{N_{hyp}} n_i\right)\left[\prod_{j=1}^{N_k}\left(\sum_{i=1}^{N_{hyp}} n_i \mathcal{P}(\bar{x}_j;\bar{\alpha}_i)\right)\right] \tag{4.0.1}$$

where $N_{hyp}$ is the number of event hypotheses, $n_i$ is the yield of each hypothesis, and $N_k$ is the number of candidate events observed in data. The correlations between the observables $(m_{ES}, \cos\theta_{K^*}, \cos\theta_l)$ are small. The PDF $\mathcal{P}(\bar{x}_j;\bar{\alpha}_i)$ for the $i$th event hypothesis is defined as the product of individual PDFs for each fit observable $x_j$ given the set of parameters $\bar{\alpha}_i$. The type of event can be categorised into: signal, combinatoric background, peaking background and mis-reconstructed signal decays. The remainder of this chapter describes the PDFs that are used to model these signal and background shapes used in the fit. The floating parameters in the fit are optimised by minimising the log of the likelihood function $-\log(\mathcal{L})$.

## 4.1 Signal PDFs

In Fit One the signal yield is found by performing a fit in the variable $m_{ES}$. The $m_{ES}$ signal distribution is parameterized by a Gaussian with the mean and width fixed to values from fits to the charmonium control sample, described in Section 5.1.

In the 1D fits to extract $F_L$ and $A_{FB}$ the angular distributions for $\cos\theta_{K^*}$ and $\cos\theta_l$ are added in turn as extra dimensions to Fit One to create Fit Two.

In Section 1.3.2 the signal shape in $\cos\theta_{K^*}$ is shown in Equation 1.3.6, $\cos\theta_l$ is shown in Equation 1.3.7 and $(\cos\theta_{K^*}, \cos\theta_l)$ is defined in Equation 1.3.8.

The PDF given by Equation 1.3.8 can be fitted to the signal MC in order to find the values of $F_L$ and $A_{FB}$ that are input at the generator level. Figure 4.1 gives the 1D projections of these fits. There is a slight problem the fit to $\cos\theta_l$ at $\cos\theta_l = \pm 1$, this is due to the generator incorrectly modelling the physical distribution.

For the $B \to K l^+ l^-$ modes the angular distribution for $\cos\theta_l$ can be written as:

$$\frac{1}{\Gamma}\frac{d\Gamma}{d\cos\theta_l} = \frac{3}{4}(1-F_S)(1-\cos^2\theta_l) + \frac{1}{2}F_S + A_{FB}\cos\theta_l$$

where $F_S$ is a possible new physics scalar contribution that is small even in the presence of new physics and is therefore set to zero. $A_{FB}$ for $B \to K l^+ l^-$ is zero. Therefore, the distribution simplifies to:

$$\frac{1}{\Gamma}\frac{d\Gamma}{d\cos\theta_l} = \frac{3}{4}(1-\cos^2\theta_l) + A_{FB}\cos\theta_l. \tag{4.1.1}$$

## 4.2 Efficiency correction

The angular distributions above do not account for any acceptance effects due to the performance of the detector. To compensate for this an efficiency correction is applied to the selected event sample. The efficiency correction was found by studying $B \to K^* l^+ l^-$ signal MC events. Each event was traced back to its generation to find whether the event had been correctly reconstructed. For the 1D fits two 1D histogram PDFs were produced, representing the efficiency as a function of $\cos\theta_{K^*}$, and $\cos\theta_l$ for each mode. For the 2D fit a 2D histogram PDF was produced, representing the efficiency as a function of

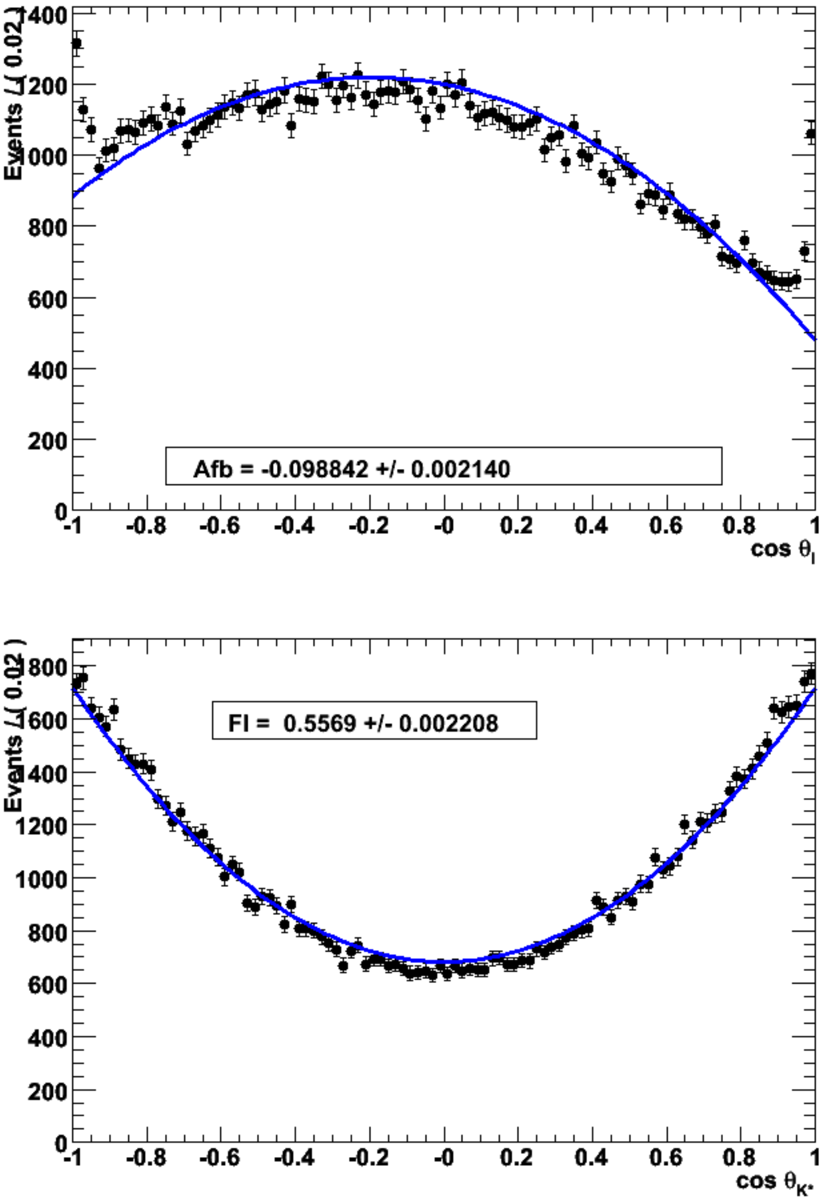

Figure 4.1: Fits to generated $B^0 \to K^+\pi^-e^+e^-$ signal MC for the $q^2$ bin, $q0$. Top: Fit to $\cos\theta_{K^*}$, Bottom: Fit to $\cos\theta_l$.

$(\cos\theta_{K^*}, \cos\theta_l)$ for each mode.

The efficiency was found to be fairly constant over most of the range but falls off rapidly at the limits, $\cos\theta = \pm 1$. It also varies across the modes, with the $K^{*+} \to K^+\pi^0$ mode displaying the lowest efficiency. At low $\cos\theta_{K^*}$ this is due to the low reconstruction efficiency of the low energy $\pi^0$ and at high $\cos\theta_{K^*}$ is due to the loss of low momentum $K^+$. There is a difference in efficiency between the electron and muon modes due to the different selection efficiencies, Section 3.10. Figures 4.2 and 4.3 show the 1D projections of the combined $B \to K^* l^+ l^-$ signal efficiency in each of the $q^2$ bins for the $\cos\theta_{K^*}$ and $\cos\theta_l$ distributions, respectively. Figures 8.9 and 8.10 in the Appendix show the $\cos\theta_{K^*}$ and $\cos\theta_l$ efficiency distributions for each of the four signal modes in $q0$.

For the 1D fits the signal PDFs are defined as the product of the efficiency histogram PDF with the angular distribution. An example of this using $\cos\theta_{K^*}$ is:

$$P(\cos\theta_K) = \epsilon(\cos\theta_K) \times \frac{1}{\Gamma}\frac{d\Gamma}{d\cos\theta_K} \tag{4.2.1}$$

where $\epsilon(\cos\theta_K)$ is the efficiency PDF.

The 2D fit is a more complicated fit and accounting for variation in efficiency was much more difficult. There were four different strategies to correct for the efficiency that were explored, they will be discussed in depth in Section 5.2. The chosen method was that for each event in the dataset, the corresponding value of the efficiency was found from the 2D efficiency histogram, the event was then weighted by $((Average\ \epsilon)/\epsilon)$ and fit with the 2D angular distribution of the signal without the efficiency folded in.

## 4.3 Combinatoric Background

Combinatoric backgrounds originate from either $e^+e^- \to B\overline{B}$ events where the $B$ meson decays in such a way as to mimic the $B \to K^* l^+ l^-$ event, or from continuum events where a light $(u, d, s, c)$ quark pair is formed.

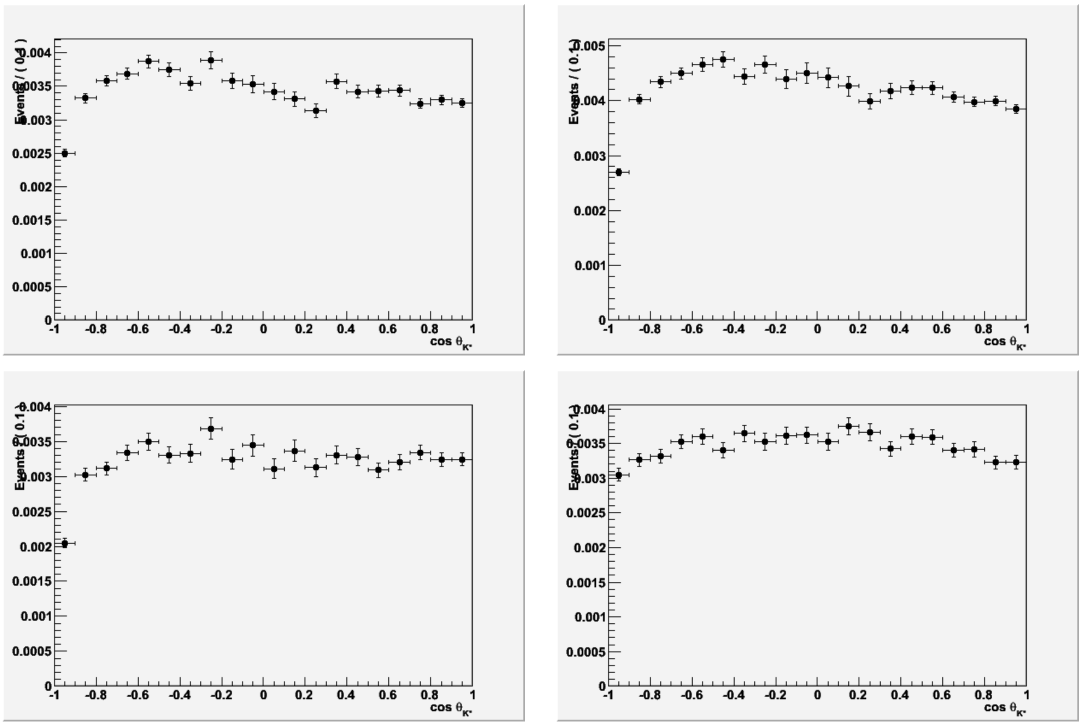

Figure 4.2: One dimensional projection of the combined $B \rightarrow K^*l^+l^-$ efficiency for $\cos\theta_{K^*}$. Top: $q0$ left, $q1$ right. Bottom: $q2$ left, $q3$ right.

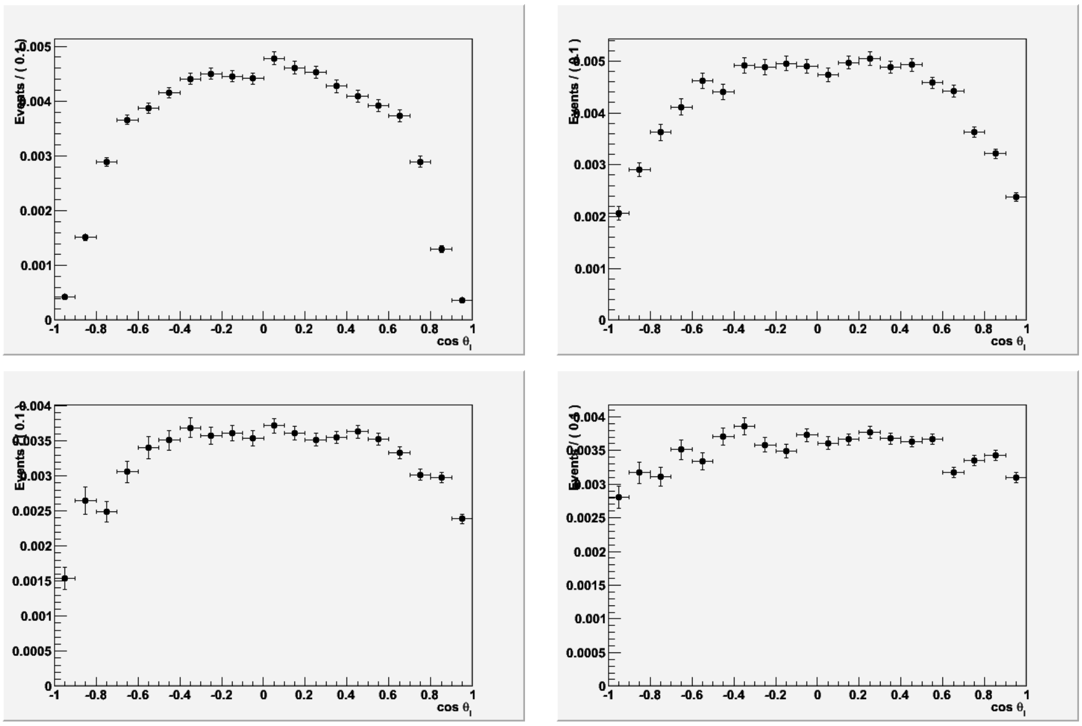

Figure 4.3: One dimensional projection of the combined $B \to K^*l^+l^-$ efficiency for $\cos\theta_l$. Top: $q0$ left, $q1$ right. Bottom: $q2$ left, $q3$ right.

The primary source of combinatoric background is from $B\overline{B}$ where both $B$-mesons decay semi-leptonically. Another source of combinatoric background comes from $B \to D^{(*)}l\nu$ events where the $D$ meson decays semi-leptonically, $D \to K^{*}l\nu$. Lastly, there are combinatoric events where one of the hadrons is misidentified as a lepton.

The combinatoric background distribution in $m_{ES}$ is modelled by an Argus function [82]:

$$f(m_{ES}) \propto e^{-\xi\left(1-\frac{m_{ES}^2}{E_B^2}\right)}$$

where $\xi$ is a free parameter determined in the fit to data.

The lepton-flavour violating control samples, where the dilepton pair are either $e^{+}\mu^{-}$ or $\mu^{+}e^{-}$, provides an excellent way to study semileptonic $B$ backgrounds. The distribution of the combinatoric background is modelled using both the lepton-flavour violating and lepton-flavour conserving data from the sideband region in $m_{ES}$, defined by $5.2 < m_{ES} < 5.27$ GeV. For the 1D fits two 1D histogram PDFs were generated to model the $\cos\theta_K$ and $\cos\theta_l$ distribution. For the 2D fits a 2D histogram PDF was produced to model the $(\cos\theta_K, \cos\theta_l)$ angular distributions of the combinatoric background. Figures 4.4 and 4.5 show the 1D projections of the combined $B \to K^{*}l^{+}l^{-}$ combinatoric background in each of the $q^2$ bins for the $\cos\theta_{K^*}$ and $\cos\theta_l$ distributions, respectively. Figures 8.11 and 8.12 in the Appendix show the $\cos\theta_{K^*}$ and $\cos\theta_l$ combinatoric background distributions for each of the four signal modes in $q0$. For both analyses, the PDFs for the background are simultaneously fitted in the $m_{ES}$ sideband and signal region. The sideband in data can be compared with the fit and sideband region in MC samples to ensure that the sideband correctly models the fit region in data.

## 4.4 Crossfeed Components

The crossfeed components for the Run 5 and Run 6 analysis are modelled in a slightly different way. Sections 4.4.1 and 4.4.2 describe how the crossfeed is

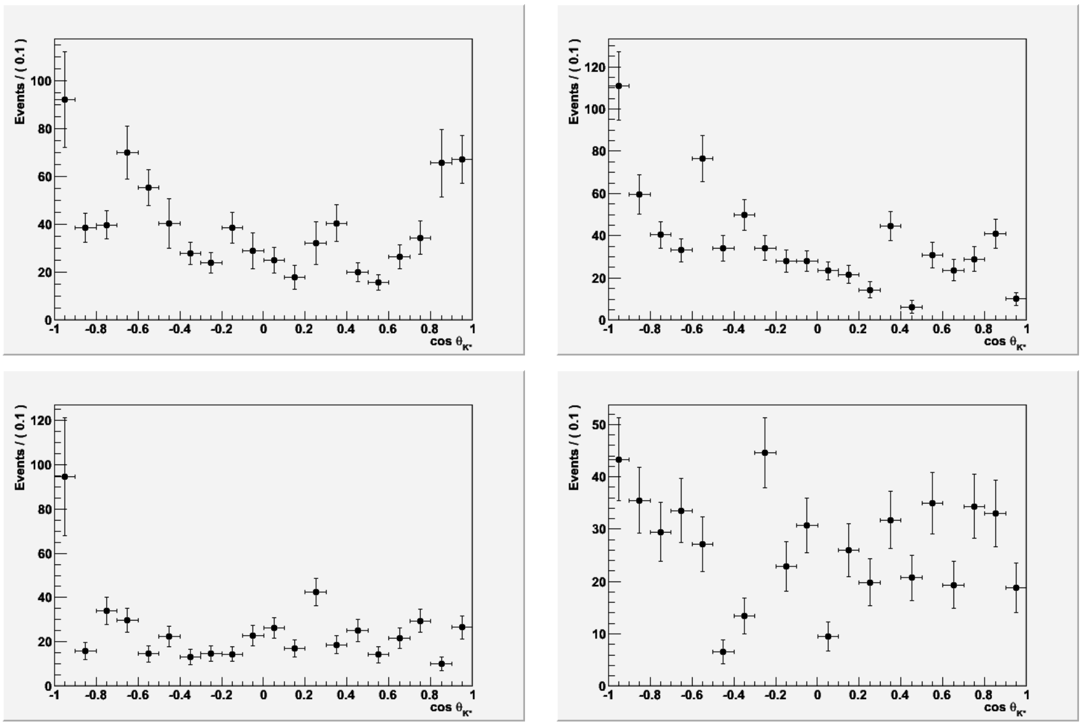

Figure 4.4: One dimensional projection of the combined $B \rightarrow K^{*}l^{+}l^{-}$ combinatoric background for $\cos\theta_{K^{*}}$. Top: $q0$ left, $q1$ right. Bottom: $q2$ left, $q3$ right.

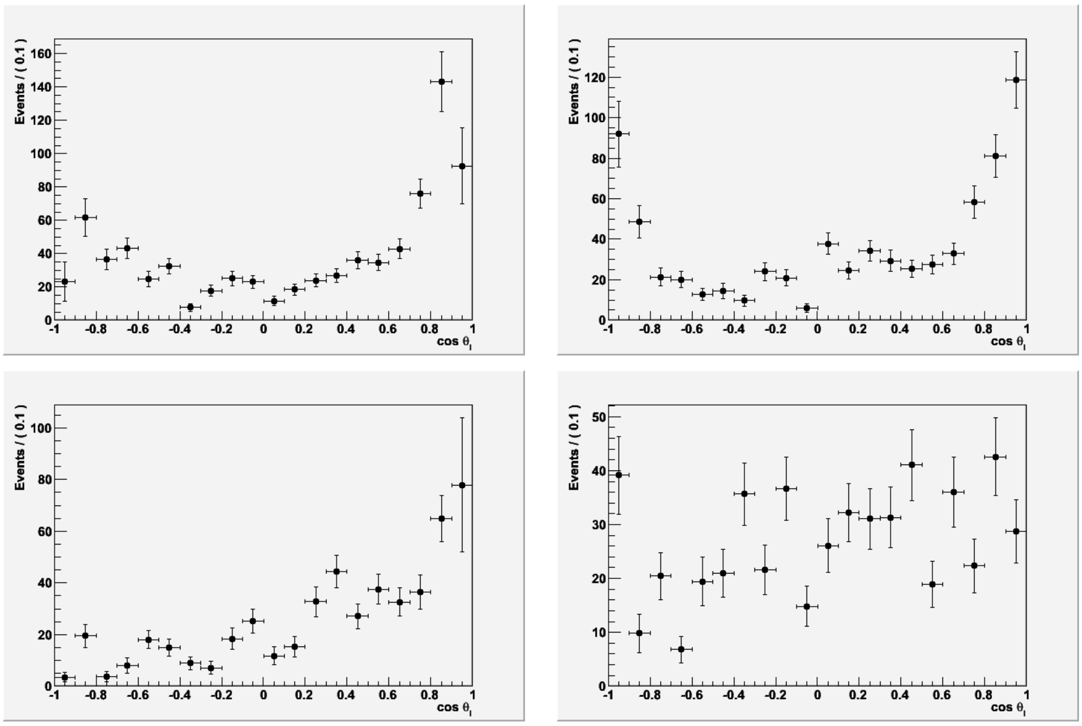

Figure 4.5: One dimensional projection of the combined $B \rightarrow K^{*} l^{+} l^{-}$ combinatoric background for $\cos\theta_l$. Top: $q0$ left, $q1$ right. Bottom: $q2$ left, $q3$ right.

treated in the Run 5 analysis and Section 4.4.3 describes the Run 6 analysis.

### 4.4.1 Feed-across between Different Modes

Feed-across events occur when a true signal decay is reconstructed as a different signal decay used in this analysis. This can occur when the correct $\pi^0$ is swapped with a random $\pi^+$ when reconstructing the decay. These events are background events between different $B \to K^* l^+ l^-$ modes. Signal MC is used to model the feed-across background for each mode in the different bins of $q^2$. The swapped-in pion results in the $m_{ES}$ distribution being broadened since the pion that was swapped in will have a different momentum to the true pion.

The feed-across distribution for $m_{ES}$ is modelled using a Crystal Ball function. Since the feed-across has a tail in $m_{ES}$, a Gaussian would not adequately describe the distribution. The Crystal Ball is composed of a Gaussian core with a power law tail [83]:

$$f(x) \propto \begin{cases} exp(-\frac{(x-\overline{x})^2}{2\sigma^2}) & : \ (x-\overline{x})/\sigma > \alpha \\ A \times \left(B - \frac{x-\overline{x}}{\sigma}\right)^{-n} & : \ (x-\overline{x})/\sigma < \alpha \end{cases}$$

where $A = (n/|\alpha|)^n \times exp(-|\alpha|^2/2)$ and $B = n/|\alpha| - |\alpha|$. $\overline{x}$ and $\sigma$ are the mean and width of the Gaussian. This PDF is added as a separate component of the fit with all parameters fixed from signal MC studies.

Although the feed-across is small, it is accounted for in the all of the fits. However, it is not modelled in the $m_{ES}$ sidebands. Therefore, it is not accounted for in the combinatoric background PDF.

### 4.4.2 Self-crossfeed

Self-crossfeed occurs when a signal $K^* l^+ l^-$ event is reconstructed in the correct final state, however, a wrong final state particle has been used. This type of crossfeed can be significant, in particular where $K^{*+} \to K^+ \pi^0$. The $\pi^0$ in these

| Mode | $q0$ bin | $q1$ bin | $q2$ bin | $q3$ bin |
|---|---|---|---|---|
| $B^+ \to K_s^0\pi^+\mu^+\mu^-$ | 0.8 | 0.32 | 1.89 | 1.68 |
| $B^0 \to K^+\pi^-\mu^+\mu^-$ | 0.35 | 0.14 | 0.87 | 0.99 |
| $B^+ \to K_s^0\pi^+e^+e^-$ | 0.64 | 0.22 | 1.00 | 0.96 |
| $B^0 \to K^+\pi^-e^+e^-$ | 0.30 | 0.10 | 0.49 | 0.61 |
| TOTAL | 2.09 | 0.78 | 4.25 | 4.24 |

Table 4.1: Number of expected inclusive crossfeed events by mode and $q^2$ bin.

events can often be reconstructed using a wrong photon.

The self-crossfeed is also modelled using a Crystal Ball function in $m_{ES}$ but since it is a signal event that is reconstructed with slightly the wrong energy and momentum it has to be treated differently from the feed-across. The $m_{ES}$ signal Gaussian and the Crystal Ball self-crossfeed shape are summed together. The signal to self-crossfeed fraction is fixed from signal MC.

### 4.4.3 Inclusive Crossfeed

For the Run 6 analysis the feed-across and self-crossfeed are summed together to make an inclusive crossfeed. The self-crossfeed is not added as a component of the $m_{ES}$ fit, instead a systematic is assigned to this in Section 7.2. For the angular fits the crossfeed component is modelled in the same way as before using signal MC samples. This component is then added as a fixed PDF in the final fit, the number of events are shown in Table 4.1. Figures 4.7 and 4.7 show the combined $B \to K^*l^+l^-$ for the inclusive crossfeed background for the $\cos\theta_{K^*}$ and $\cos\theta_l$ distributions, respectively. Figures 8.13 and 8.14 in the Appendix show the inclusive crossfeed background for $q0$ in each of the four signal modes.

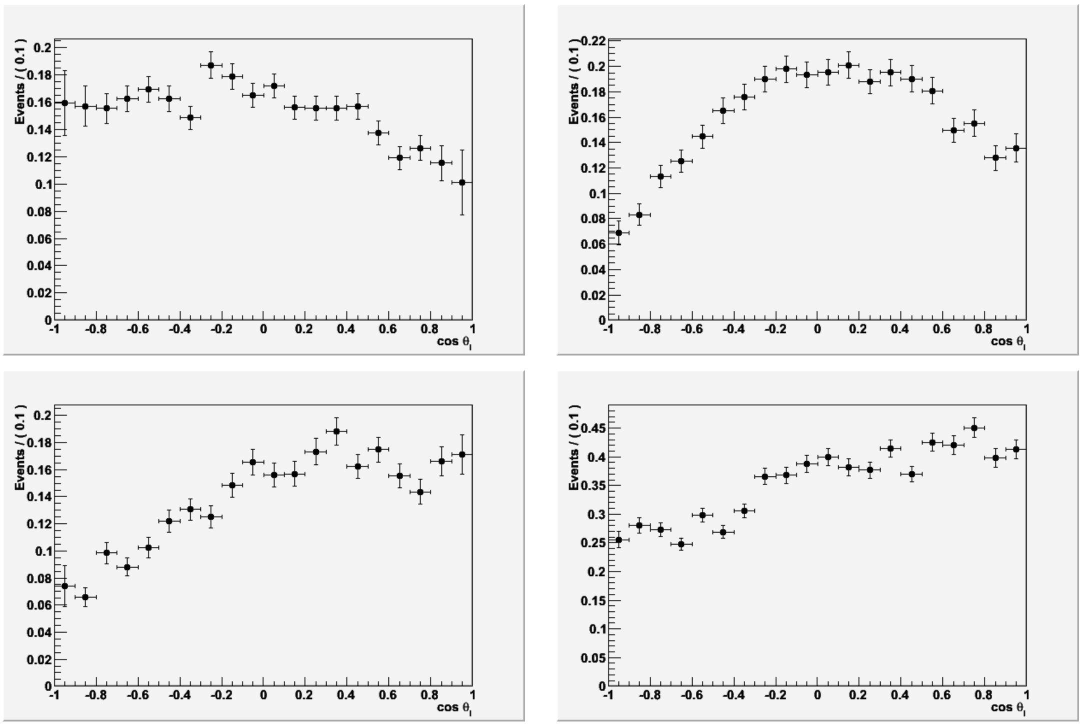

Figure 4.6: One dimensional projection of the combined $B \rightarrow K^{*}l^{+}l^{-}$ inclusive crossfeed background for $\cos\theta_l$. Top: $q0$ left, $q1$ right. Bottom: $q2$ left, $q3$ right.

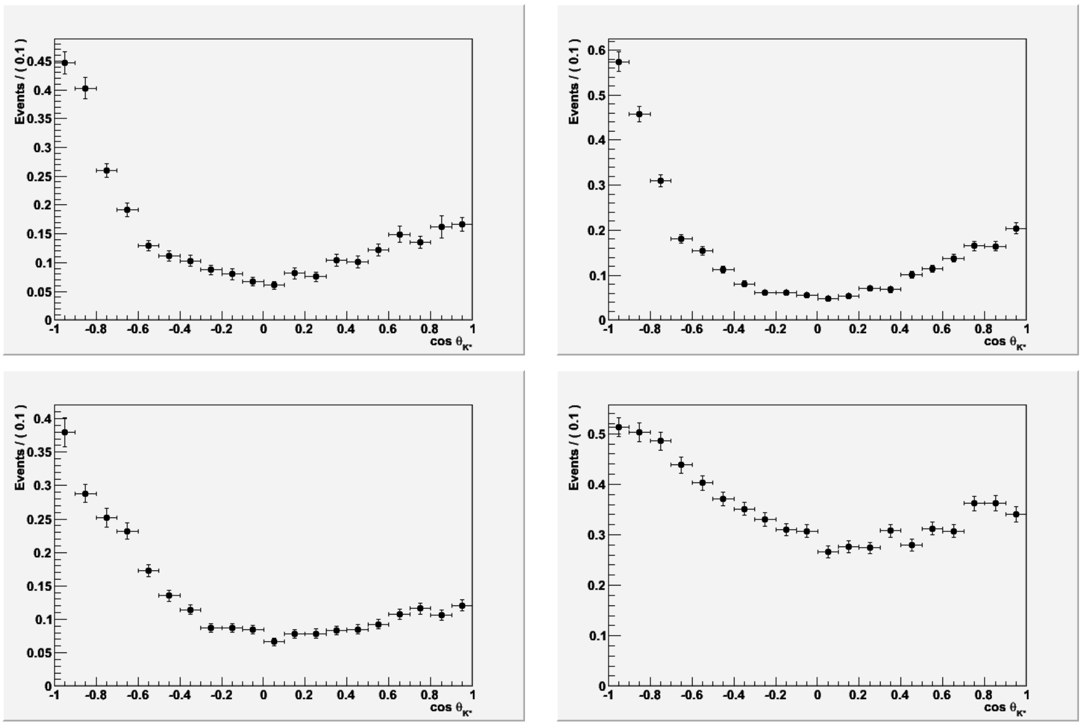

Figure 4.7: One dimensional projection of the combined $B \rightarrow K^*l^+l^-$ inclusive crossfeed background for $\cos\theta_{K^*}$. Top: $q0$ left, $q1$ right. Bottom: $q2$ left, $q3$ right.

## 4.5 Hadronic Peaking Background

There are a few sources of hadronic background that remain after all the event selections and vetoes, discussed in Sections 3.10 and 3.6.3, have been applied. An example is the three-body decay $B \rightarrow K^{*}h^{+}h^{-}$, where the "$h$" can be a charged pion or kaon. If the two "$h$" are misidentified as muons it produces a background with a peaking distribution in the signal region. Predominantly the two "h" are pions and this background is mainly in the muon mode. In order to estimate these backgrounds a control sample is used.

The control sample contains events reconstructed as $B \rightarrow K^{*}\mu h$, where the "$h$" is a kaon or pion, as above. The muon must pass the muon selection and the $h$ must fail the electron or muon selection. The result is a sample which is composed of hadronic B decays with one misidentified muon. This sample must then pass all of the kinematic selection criteria. The probability for the remaining hadron, $h$ to also be mis-identified as a muon is used to weight the sample.

The $m_{ES}$ distribution of this sample is then fitted with an Argus and a Gaussian for the flat and peaking components, respectively. Only the peaking component is added to the final $m_{ES}$ and angular fits as the flat component is already modelled in the combinatoric background. For the 2D fit a 2D binned histogram PDF was used to model the $(\cos\theta_K, \cos\theta_l)$ angular distributions and for the 1D fits 1D binned histogram PDFs were used for $\cos\theta_K$ and $\cos\theta_l$. This technique is carried out in each of the $q^2$ bins in the $m_{ES}$ signal region. The total number of hadronic peaking background events for each mode and $q^2$ bin are shown in Table 4.2.

Another peaking background is from charmonium events that escape the veto region in $\Delta E$ and $m_{ll}$, Section 3.10. To model this background the $K^{(*)}ll$ selections are applied to the charmonium MC and the number of events that remain are determined. These events are then fit using the technique described in Section 5.1 and scaled to the number expected in data. The number of expected events for each mode and $q^2$ are shown in Table 4.3.

There is also a small peaking background component at low $q^2$ from $B \rightarrow K^{*}\pi^{0}/\eta$, where the $\pi^0$ or $\eta$ decay to a photon and a lepton pair. These events are studied using exclusive MC samples. The shape of the background is found and a normalisation is applied.

## 4.6 Fitting Strategy

### 4.6.1 Fit One - $m_{ES}$ Fit

The candidates for the four $K^{*}l^{+}l^{-}$ modes are summed in both the signal and sideband region to give a combined $m_{ES}$ distribution for each $q^2$ bin.

Fitted parameters:

- The number of signal events, $N_S(q^2)$.
- The number of combinatoric background events, $N_B(q^2)$.
- The combinatoric background Argus parameter shape, $\xi(q^2)$.

Fixed parameters:

- The endpoint of the combinatoric background at $m_{ES} = 5.29$ GeV.
- The ratio of the self-crossfeed to the signal yield.
- The shape of the feed-across and self-crossfeed contributions.
- The mean and sigma of the Gaussian signal.

### 4.6.2 Fit Two - 1D Fit to extract $F_L$

$\cos\theta_{K^*}$ is an additional fit variable to Fit 1 in each $q^2$ bin.

Fitted parameters:

- The $K^*$ polarisation of the signal, $F_L$.

Fixed parameters:

- All fixed and floated parameters from Fit 1.
- The $\cos\theta_{K^*}$ shape of the combinatoric background.
- The $\cos\theta_{K^*}$ efficiency of the signal.
- The $\cos\theta_{K^*}$ shape of the crossfeed contributions.
- The $\cos\theta_{K^*}$ shape of the peaking background.

### 4.6.3 Fit Three - 1D Fit to extract $A_{FB}$

$\cos\theta_l$ is an additional fit variable to Fit 2 in each $q^2$ bin.

Fitted parameters:

- The forward-backward asymmetry of the signal, $A_{FB}$.

Fixed parameters:

- All fixed and floated parameters from Fit 2.
- The $\cos\theta_l$ shape of the combinatoric background.
- The $\cos\theta_l$ efficiency of the signal.
- The $\cos\theta_l$ shape of the crossfeed contributions.
- The $\cos\theta_l$ shape of the peaking background.

### 4.6.4 Fit Four - 2D Fit to extract $F_L$ and $A_{FB}$

$(\cos\theta_{K^*}, \cos\theta_l)$ are additional fit variables to Fit 1 in each $q^2$ bin.

Fitted parameters:

- The $K^*$ polarisation of the signal, $F_L$.
- The forward-backward asymmetry of the signal, $A_{FB}$.

Fixed parameters:

- All fixed and floated parameters from Fit 1.
- The $(\cos\theta_{K^*}, \cos\theta_l)$ shape of the combinatoric background.
- The $(\cos\theta_{K^*}, \cos\theta_l)$ efficiency of the signal.
- The $(\cos\theta_{K^*}, \cos\theta_l)$ shape of the crossfeed contributions.
- The $(\cos\theta_{K^*}, \cos\theta_l)$ shape of the peaking background.

## 4.7 Conclusion

This chapter has given a detailed description of the fitting strategy for both the Run 5 and Run 6 analyses. For the Run 5 analysis only Fit One, Two and Three will be performed. For the Run 6 analysis all of the fits will be performed. The signal and background PDFs for both analyses are constructed identically with the exception of the crossfeed component. In the Run 5 analysis the feed-across and self-crossfeed components are modelled using two separate PDFs whereas the Run 6 analysis uses the sum of the crossfeed components, this inclusive crossfeed component is then modelled using one PDF. Chapter 6 and 5 will validate the fitting technique for the Run 5 and Run 6 analysis, respectively.

| Mode | $q0$ | $q1$ | $q2$ | $q3$ |
|---|---|---|---|---|
| $B^+ \to K^0_S\pi^+\mu^+\mu^-$ | 0.101 | 0.104 | 0.095 | 0.106 |
| $B^0 \to K^+\pi^-\mu^+\mu^-$ | 0.222 | 0.222 | 0.425 | 0.385 |
| TOTAL | 0.323 | 0.326 | 0.520 | 0.491 |

Table 4.2: Number of expected hadronic peaking background events for each mode and $q^2$ bin.

| Mode | $q0$ bin | $q1$ bin | $q2$ bin | $q3$ bin |
|---|---|---|---|---|
| $B^+ \to J/\Psi K^0_s\pi^+$ | 0.29 | 1.75 | 0.99 | 0.03 |
| $B^0 \to J/\Psi K^+\pi^-$ | 0.61 | 3.94 | 2.33 | 0.04 |
| TOTAL $J/\Psi K^*$ | 0.9 | 5.69 | 3.32 | 0.07 |
| $B^+ \to \Psi(2S)K^0_s\pi^+$ | 0.03 | 0.01 | 0.58 | 0.16 |
| $B^0 \to \Psi(2S)K^+\pi^-$ | 0.07 | 0.08 | 1.36 | 0.56 |
| TOTAL $\Psi(2S)K^*$ | 0.10 | 0.09 | 1.94 | 0.72 |

Table 4.3: Number of charmonium peaking background events by mode and $q^2$ bin.

# 5

# Validation of Fitting Technique

In this chapter the validation of the fit technique will be discussed for the Run 6 analysis where measurements are made in four $q^2$ bins: $q^2$: 0.10 - 4.00 GeV$^2/c^4$, 4.00 - 8.00 GeV$^2/c^4$, 10.24 - 12.96 GeV$^2/c^4$ and $>$14.06 GeV$^2/c^4$. There are two methods that are used to test the fitting technique. The first involves fits to charmonium data, $B \rightarrow J/\Psi K^*$, where $J/\Psi \rightarrow l^+l^-$, with a branching fraction 1000 times greater than $B \rightarrow K^*l^+l^-$. The topologies of the two decays are almost identical making the charmonium data an ideal control sample, the fit method and results will be discussed in Sections 5.1.1. The second validation method involves generating ensembles of Monte Carlo samples with the expected $B \rightarrow K^*l^+l^-$ distribution and then fitting these samples. This validation method is called a "toy study" and the ensembles of samples are "toy datasets". The results from the toy studies will be discussed in Section 5.2. Toy studies are also used to determine the number of $q^2$ bins that $F_L$ and $A_{FB}$ will be measured in Section 5.2.3.

## 5.1 Charmonium Control Sample

The $B \rightarrow J/\Psi K^*$ events are required to pass all of the selection cuts for $B \rightarrow K^*l^+l^-$ except for the charmonium vetoes, described in Section 3.10. These fits are used to study the efficiency of the selection cuts and to cross-check the fit methodology. The result from the $B \to J/\Psi K^*$ $m_{ES}$ fit is used to fix the $m_{ES}$ Gaussian for the $B \to K^* l^+ l^-$ fit.

### 5.1.1 $B \to J/\Psi K^*$ Validation

The charmonium $m_{ES}$ distribution is fitted with a Gaussian and the Argus function for the signal and combinatoric background components, respectively. Figure 5.1 shows the $m_{ES}$ fit.

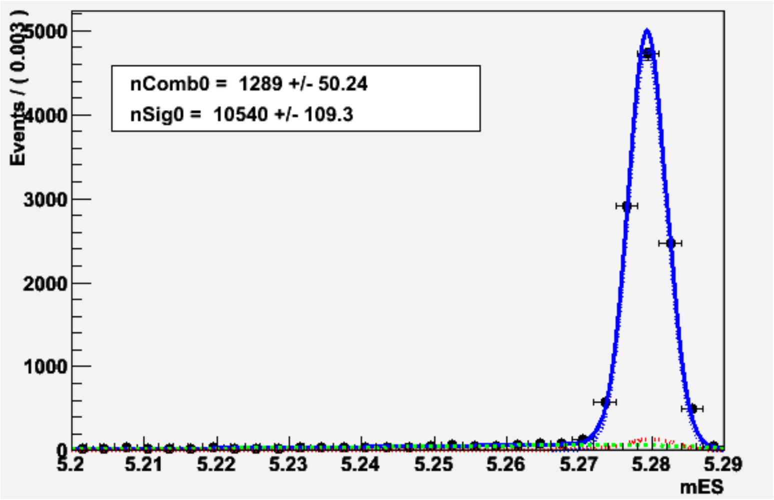

Figure 5.1: Fit to $m_{ES}$ for the $B \to J/\Psi K^*$ combined dataset. Total fit (solid blue line), signal (dashed blue), combinatoric background (dashed green), total crossfeed (dashed red).

The 1D fits and the 2D fit to extract $F_L$ and $A_{FB}$ are then performed. The fit procedure is derived in the same way as for $B \to K^* l^+ l^-$, however, it does not contain a component for the charmonium leakage or for the very small hadronic peaking background. The 2D fit results are shown in Figures 5.2 and 5.3, and the 1D fits are in the Appendix, Figures 8.7 and 8.8. The value for $F_L$ is expected to be 0.56 and $A_{FB}$ fit is expected to be null [85]. The results for both fit methods are shown in Table 5.1 with the 2D fit method producing a smaller error. It can be seen that there is a slight tilt in the fit to $\cos\theta_{K*}$, the total fit is higher/lower on the left/right-hand side. This is because the s-wave component is not modelled in the fits. The decay $B \to J/\Psi K^*$ is followed by the two-body decay of the $K^*$, the meson pair produced is an orbital P-wave amplitude. However, near the $K^*$ mass peak there can be a contribution from the S-wave partial wave [84]. The $B \to K^* l^+ l^-$ is also followed by the same two-body decay of the $K^*$, it is expected that it will also contain a small S-wave component. However, the previous BABAR analysis that studied $B \to J/\Psi K^*$ extensively tested the fit with and without the s-wave component. They found that by including the s-wave component the fit did improve, however, it did not affect the central value obtained from the fit. Therefore, the S-wave of the significantly statistically smaller $B \to K^* l^+ l^-$ dataset will be negligible.

| Fit type | $J/\Psi$ $F_L$ | Err | $J/\Psi$ $A_{FB}$ | Err |
|---|---|---|---|---|
| 1D fits | 0.557 | 0.008 | -0.011 | 0.009 |
| 2D fit | 0.553 | 0.007 | -0.012 | 0.007 |

Table 5.1: $B \to J/\Psi K^*$ $F_L$ and $A_{FB}$.

As previously mentioned, the fit results from the $m_{ES}$ signal Gaussian in Table 5.2 are used to parameterise the $m_{ES}$ signal Gaussian mean and width for the $B \to K^* l^+ l^-$ fit.

## 5.2 Toy Monte Carlo Studies

This method generates MC samples with the expected angular distributions and then fits these samples with the same angular distributions to measure any biases that exist from the fitting strategy.

As discussed in Section 4.2, four different methods of implementing the two-dimensional efficiency corrections were explored. Toy studies were used to determine the most effective way of performing the efficiency correction. They measured how precisely $F_L$ and $A_{FB}$ can be found. Toy studies were also used to establish the definition of a "good fit", (see Section 5.2.3). An ensemble of three hundred toy studies are generated for each region of $q^2$.

These toy studies can be carried out in different ways to examine the behaviour of different components of the fit. For a "pure signal" toy study only the 2D

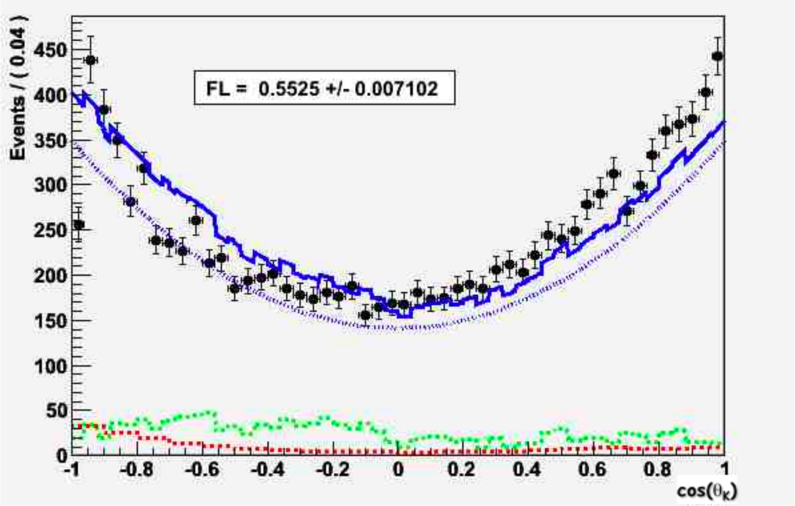

Figure 5.2: Fit to $F_L$ for the $B \to J/\Psi K^*$ combined dataset. Total fit (solid blue line), signal (dashed blue), combinatoric background (dashed green), total crossfeed (dashed red).

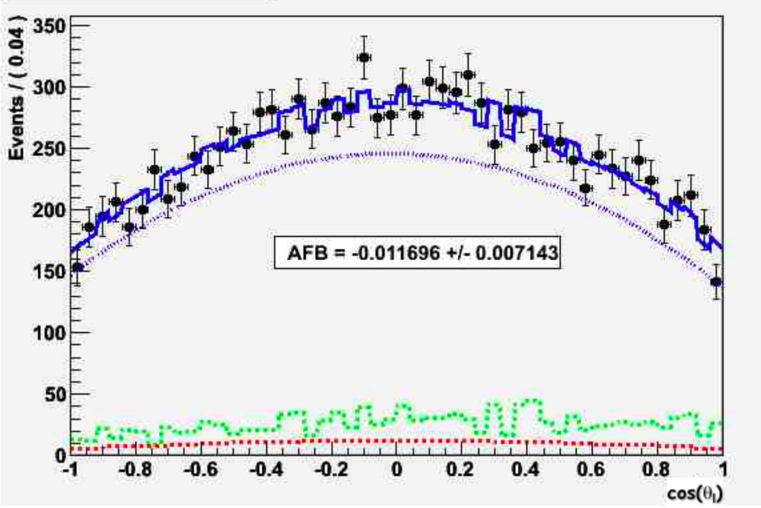

Figure 5.3: Fit to $A_{FB}$ for the $B \to J/\Psi K^*$ combined dataset. Total fit (solid blue line), signal (dashed blue), combinatoric background (dashed green), total crossfeed (dashed red).

| Mode | Gaussian Mean (GeV) | Gaussian Sigma (MeV) |
|---|---|---|
| Combined $K^*l^+l^-$ | 5.27933 ± 0.00003 | 2.635 ± 0.023 |

Table 5.2: $B \rightarrow J/\Psi K^*$ $m_{ES}$ PDF shape parameter. The listed central values and errors.

$(\cos\theta_K, \cos\theta_l)$ differential distribution and the efficiency histogram from Equation 1.3.8 are used to generate toy datasets. These toy datasets were used to explore different techniques for the efficiency correction. A "signal embedded" toy study uses the combinatoric and peaking background PDFs from Sections 4.3 and 4.5 to generate the toy datasets then signal events were randomly selected from exclusive signal MC samples and embedded in the toy datasets. These toy datasets include any detector or reconstruction affects and were used to validate the fitting strategy.

The pull is a measure of the amount that a fit parameter differs from the expected value and can be defined by:

$$Pull = \frac{x_{fit} - x_{exp}}{x_\sigma}$$

where $x_{exp}$, $x_{fit}$, $x_\sigma$ are the expected value, the fit value and the error, respectively, for a given parameter $x$. The pull distribution is plotted for each ensemble and fitted with a Gaussian. The Gaussian for a toy study with no bias will have a mean of zero and an RMS of one. Any deviation in the mean indicates a bias in the central value from the fit, and if the RMS differs from one, this is evidence of a bias in the error from the fit.

### 5.2.1 "Pure Signal" Toy Studies - $F_L$, $A_{FB}$

For the 2D fit to extract $F_L$ and $A_{FB}$ four different fit techniques were investigated in order to establish a method for applying the efficiency correction. The toy datasets were generated using the product of the $(\cos\theta_K, \cos\theta_l)$ differential distribution (Equation 1.3.8) and the efficiency histogram PDF. The four different fit techniques were:

- Method 1 - Fit the toy datasets using the product of the $(\cos\theta_K, \cos\theta_l)$ differential distribution and the efficiency histogram PDF. The pull distributions for this method were within $1\sigma$. However, each fit took over 12 hours to converge. The time required to run thousands of toy studies would be too large, therefore, it was decided that this method was not feasible.

- Method 2 - Each event in the toy dataset was weighted by the efficiency, then fitted with only the $(\cos\theta_K, \cos\theta_l)$ differential distribution. Using this method, the central values for values for $F_L$ and $A_{FB}$ were within $1\sigma$, however, the errors on the central value were too small, producing a large RMS for the pulls. This arises from the way weights are handled within a log-likelihood fit. The event is weighted before the error calculation, therefore the errors are too small by a factor of $\frac{1}{\sqrt{weight}}$. To illustrate this a flat efficiency of 11% was produced, the toy datasets were weighted by 11% and then fit. Figure 5.4 shows the pull distribution for $A_{FB}$, it can be seen that the Gaussian mean is within $1\sigma$ however the RMS is too large by a factor of $\frac{1}{\sqrt{11}}$.

- Method 3 - In order to overcome the problem with Method 2, the toy datasets were divided into bins. This binned dataset was fit using a $\chi^2$ method, where the errors were calculated without the weights, therefore artificially small errors do not occur. However, this is a statistics limited analysis and therefore fine binning would result in bins with no events in them causing the fits to fail. If the bin size was increased the small number of bins made the measurements less sensitive.

- Method 4 - Uses the same technique as Method 2 but with the weights renormalised. The weight of each event was divided by the average weight before the toy datasets were fitted. Using the example above with a flat efficiency of 11%, the weights were renormalised and the toy dataset was fit. Figure 5.5 shows the resulting pull with the correct pull distribution, therefore this method is robust.

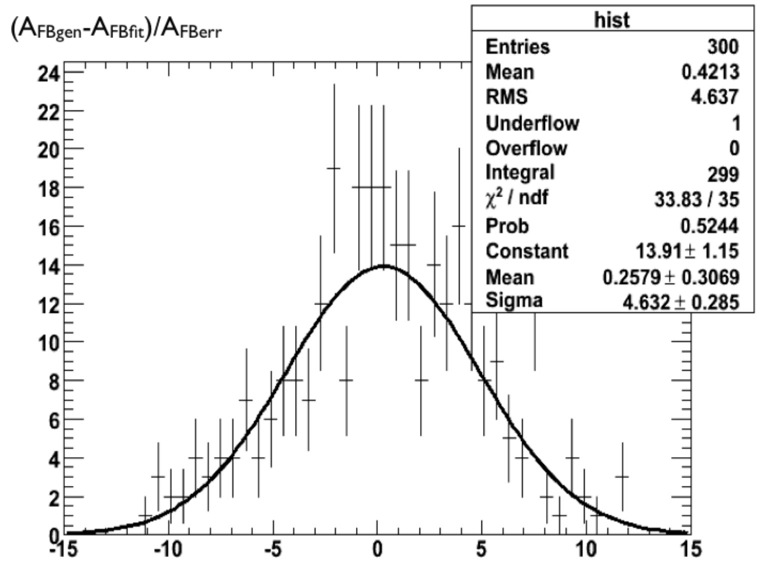

Figure 5.4: Toy study for Method 2 - the Gaussian mean is consistent with zero, however, the RMS is too large by a factor of $\frac{1}{\sqrt{weight}}$. $A_{FB_{gen}}$ is the generated value, $A_{FB_{fit}}$ is the value obtained from the fit and $A_{FB_{err}}$ is the error on the fitted value of $A_{FB}$.

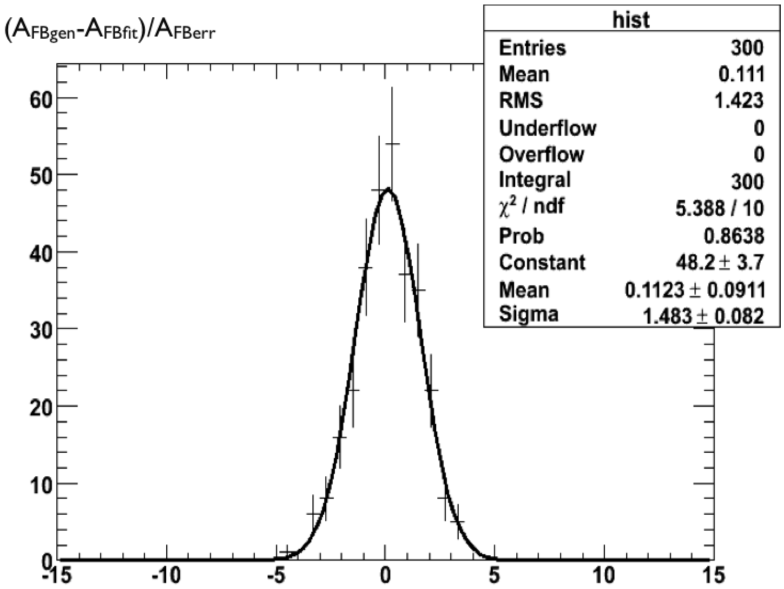

Figure 5.5: Toy study for Method 4 - the Gaussian mean is consistent with zero and the RMS is within $1\sigma$ from 1. $A_{FB_{gen}}$ is the generated value, $A_{FB_{fit}}$ is the value obtained from the fit and $A_{FB_{err}}$ is the error on the fitted value of $A_{FB}$.

| $q^2$ bin | Stat Mean | Stat RMS | Fit Mean | Fit Sigma |
|---|---|---|---|---|
| $q0$ | 0.273 | 1.010 | 0.266 | 1.010 |
| $q1$ | 0.263 | 0.995 | 0.273 | 0.993 |
| $q2$ | 0.296 | 0.975 | 0.279 | 0.976 |
| $q3$ | 0.254 | 0.990 | 0.271 | 1.028 |

Table 5.3: “Signal Embedded“ number of signal events from $m_{ES}$ pull results.

### 5.2.2 “Signal Embedded” Toy Studies - $F_L$, $A_{FB}$

The toy MC is generated in the following way: the hadronic peaking events are generated from the PDF found in Section 4.5; the combinatoric background events are generated from a PDF produced by a fit to the generic background MC; lastly, the signal and crossfeed events are drawn from the signal MC and embedded into the background sample. The number of signal and background events are generated according to the number of expected events in Table 3.8. The toy dataset is then re-weighted by the efficiency as described in Method 4 and fit.

The signal yield pull distributions for each $q^2$ bin are shown in Figure 5.6. The parameters from the Gaussian fit to the pull distribution are shown in Table 5.3. The results show that there is $\sim$1 $\sigma$ deviation from the expected value.

The $F_L$ and $A_{FB}$ pull distributions are shown in Figure 5.7. The parameters from the Gaussian fit to the pull distribution for $F_L$ are in Table 5.4 and for $A_{FB}$ are in Table 5.5.

| $q^2$ bin | Stat Mean | Stat RMS | Fit Mean | Fit Sigma |
|---|---|---|---|---|
| $q0$ | 0.031 | 1.185 | 0.054 | 1.179 |
| $q1$ | 0.634 | 1.182 | 0.540 | 0.950 |
| $q2$ | 0.380 | 1.390 | 0.309 | 1.172 |
| $q3$ | 0.500 | 1.182 | 0.477 | 1.089 |

Table 5.4: “Signal embedded” toy $F_L$ pull results.

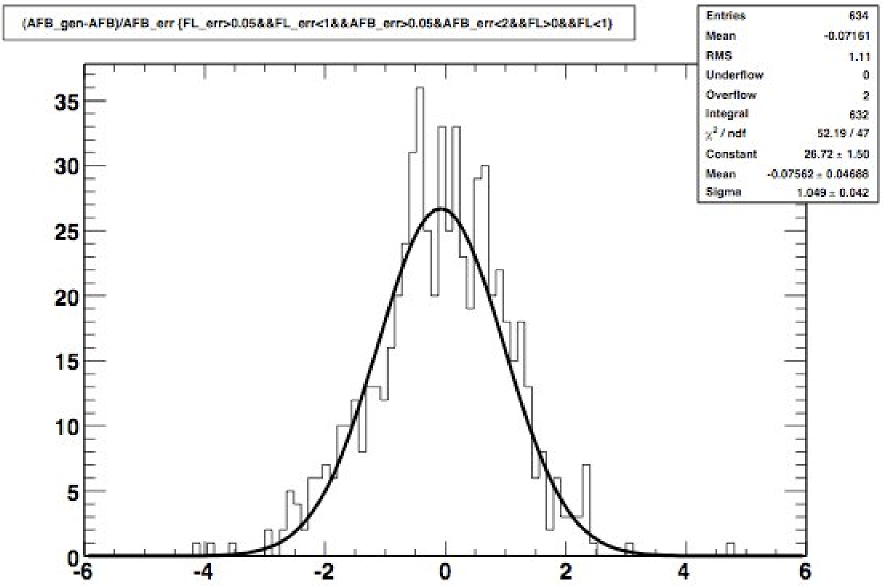

Figure 5.6: Signal embedded toy $m_{ES}$ pull results.

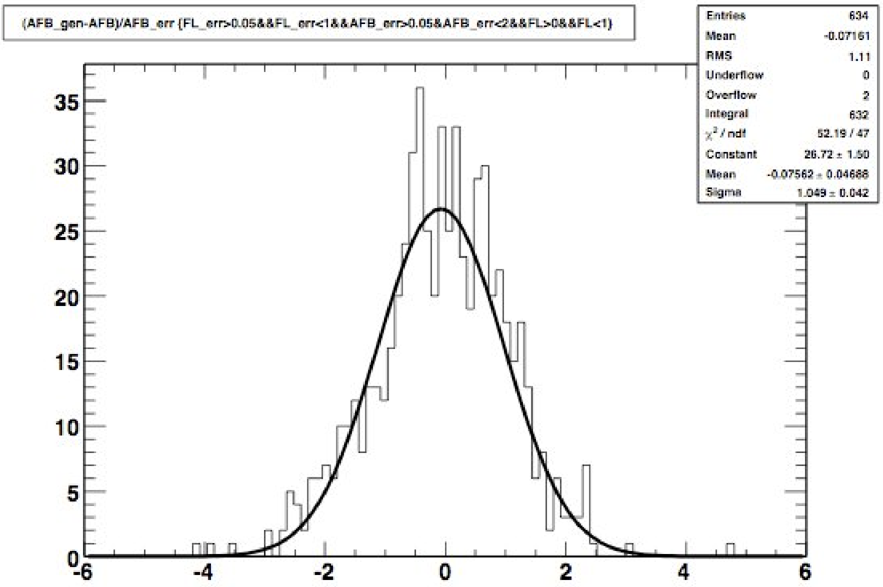

Figure 5.7: "Signal embedded" toy $F_L$, $A_{FB}$ pull results.

| $q^2$ bin | Stat Mean | Stat RMS | Fit Mean | Fit Sigma |
|---|---|---|---|---|
| $q0$ | 0.280 | 1.344 | 0.128 | 1.179 |
| $q1$ | 0.118 | 1.07 | 0.12 | 1.04 |
| $q2$ | 0.221 | 1.144 | 0.318 | 1.149 |
| $q3$ | 0.346 | 1.156 | 0.332 | 1.109 |

Table 5.5: "Signal embedded" toy $A_{FB}$ pull results.

### 5.2.3 Definition of Good Fit

The error distributions for $F_L$ and $A_{FB}$ from the signal embedded toy fits shown in Figures 5.8 and 5.9 have two features. A small fraction of fits have very small errors from fits that did not converge properly. Secondly, a few toy datasets with large errors produce a long tail from fits in where the signal yield was too low. To reject these bad fits, the allowed values for the errors are above 0.05 and no larger than the full range of $F_L$ and $A_{FB}$:

- the error on $F_L$ be $0.05 < \sigma(F_L) < 1.00$;
- the error on $A_{FB}$ be $0.05 < \sigma(A_{FB}) < 2.00$

The number of $q^2$ bins that $F_L$ and $A_{FB}$ could be measured in was determined by the fraction of good fits. If the fraction of good fits in a particular $q^2$ bin was greater than 80% then $F_L$ and $A_{FB}$ were deemed to be measureable.

After performing these studies it was decided that $F_L$ and $A_{FB}$ would be measured in four bins of $q^2$. The error distribution for $F_L$ and $A_{FB}$ are shown in Figures 5.8 and 5.9.

## 5.3 Conclusion

This chapter described two techniques that were used to validate the fitting technique for the Run 6 analysis. The first technique involved fitting the charmonium data, $B \to J/\Psi K^*$, where $J/\Psi \to l^+l^-$ using the same fitting strategy

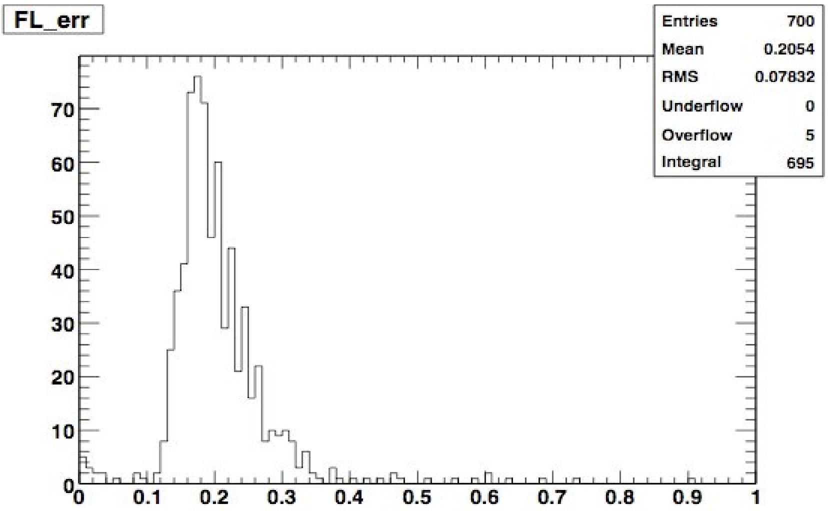

Figure 5.8: $F_L$ error distributions.

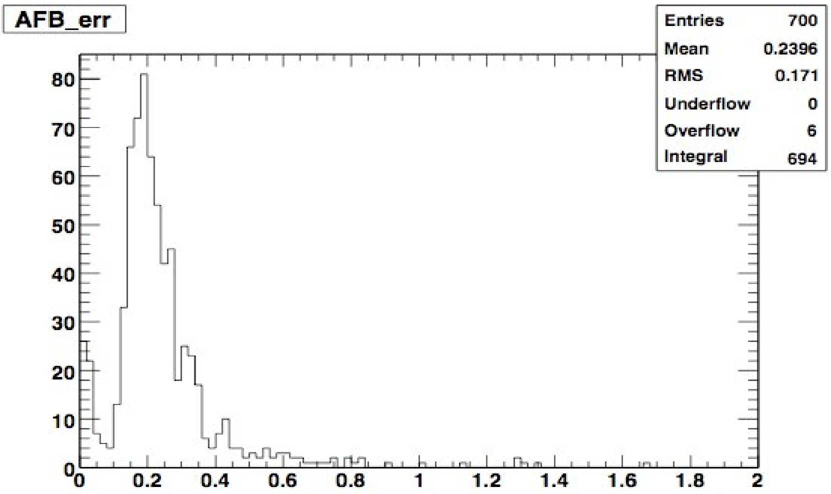

Figure 5.9: $A_{FB}$ error distributions.

that will be used for $B \rightarrow K^{*}l^{+}l^{-}$. The results from these fits were in good agree with the previous BABAR measurement. The statistical error on the two-dimensional fits was found to be $\sim 20\%$ smaller than the one-dimensional fits. The second technique involved performing "signal embedded" toy studies. The pull distributions generated from these toy studies confirm that fitting methodology is performing as expected. The "signal embedded" toy studies were also used to decide that $F_L$ and $A_{FB}$ would be measured in four bins of $q^2$.

# 6

# Run 5 Analysis

In this chapter the validation and results for the Run 5 analysis will be presented. This analysis used a dataset of 384 million $B\overline{B}$ events collected by the BABAR detector. $F_L$ and $A_{FB}$ were measured in two $q^2$ bins, the "low" region 0.1< $q^2$ < 6.5 GeV$^2/c^4$ and a "high" region above the $J/\Psi$ resonance $q^2$ > 10.24 GeV$^2/c^4$. The angular distributions are fitted using the 1D fit technique described in Chapter 4.

Sections 6.1.1 and 6.1.4 will show the results from the charmonium validation and the toy studies for the Run 5 analysis. The final results for this analysis will be presented in Section 6.2, followed by a discussion of systematic errors in Section 6.3.

## 6.1 Validation

### 6.1.1 Charmonium Control Sample

The $B \rightarrow J/\Psi K^*$ and $B \rightarrow \Psi(2S)K^*$ events are required to pass all of the selection cuts for the Run 5 analysis of $B \rightarrow K^* l^+ l^-$, except for the charmonium vetoes, as defined in Section 3.6.2. The different event selections for each of the $q^2$ bins were applied to the Charmonium samples, therefore the validation is performed for each of the selections. Due to the large statistics it is possible to perform the angular fits separately for each of the six signal modes. The individual fits are used to study the efficiency of the selection cuts across the different modes. The six signal modes are then combined and the fit is performed again. The result from the combined fit is used to fix the variables for the $m_{ES}$ signal Gaussian.

### 6.1.2 $B \to J/\Psi K^*$ Validation

The $B \to J/\Psi K^*$ $m_{ES}$ distribution is fitted with a Gaussian and the Argus function for the signal and combinatoric background components, respectively. The self-crossfeed is modelled in the same way as described in Section 4.4.2 using charmonium signal MC samples. The branching fraction for each mode is calculated as follows:

$$B = \frac{N_{B_{FIT}}}{\epsilon \times B(J/\Psi) \times B(K^*) \times N_{B_{TOT}}}$$

where $N_{B_{FIT}}$ is the number of signal events extracted from the fit, $\epsilon$ is the efficiency from the signal MC, $B(J/\Psi)$ is the branching fraction of the $J/\Psi$ decaying to either $e^+e^-$ or $\mu^+\mu^-$, $B(K^*)$ is the branching fraction of the $K^*$ decaying to $K\pi$, and $N_{B_{TOT}}$ is the total number of $B^+$ or $B^0$ mesons in the dataset. The results can then be compared to the PDG values.

Figure 6.1 shows the $m_{ES}$ fit to the combined dataset and Table 6.1 summarises the branching fraction results determined from the fit. The PDG 2006 values for $B^+ \to J/\Psi K^+$, $B^0 \to J/\Psi K^{*0}$ and $B^0 \to J/\Psi K^{*+}$ are $(1.08 \pm 0.0035, 1.33 \pm 0.06, 1.41 \pm 0.08) \times 10^{-3}$, respectively. The results across the modes agree well with the PDG values.

The 1D fits to $\cos\theta_K$ and $\cos\theta_l$ to extract $F_L$ and $A_{FB}$ are then performed. The fit procedure is derived in the same way as for $B \to K^*l^+l^-$, however, it does not contain a component for the charmonium leakage or for the very small hadronic peaking background. These fits are also performed for each mode individually before the combined fit. The $\cos\theta_K$ fit is shown in Figure 6.2 and the $\cos\theta_l$ fit is in Figure 6.3. The value for $F_L$ is expected to be 0.56 and $A_{FB}$

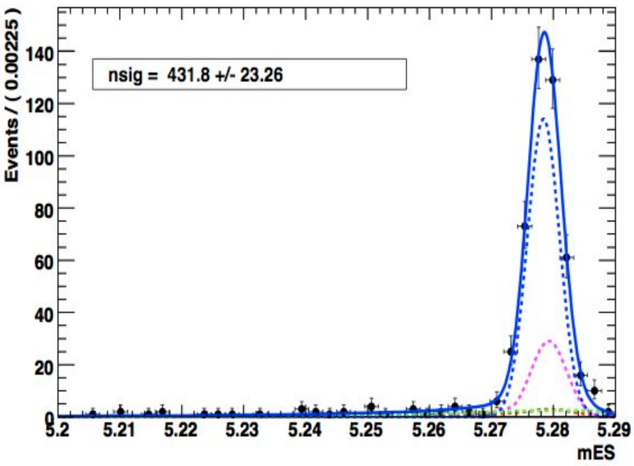

Figure 6.1: Fit to $m_{ES}$ for the $B \rightarrow J/\Psi K^*$ combined dataset. Total fit (solid blue line), signal (dashed blue), combinatoric background (dashed green), self-crossfeed (dashed magneta), crossfeed (dashed red).

fit is expected to be null in the SM. The results for both $F_L$ and $A_{FB}$ are both shown in Table 6.2 and are within $2\sigma$ of the previous result from BABAR [85].

### 6.1.3 $\Psi(2S)$ Validation

The $B \rightarrow \Psi(2S)K^*$ is performed using the same fit technique as the $J/\Psi$ sample. The results for all modes are in good agreement with the PDG values. Figure 6.5 shows the fits to the combined dataset to extract $F_L$ and $A_{FB}$. Table 6.3 shows the results for the branching fraction, $F_L$ and $A_{FB}$ for each mode.

### 6.1.4 "Signal Embedded" Toy Studies

The toy datasets are generated using the method described in Section 5.2.2. The number of signal and background events are generated according to the number of events expected from a luminosity of $350 fb^{-1}$, shown in Table 3.5.

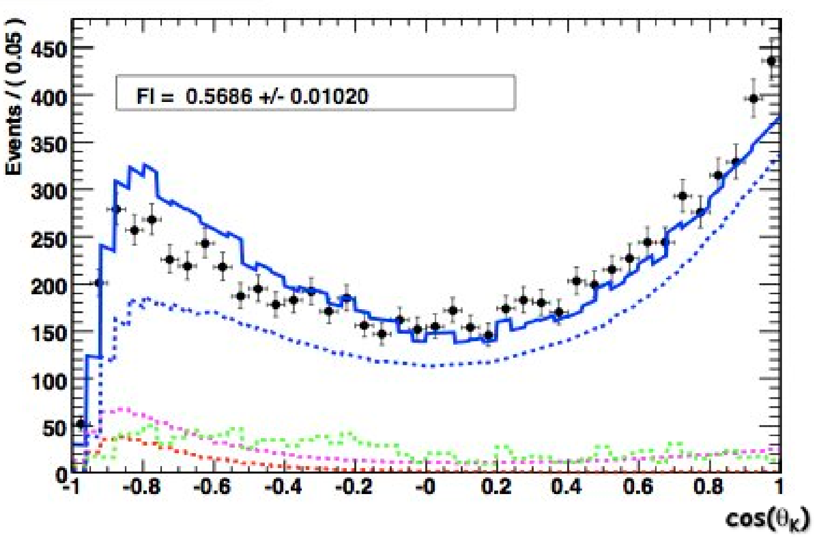

Figure 6.2: Fit to $F_L$ for the $B \to J/\Psi K^*$ combined dataset. Total fit (solid blue line), signal (dashed blue), combinatoric background (dashed green), self-crossfeed (dashed magneta), crossfeed (dashed red).

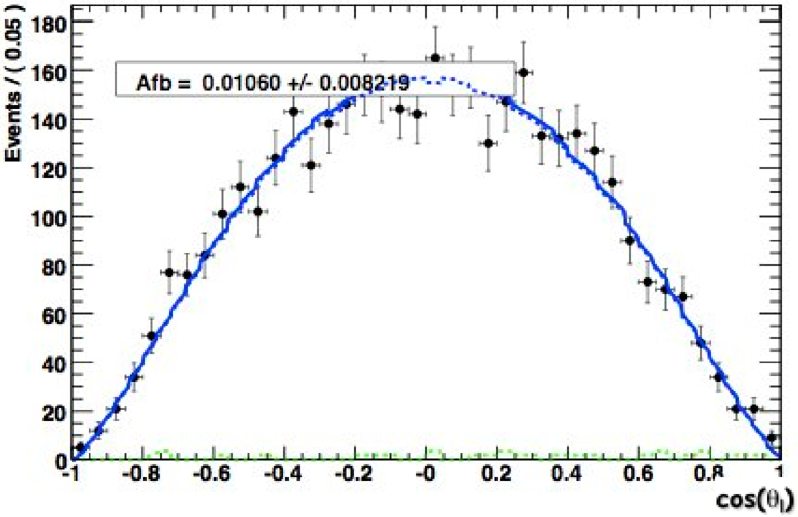

Figure 6.3: Fit to $A_{FB}$ for the $B \to J/\Psi K^*$ combined dataset. Total fit (solid blue line), signal (dashed blue), combinatoric background (dashed green), self-crossfeed (dashed magneta), crossfeed (dashed red).

| Mode | NN cuts ($q^2$ bin) | $J/\psi$ BF ($/10^{-3}$) | Stat Err ($/10^{-3}$) | Discrepancy ($\sigma$) |
|---|---|---|---|---|
| $B^+ \to K^+\mu^+\mu^-$ | q0 | 1.003 | 0.017 | −0.1 |
| | q1 | 1.026 | 0.016 | 0.5 |
| | q2 | 1.011 | 0.016 | 0.1 |
| | q3 | 1.011 | 0.016 | 0.1 |
| $B^+ \to K^+e^+e^-$ | q0 | 1.030 | 0.013 | 0.6 |
| | q1 | 1.031 | 0.014 | 0.7 |
| | q2 | 1.035 | 0.013 | 0.8 |
| | q3 | 1.040 | 0.014 | 0.9 |
| $B^+ \to K^+\pi^0\mu^+\mu^-$ | q0 | 1.45 | 0.08 | 0.5 |
| | q1 | 1.45 | 0.08 | 0.5 |
| | q2 | 1.50 | 0.09 | 1.0 |
| | q3 | 1.50 | 0.08 | 1.1 |
| $B^+ \to K^0_s\pi^+\mu^+\mu^-$ | q0 | 1.49 | 0.08 | 1.0 |
| | q1 | 1.49 | 0.07 | 1.1 |
| | q2 | 1.43 | 0.08 | 0.3 |
| | q3 | 1.48 | 0.07 | 1.0 |
| $B^0 \to K^+\pi^-\mu^+\mu^-$ | q0 | 1.222 | 0.032 | −1.8 |
| | q1 | 1.241 | 0.033 | −1.5 |
| | q2 | 1.300 | 0.031 | −0.5 |
| | q3 | 1.276 | 0.033 | −0.9 |
| $B^+ \to K^+\pi^0e^+e^-$ | q0 | 1.547 | 0.066 | 1.7 |
| | q1 | 1.544 | 0.064 | 1.7 |
| | q2 | 1.573 | 0.061 | 2.0 |
| | q3 | 1.612 | 0.055 | 2.5 |
| $B^+ \to K^0_s\pi^+e^+e^-$ | q0 | 1.477 | 0.056 | 0.8 |
| | q1 | 1.429 | 0.065 | 0.2 |
| | q2 | 1.481 | 0.059 | 0.9 |
| | q3 | 1.486 | 0.057 | 1.0 |
| $B^0 \to K^+\pi^-e^+e^-$ | q0 | 1.378 | 0.032 | 0.8 |
| | q1 | 1.378 | 0.032 | 0.8 |
| | q2 | 1.345 | 0.028 | 0.3 |
| | q3 | 1.349 | 0.029 | 0.3 |

Table 6.1: $B \to J/\Psi K^*$ branching fraction by mode and $q^2$ bin selection.

| Mode | NN cuts ($q^2$ bin) | $J/\psi$ $F_L$ | Stat Err | $J/\psi$ $A_{FB}$ | Stat Err |
|---|---|---|---|---|---|
| $B^+ \to K^+\pi^0\mu^+\mu^-$ | q0 | 0.05 | 0.05 | −0.060 | 0.060 |
| | q1 | 0.50 | 0.05 | −0.060 | 0.060 |
| | q2 | 0.55 | 0.05 | −0.040 | 0.050 |
| | q3 | 0.55 | 0.05 | −0.040 | 0.050 |
| $B^+ \to K_s^0\pi^+\mu^+\mu^-$ | q0 | 0.43 | 0.05 | 0.006 | 0.053 |
| | q1 | 0.44 | 0.05 | 0.004 | 0.051 |
| | q2 | 0.49 | 0.05 | 0.001 | 0.055 |
| | q3 | 0.47 | 0.05 | 0.028 | 0.047 |
| $B^0 \to K^+\pi^-\mu^+\mu^-$ | q0 | 0.579 | 0.020 | −0.001 | 0.023 |
| | q1 | 0.592 | 0.021 | −0.003 | 0.025 |
| | q2 | 0.572 | 0.019 | −0.018 | 0.020 |
| | q3 | 0.578 | 0.020 | −0.010 | 0.022 |
| $B^+ \to K^+\pi^0e^+e^-$ | q0 | 0.596 | 0.037 | 0.005 | 0.037 |
| | q1 | 0.609 | 0.036 | −0.003 | 0.034 |
| | q2 | 0.595 | 0.030 | 0.016 | 0.029 |
| | q3 | 0.593 | 0.030 | 0.022 | 0.030 |
| $B^+ \to K_s^0\pi^+e^+e^-$ | q0 | 0.523 | 0.036 | −0.048 | 0.039 |
| | q1 | 0.515 | 0.042 | −0.017 | 0.050 |
| | q2 | 0.525 | 0.037 | −0.019 | 0.042 |
| | q3 | 0.540 | 0.035 | −0.046 | 0.039 |
| $B^0 \to K^+\pi^-e^+e^-$ | q0 | 0.581 | 0.017 | −0.001 | 0.020 |
| | q1 | 0.581 | 0.017 | −0.001 | 0.020 |
| | q2 | 0.572 | 0.016 | 0.010 | 0.017 |
| | q3 | 0.566 | 0.016 | −0.004 | 0.012 |

Table 6.2: $B \to J/\Psi K^*$ $F_L$ and $A_{FB}$ results by mode and $q^2$ bin selection.

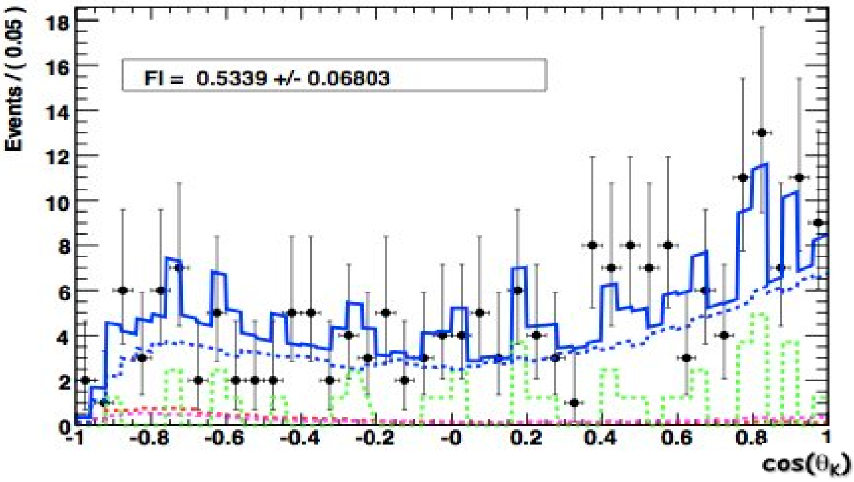

Figure 6.4: Fit to $F_L$ for the $B \to \Psi(2S)K^*$ combined dataset. Total fit (solid blue line), signal (dashed blue), combinatoric background (dashed green), self-crossfeed (dashed magneta), crossfeed (dashed red)

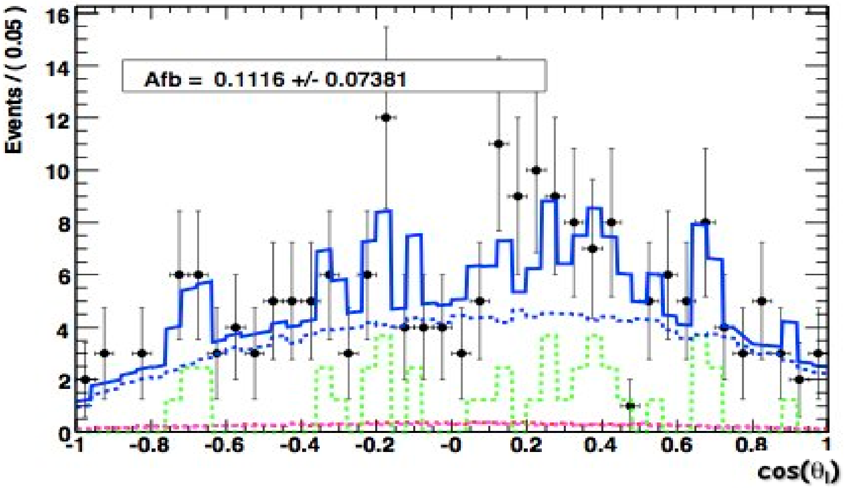

Figure 6.5: Fit to $A_{FB}$ for the $B \to \Psi(2S)K^*$ combined dataset. Total fit (solid blue line), signal (dashed blue), combinatoric background (dashed green), self-crossfeed (dashed magneta), crossfeed (dashed red)

| Mode | $\Psi(2S)$ BF ($10^{-3}$) | Err ($10^{-3}$) | $\Psi(2S)$ $F_L$ | Err | $\Psi(2S)$ $A_{FB}$ | Err |
|---|---|---|---|---|---|---|
| $B^0 \to K^+\pi^-\mu^+\mu^-$ | 0.72 | 0.07 | 0.513 | 0.083 | $-0.03$ | 0.09 |
| $B^+ \to K^+\pi^0 e^+e^-$ | 0.69 | 0.12 | 0.495 | 0.153 | $-0.12$ | 0.16 |
| $B^+ \to K^0_S\pi^+ e^+e^-$ | 0.69 | 0.13 | 0.582 | 0.157 | 0.31 | 0.15 |
| $B^0 \to K^+\pi^- e^+e^-$ | 0.71 | 0.06 | 0.534 | 0.068 | 0.11 | 0.07 |

Table 6.3: $\Psi(2S)$ branching fraction, $F_L$ and $A_{FB}$ by mode.

| $q^2$ bin | Stat Mean | Stat RMS | Fit Mean | Fit Sigma |
|---|---|---|---|---|
| low | -0.062 | 1.086 | $-0.069 \pm 0.041$ | $0.962 \pm 0.041$ |
| high | -0.089 | 1.065 | $-0.112 \pm 0.040$ | $0.993 \pm 0.035$ |

Table 6.4: Embedded toy $F_L$ pull results.

Seven hundred toy datasets were produced and fitted using the 1D fits technique. These studies were performed in each bin of $q^2$ and for both $B \to Kl^+l^-$ and $B \to K^*l^+l^-$. Figures 6.6 and 6.7 show the $F_L$ and $A_{FB}$ pull distributions in each $q^2$ bin. The parameters from the Gaussian fit to the pull distribution are tabulated in Tables 6.4 and 6.5 for $F_L$ and $A_{FB}$, respectively.

### 6.1.5 Definition of a Good Fit

The definition of a good fit was described in Section 5.2.3. For this analysis the same cuts are used to reject fits that are classed as "failed". The $F_L$ and $A_{FB}$ errors must not exceed the full range of $A_{FB}$ and $F_L$, and further require:

- the error on $F_L$ be $0.05 < \sigma(F_L) < 1.00$;

| $q^2$ bin | Stat Mean | Stat RMS | Fit Mean | Fit Sigma |
|---|---|---|---|---|
| low | $-0.072$ | 1.11 | $-0.076 \pm 0.047$ | $1.049 \pm 0.042$ |
| high | $-0.090$ | 1.13 | $-0.118 \pm 0.052$ | $1.121 \pm 0.042$ |

Table 6.5: Embedded toy $A_{FB}$ pull results.

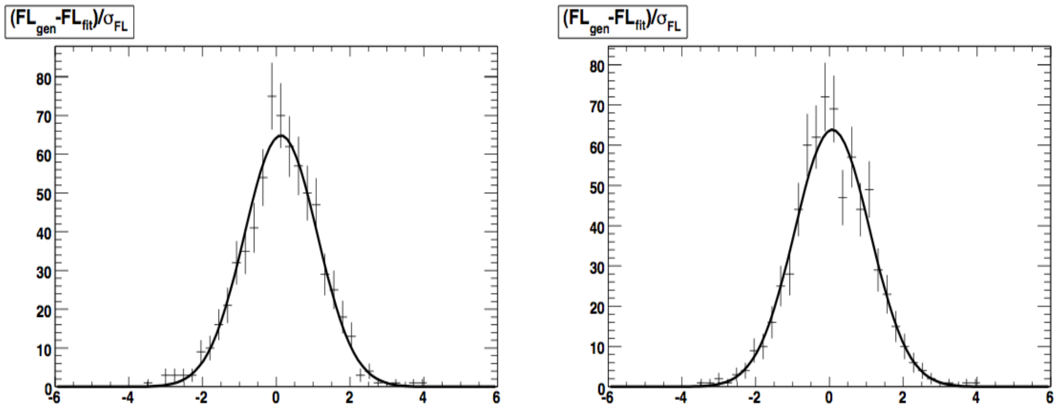

Figure 6.6: Pulls for embedded $F_L$ toys. Left: low $q^2$. Right: high $q^2$.

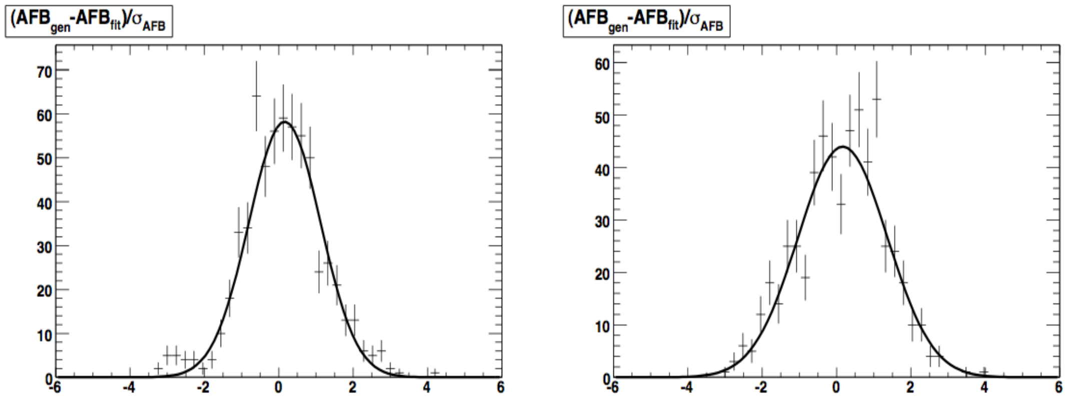

Figure 6.7: Pulls for embedded $A_{FB}$ toys. Left: low $q^2$. Right: high $q^2$.

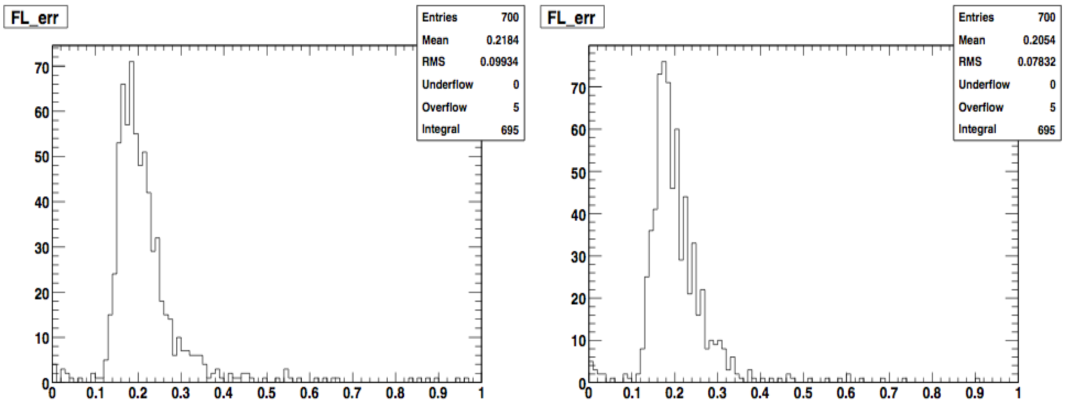

Figure 6.8: Error distribution from $F_L$ embedded toys:. Left: low $q^2$. Right: high $q^2$.

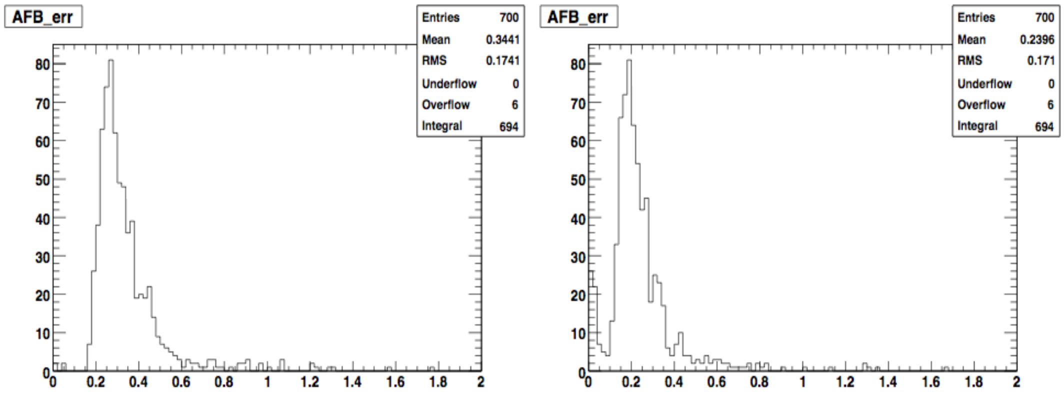

Figure 6.9: Error distribution from $F_L$ embedded toys:. Left: low $q^2$. Right: high $q^2$.

- the error on $A_{FB}$ be $0.05 < \sigma(A_{FB}) < 2.00$.

The error distributions for the 1D fits to $F_L$ and $A_{FB}$ are plotted in Figure 6.8 and 6.9, respectively.

## 6.2 Results

### 6.2.1 Unblinding Strategy

The analysis until this point was "blind", meaning that the $B \to K^{+}l^{+}l^{-}$ and $B \to K^{*}l^{+}l^{-}$ data in the signal region was never studied. This is a method enforced by the BABAR Collaboration to ensure that there is no human bias that enters into the fitting strategy and final result. The analysis undergoes review within the BABAR Collaboration, if the analysis technique is found to be satisfactory then the analysis can be "unblinded". This analysis was unblinded in several stages that are listed below. The four parts to the unblinding strategy were:

- The $B \to K^{+}l^{+}l^{-}$ modes were unblinded, the signal yield and $A_{FB}$ in the fit region were measured in each bin of $q^2$. The number of signal events was compared to the expected number events, this provided another validation of the selection cuts. For $B \to K^{+}l^{+}l^{-}$, $A_{FB}$ is theoretically expected to be null in the SM. The $A_{FB}$ measurement was consistent with the SM, therefore the fit model was known to be robust.
- The $B \to K^{*}l^{+}l^{-}$ signal yields were unblinded. The $m_{ES}$ fits were performed in each $q^2$ bin and the number of signal events was compared to the expected number of events in Table 3.5.
- The fit to $\cos\theta_K$ was performed to extract the value of $F_L$. There are two requirements that had to be met for the fit to be classed as successful: the fit must converge; and the error on $F_L$ must meet the conditions described in Section 5.2.3.
- The fit to $\cos\theta_l$ was performed to extract the value of $A_{FB}$ in each bin of $q^2$. The $\cos\theta_l$ fits passed the same requirements as the $\cos\theta_K$ fit, therefore they were classed as successful.

| $q^2$ bin | Exp. $N_S(q^2)$ | Fit $N_S(q^2)$ | Exp. $N_B(q^2)$ | Fit $N_B(q^2)$ |
|---|---|---|---|---|
| $B \to K^+l^+l^-$ | | | | |
| low | 18.4 | $26.9 \pm 5.8$ | 125.3 | $81.2 \pm 9.3$ |
| high | 15.5 | $24.9 \pm 6.7$ | 165.0 | $168.1 \pm 13.7$ |
| $B \to K^*l^+l^-$ | | | | |
| low | 8.9 | $27.0 \pm 10.2$ | 87.3 | $92.8 \pm 10.3$ |
| high | 13.0 | $15.4 \pm 7.3$ | 285.3 | $285.8 \pm 19.7$ |

Table 6.6: $B \to K^+l^+l^-$ and $B \to K^*l^+l^-$ expected (based on earlier *BABAR* measurements) and observed number of signal and background yields.

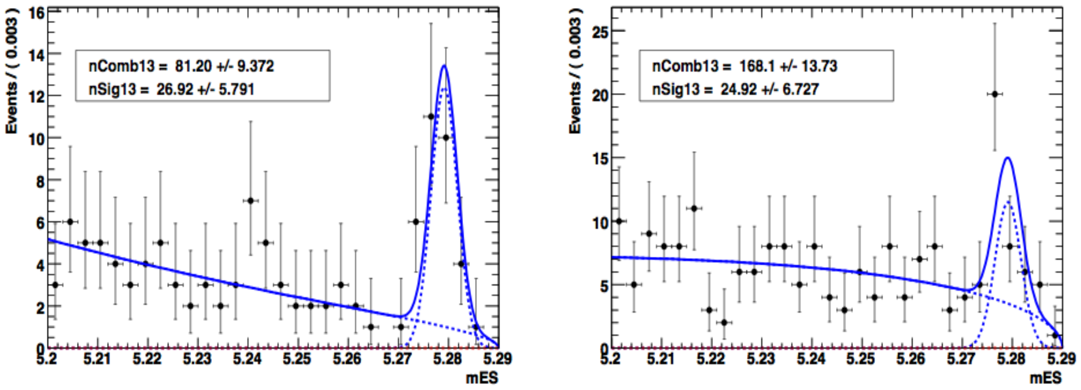

Figure 6.10: $B \to K^+l^+l^-$ fit to $m_{ES}$ distribution. Left: low $q^2$. Right: high $q^2$. Total fit (solid blue), signal (dashed blue), random combinatoric (dashed blue).

### 6.2.2 $B \to K^+l^+l^-$ and $B \to K^*l^+l^-$ $m_{ES}$ Fit Results

The signal yields are extracted from fits to the $m_{ES}$ distributions for $B \to K^+l^+l^-$ and $B \to K^*l^+l^-$ in each $q^2$ bin. Table 6.6 shows the expected and observed yields for both $B \to K^+l^+l^-$ and $B \to K^*l^+l^-$. Figures 6.10 and 6.11 show the $B \to K^+l^+l^-$ and $B \to K^*l^+l^-$ fits in each $q^2$ bin. The expected yields were calculated using the most recent branching fraction measurement from *BABAR*. The number for observed signal events was found to be roughly twice the number of expected events. These results are more consistent with Belle and less consistent with the previous result from *BABAR* [41].

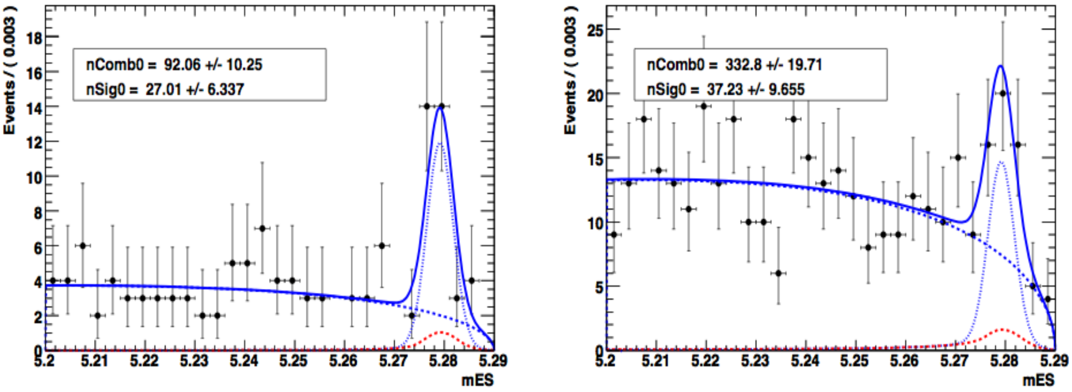

Figure 6.11: $B \to K^* l^+ l^-$ fit to $m_{ES}$ distribution. Left: low $q^2$ left. Right: high $q^2$. Total fit (solid blue), signal (dashed blue), random combinatoric (dashed blue).

| $q^2$ bin | $A_{FB}$ |
|---|---|
| low | $0.13^{+0.10}_{-0.12}$ |
| high | $0.20^{+0.18}_{-0.18}$ |

Table 6.7: $B \to K^+ l^+ l^-$ $A_{FB}$ fit results.

### 6.2.3 $B \to K^+ l^+ l^-$ $A_{FB}$ Fits

$B \to K^+ l^+ l^-$ does not have a distribution in $\cos\theta_K$ and $F_S$ is set to zero before the fit to $\cos\theta_l$ is performed. It is expected that $A_{FB}$ result will be null in both $q^2$ bins [65]. The fits to $B \to K^+ l^+ l^-$ are shown in Figure 6.12 and the $A_{FB}$ values from the fits are in Table 6.7.

### 6.2.4 $B \to K^* l^+ l^-$ $F_L$ and $A_{FB}$ Fits

The fits to $B \to K^* l^+ l^-$ in each bin of $q^2$ are shown in Figure 6.13. The plots on the left are the fits to $\cos\theta_K$ to extract $F_L$ and the plots on the right are the fits to $\cos\theta_l$ to extract $A_{FB}$. The values for $F_L$ and $A_{FB}$ obtained from the fit with the statistical error are in shown in Table 6.8. The final results for $F_L$ and $A_{FB}$ with the systematic error will be presented in Section 6.4.

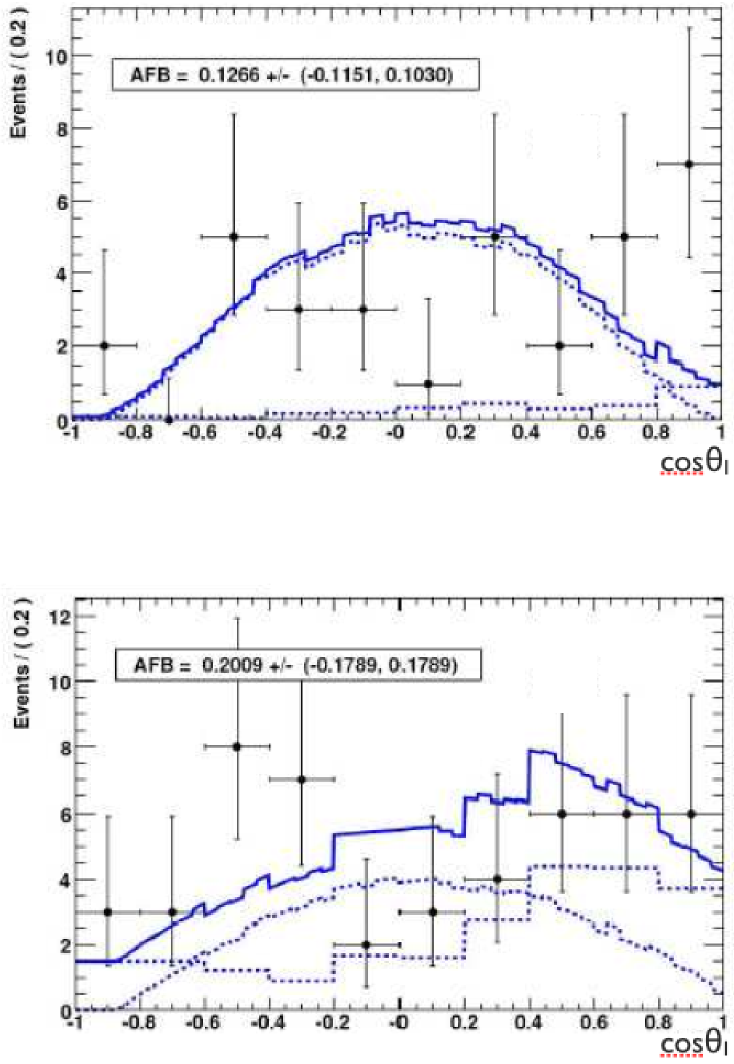

Figure 6.12: $B \to K^+ l^+ l^-$ $A_{FB}$ fits. Top plot: low $q^2$. Bottom plot: High $q^2$. Total fit (solid blue line), signal (quasi-continuous dotted blue line), random combinatoric (dotted blue line).

| $q^2$ bin | $F_L$ | $A_{FB}$ |
|---|---|---|
| low | $0.35 \pm 0.16$ | $0.24^{+0.18}_{-0.23}$ |
| high | $0.69^{+0.21}_{-0.23}$ | $0.76^{+0.49}_{-0.30}$ |

Table 6.8: $B \to K^* l^+ l^-$ $F_L$ and $A_{FB}$ fit results with statistical error.

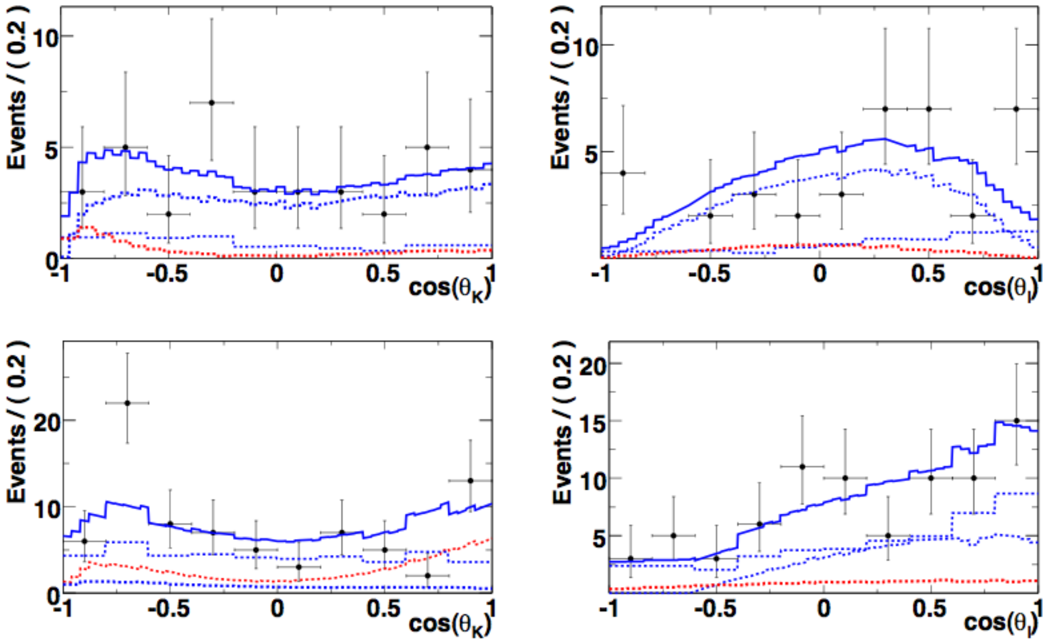

Figure 6.13: $B \to K^* l^+ l^-$ $F_L$ fits on the right and $A_{FB}$ fits on the left. Top plots: low $q^2$. Bottom plots: high $q^2$. Total fit (solid blue line), signal (quasi-continuous dotted blue line), random combinatoric (dotted blue line).

## 6.3 Systematic Errors

There are many systematic errors that propagate into the $F_L$ and $A_{FB}$ fit result. The sources of the systematic errors are listed below and are described in detail in the sections that follow:

- $m_{ES}$ fit yields - the error on the signal and background yield from the $m_{ES}$ fit.
- $F_L$ fit - the error on $F_L$ from the fit to $\cos\theta_K$ propagated into the $A_{FB}$ fit.
- Combinatoric background - the error on the combinatoric background shape and normalisation.
- Signal model - the error from assuming SM Wilson coefficients $C_7$, $C_9$ and $C_{10}$.
- Fit bias - the error introduced from the fitting technique.
- Crossfeed shape - the errors from the crossfeed shape and normalisation.
- $\Delta E$ fit window - the error from the selection of the $\Delta E$ fit window.
- Peaking background - the error on the peaking backgrounds from hadronic modes and charmonium leakage.

The $m_{ES}$ fit yield error was found by studying both the signal and background components of the $m_{ES}$ fit. For the signal component the mean and sigma of the Gaussian was varied by $\pm 1\sigma$ and then the $F_L$ and $A_{FB}$ fits were rerun. For the background component the Argus shape parameter was varied by $\pm 1\sigma$ and the fits were rerun. The average shift in the central $F_L$ and $A_{FB}$ values relative to the original fit was found and used as the systematic error.

The $F_L$ fit error was found by varying the central value of $F_L$ by $\pm 1\sigma$ relative to the original fit result. The $F_L$ value was then fixed and the $A_{FB}$ fit was performed again. The average shift in $A_{FB}$ relative to the original fit value after the $F_L$ variations was found and used as the systematic error.

The combinatoric background shape error was found by studying different $m_{ES}$ sideband regions: $5.23 < m_{ES} < 5.27$ GeV/$c^2$ and $5.20 < m_{ES} < 5.23$

GeV/$c^2$. The $F_L$ and $A_{FB}$ fits were rerun using the different sideband regions. Any shift in the final result relative to the original fit was assigned as the error.

The signal model error was found by varying the underlying physics model. The efficiency histograms were generated using signal MC with the SM Wilson coefficients. If this assumption was incorrect a systematic error would propagate into the efficiency histograms. The values of the Wilson coefficients were varied, new efficiency histograms were generated and the angular fits were rerun. The average shift in the central $F_L$ and $A_{FB}$ was assigned as the signal model systematic.

The fit bias error was taken from the "signal embedded" toy studies that were performed in Section 5.2.2. The error was found by calculating the average deviation of the pull mean from zero and then multiplying by the statistical error. This value was then assigned as the fit bias error.

The crossfeed shape error was found by studying the charmonium control samples. The ratio of the self-crossfeed and the normalisation of the feed-across were varied in turn and the angular fits were rerun, the average deviation from the original fit value was used as the systematic error.

The $\Delta E$ fit window error was found by varying the window between: $-0.04 < \Delta E < 0.04$ GeV and $-0.10 < \Delta E < 0.10$ GeV. Using each of the different windows the fits were rerun and it was found that the systematic associated with the choice in $\Delta E$ window was negligible.

The peaking background error was found by scaling the peaking background components. The peaking background were modelled in the fit using signal MC samples, therefore, the charmonuim leakage was scaled 10% to account for the uncertainty on the charmonium branching fraction and the hadronic peaking background was scaled by the error from the control sample. The angular fit were performed again and the systematic error was found to be negligible due to the small number of peaking background events.

| | $F_L$ systematic | | $A_{FB}$ systematic | |
|---|---|---|---|---|
| Source of Error | low $q^2$ | high $q^2$ | low $q^2$ | high $q^2$ |
| $m_{ES}$ fit yields | 0.001 | 0.016 | 0.003 | 0.002 |
| $F_L$ fit error | N/A | N/A | 0.025 | 0.022 |
| Combinatoric background | 0.006 | 0.020 | 0.027 | 0.006 |
| Signal model | 0.036 | 0.034 | 0.030 | 0.038 |
| Fit bias | 0.012 | 0.020 | 0.023 | 0.052 |
| Crossfeed | 0.010 | 0.010 | 0.020 | 0.020 |
| Total | 0.05 | 0.10 | 0.10 | 0.08 |

Table 6.9: Total systematic errors.

### 6.3.1 Total Systematic Error

The systematic errors described above are all independent of each other and are combined in quadrature. Since the $\Delta E$ fit window and peaking background systematic errors were found to be negligible, they are not included in the final error calculation. Table 6.9 shows the systematic errors associated with each of the different sources and gives the total systematic error.

## 6.4 Conclusion

The final results for $F_L$ and $A_{FB}$ with the statistical and systematic error are shown in Table 6.10. Figure 6.14 shows the results for $F_L$ and $A_{FB}$ with the expected SM and NP models. In the low $q^2$ bin the results for $F_L$ and $A_{FB}$ are $F_L = 0.35 \pm 0.16 \pm 0.05$ and $A_{FB} = 0.24^{+0.18}_{-0.23} \pm 0.10$, where the first error is statistical and the second is systematic. In the SM $F_L = 0.64$ and $A_{FB} = -0.03$ in the low $q^2$ bin. The measured results for $A_{FB}$ value are $\sim 1\sigma$ away from the SM and suggests that a "zero-crossing" at $q^2 \sim 4\,\text{GeV}^2/c^4$ might not be present.

In the high $q^2$ bin the results for $F_L$ and $A_{FB}$ are $F_L = 0.69^{+0.21}_{-0.23} \pm 0.10$ and $A_{FB} = 0.76^{+0.49}_{-0.30} \pm 0.08$. In the SM $F_L = 0.38$ and $A_{FB} = 0.44$ in the high $q^2$ bin. The measured results are consistent with the SM and exclude the flipped sign $C_9C_{10}$ scenario at more than a $3\sigma$ significance.

| $q^2$ bin | $F_L$ | $A_{FB}$ |
|---|---|---|
| low | $0.35 \pm 0.16 \pm 0.05$ | $0.24^{+0.18}_{-0.23} \pm 0.103$ |
| high | $0.69^{+0.21}_{-0.23} \pm 0.10$ | $0.76^{+0.49}_{-0.30} \pm 0.078$ |

Table 6.10: $B \rightarrow K^{*}l^{+}l^{-}$ $F_L$ and $A_{FB}$ final results for Run 5 where the first error is statistical and the second is systematic.

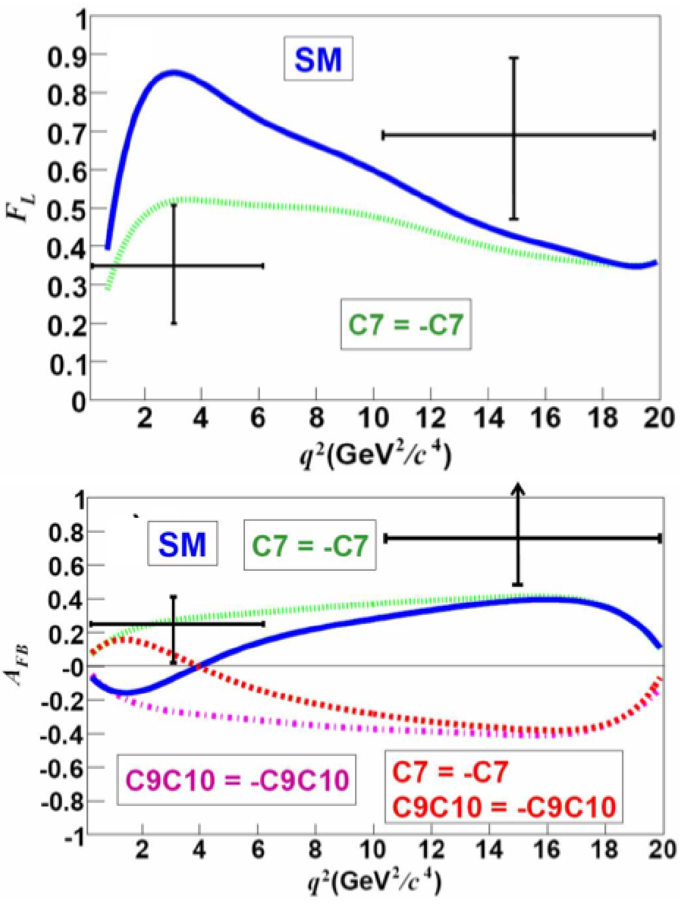

Figure 6.14: $F_L$ and $A_{FB}$ results and theoretical expectations.

The Run 6 analysis will measure $F_L$ and $A_{FB}$ again using the full BABAR dataset. With an increase in statistics, an improved event selection and a new fit technique it is hoped that the Run 6 analysis will measure $F_L$ and $A_{FB}$ in four bins of $q^2$.

# 7

# Run 6 Analysis

In this chapter the results for the Run 6 analysis will be presented. $F_L$ and $A_{FB}$ are measured in four bins of $q^2$: 0.10 - 4.00 GeV$^2/c^4$, 4.00 - 8.00 GeV$^2/c^4$, 10.24 - 12.96 GeV$^2/c^4$ and $>$14.06 GeV$^2/c^4$ using BABARs full dataset of 468 million $B\overline{B}$ pairs. The measurements will be made using both the 1D fits and the 2D fit techniques described in Chapter 4.

## 7.1 Results

### 7.1.1 Unblinding Strategy

The Run 6 analysis was unblinded in a similar way to the Run 5 analysis, the different stages are:

- The $B \rightarrow K^{*}l^{+}l^{-}$ signal yields were unblinded. Fit One - the $m_{ES}$ fits were performed in each $q^2$ bin and the number of signal and background events were compared to the expected number of events from Table 3.8.
- Fit Two - the 1D fit to $\cos\theta_{K^*}$ to extract $F_L$ was performed. For this fit to be classed as successful the fit must converge and the error on $F_L$ must meet the condition described in Section 5.2.3.

| $q^2$ bin | Fit $N_S(q^2)$ | Fit $N_B(q^2)$ |
|---|---|---|
| $q0$ | 21.9 ± 7.4 | 244.7 ± 16.6 |
| $q1$ | 28.8 ± 8.4 | 224.0 ± 16.1 |
| $q2$ | 31.1 ± 7.8 | 147.7 ± 13.1 |
| $q3$ | 25.9 ± 7.8 | 179.4 ± 14.6 |

Table 7.1: $B \rightarrow K^{*}l^{+}l^{-}$ observed number of signal and background yields.

- Fit Three and Four - the 1D fit to $\cos\theta_l$ to extract $A_{FB}$ and the 2D fit to $(\cos\theta_{K^*}, \cos\theta_l)$ to extract $F_L$ and $A_{FB}$ was performed. For these fits to be classed as successful they must pass the same requirements as Fit Two.

### 7.1.2 The $m_{ES}$ Fit Results

The signal and background yields are extracted from a fit to the $m_{ES}$ distribution in each $q^2$ bin. Table 7.1 shows the observed of events and Figure 7.1 shows the fits in each of the $q^2$ bins. The number of observed signal events was found to be consistent with the expected yields in Table 3.8.

### 7.1.3 The 1D fits - $F_L$ and $A_{FB}$ Result

The 1D fit to the $\cos\theta_{K^*}$ distribution of $B \rightarrow K^{*}l^{+}l^{-}$ to extract $F_L$ in each bin of $q^2$ are shown in Figure 7.2. The fits to extract $A_{FB}$ are shown in Figure 7.3. The fit results are listed in Table 7.2 with the statistical error and the final results with the statistical and systematic errors for the 1D fits will be presented in Section 7.3.

### 7.1.4 The 2D fit - $F_L$ and $A_{FB}$ Result

The projections of the 2D fit to the $(\cos\theta_{K^*}, \cos\theta_l)$ distribution of $B \rightarrow K^{*}l^{+}l^{-}$ to extract $F_L$ and $A_{FB}$ in each bin of $q^2$ are shown in Figures 7.4 and 7.5. The fit results with the statistical error are listed in Table 7.3 and the final results with

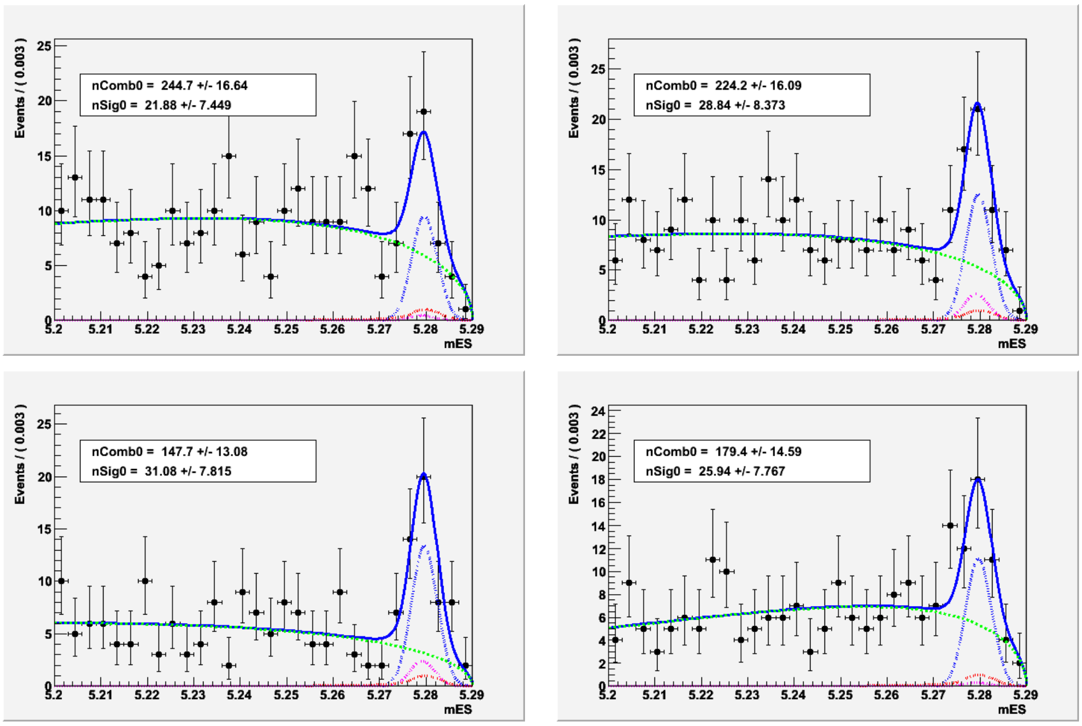

Figure 7.1: $B \rightarrow K^* l^+ l^-$ fit to $m_{ES}$ distribution. Top: $q0$ left, $q1$ right. Bottom: $q2$ left, $q3$ right. Total fit (solid blue), signal (dashed blue), random combinatoric (dashed green), inclusive crossfeed (dashed red), peaking backgrounds (dashed magenta).

| $q^2$ bin (GeV$^2/c^4$) | $F_L$ | $A_{FB}$ |
|---|---|---|
| $q0$ | $0.54 \pm 0.18$ | $-0.29 \pm 0.30$ |
| $q1$ | $0.68 \pm 0.20$ | $0.02 \pm 0.23$ |
| $q2$ | $0.70 \pm 0.18$ | $0.37 \pm 0.25$ |
| $q3$ | $0.26 \pm 0.24$ | $0.37 \pm 0.22$ |

Table 7.2: $B \rightarrow K^* l^+ l^-$ $F_L$ and $A_{FB}$ results from the 1D fits to $\cos\theta_{K*}$ and $\cos\theta_l$ with the statistical error.

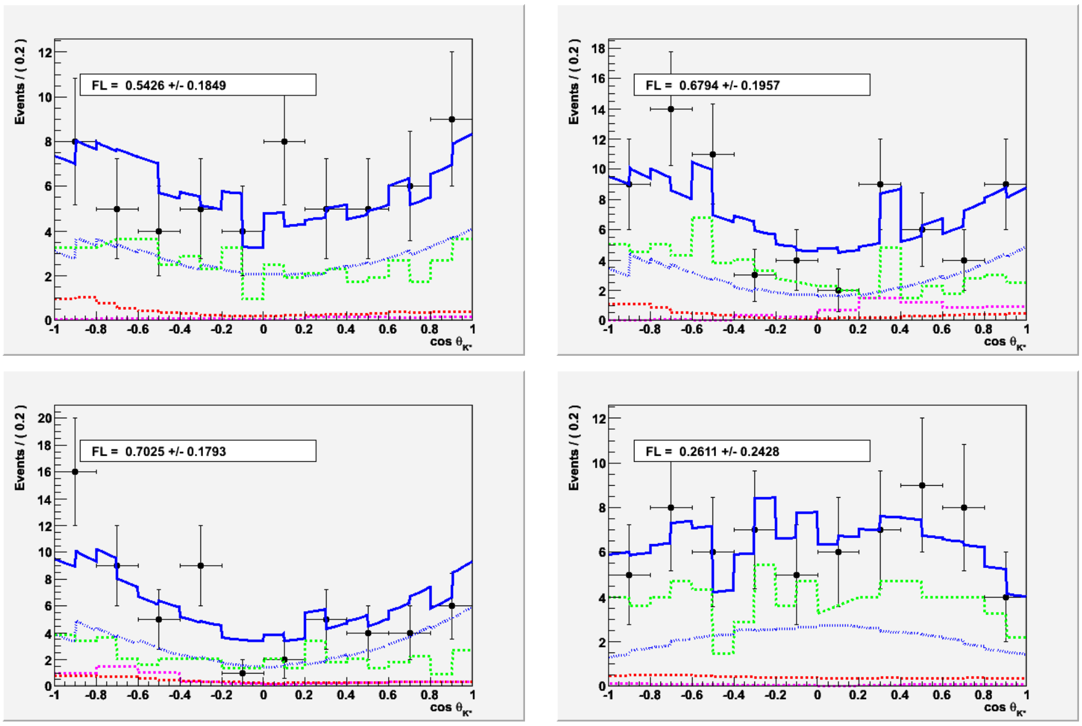

Figure 7.2: $B \rightarrow K^{*}l^{+}l^{-}$ 1D fit to $\cos\theta_{K*}$ distribution to extract $F_L$. Top: $q0$ left, $q1$ right. Bottom: $q2$ left, $q3$ right. Total fit (solid blue), signal (dashed blue), random combinatoric (dashed green), inclusive crossfeed (dashed red), peaking backgrounds (dashed magenta).

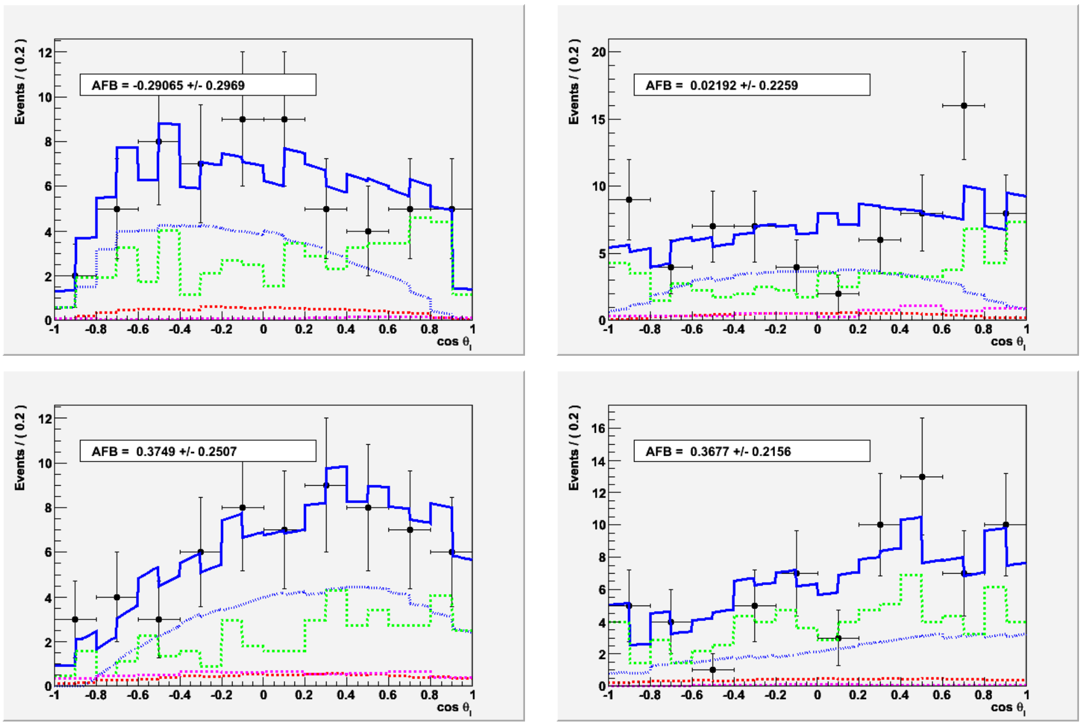

Figure 7.3: $B \to K^* l^+ l^-$ 1D fit to $\cos\theta_l$ distribution to extract $A_{FB}$. Top: $q0$ left, $q1$ right. Bottom: $q2$ left, $q3$ right. Total fit (solid blue), signal (dashed blue), random combinatoric (dashed green), inclusive crossfeed (dashed red), peaking backgrounds (dashed magenta).

| $q^2$ bin (GeV$^2/c^4$) | $F_L$ | $A_{FB}$ |
|---|---|---|
| $q0$ | $0.35 \pm 0.13$ | $-0.10 \pm 0.12$ |
| $q1$ | $0.37 \pm 0.13$ | $0.11 \pm 0.11$ |
| $q2$ | $0.32 \pm 0.10$ | $0.25 \pm 0.08$ |
| $q3$ | $0.22 \pm 0.11$ | $0.42 \pm 0.14$ |

Table 7.3: $B \to K^* l^+ l^-$ $F_L$ and $A_{FB}$ results from the 2D fit to $(\cos\theta_{K*}, \cos\theta_l)$ with statistical errors.

the statistical and systematic errors will be presented in Section 7.3.

## 7.2 Systematic Errors

The sources of systematic errors for the Run 6 analysis are predominantly the same as the Run 5 analysis listed in Section 6.3. The total systematic error for the 1D fits in each $q^2$ bin are shown in Tables 7.4 and 7.5 and for the 2D fit the systematic errors are in Tables 7.6 and 7.7.

The $m_{ES}$ fit yield error was found by studying both the signal and background components of the $m_{ES}$ fit. For the signal component the mean and sigma of the Gaussian was varied by $\pm 1\sigma$ and performing the 1D fits and the 2D fits. For the background component the Argus shape parameter was varied by $\pm 1\sigma$ and the fits were rerun. The average shift on the central values of $F_L$ and $A_{FB}$ relative to the original measured value is used as the systematic error.

The $F_L$ fit error only applies to the 1D fits and is found by rerunning the 1D $A_{FB}$ fit with the value of $F_L$ varied by $\pm 1\sigma$ to the original fit result. The average shift in the central value of $A_{FB}$ is used at the $F_L$ fit systematic.

The combinatoric background shape error is found by first studying different definitions of the $m_{ES}$ sideband. The combinatoric background shape in the fit is determined from the $m_{ES}$ region in data $5.20 < m_{ES} < 5.27$ GeV/$c^2$. Alternative definitions of the sideband region were used $5.23 < m_{ES} < 5.27$ GeV/$c^2$ and $5.20 < m_{ES} < 5.23$ GeV/$c^2$, the 1D fits and 2D fit were rerun. The second study involved reversing the BDT cut in Section 3.10, this increased

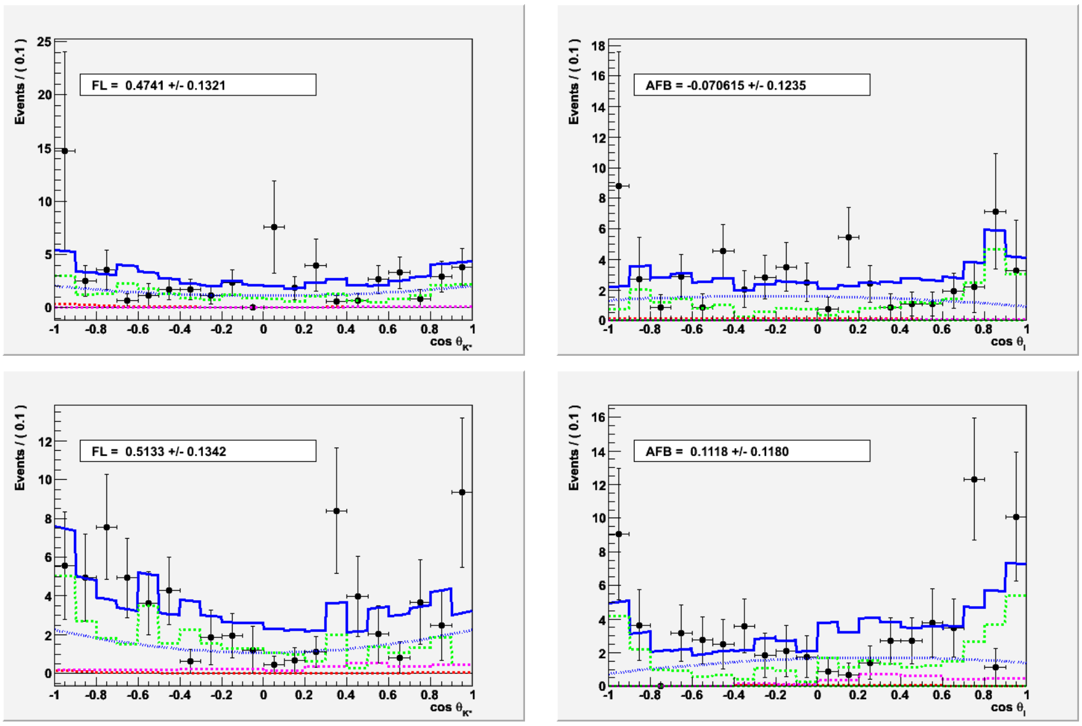

Figure 7.4: $B \to K^* l^+ l^-$ 1D projection of the 2D fit to the $(\cos\theta_{K*}, \cos\theta_l)$ distribution to extract $F_L$ and $A_{FB}$. Top: $q0$. Bottom: $q1$. Total fit (solid blue), signal (dashed blue), random combinatoric (dashed green), inclusive crossfeed (dashed red), peaking backgrounds (dashed magenta).

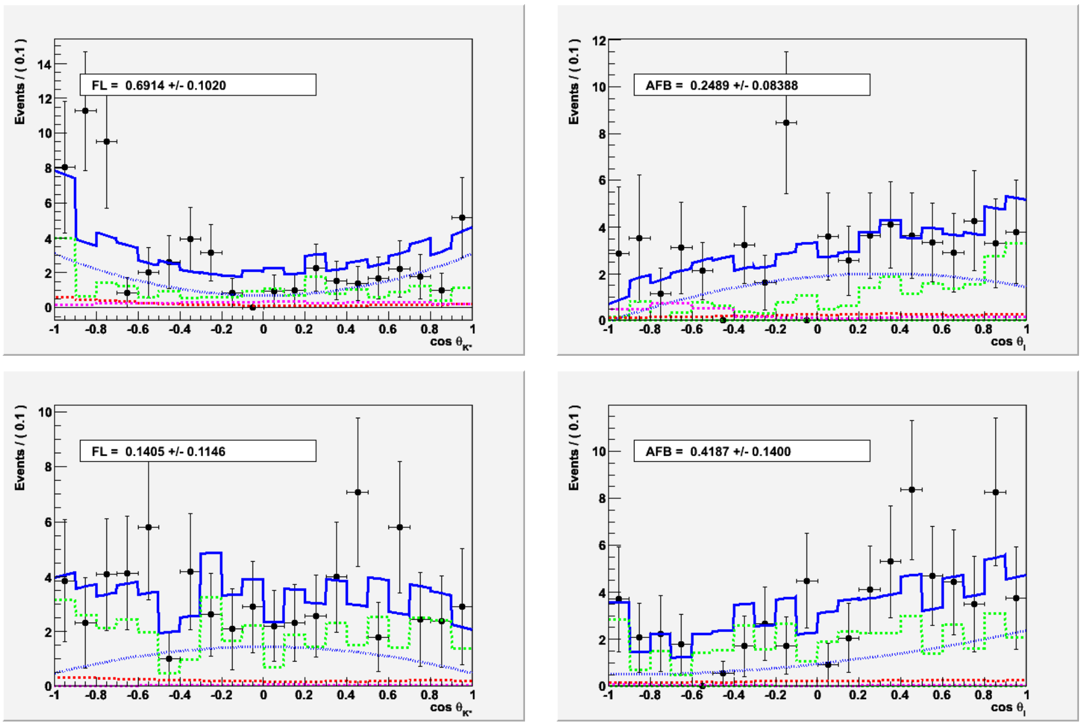

Figure 7.5: $B \rightarrow K^{*}l^{+}l^{-}$ 1D projection of the 2D fit to the $(\cos\theta_{K*}, \cos\theta_{l})$ distribution to extract $F_L$ and $A_{FB}$. Top: $q2$. Bottom: $q3$. Total fit (solid blue), signal (dashed blue), random combinatoric (dashed green), inclusive crossfeed (dashed red), peaking backgrounds (dashed magenta).

the number of combinatoric background events and produced a more precise background shape. The fits were rerun again in the $m_{ES}$ sideband region $5.20 < m_{ES} < 5.27$ GeV/$c^2$. It was found that the background shape from the events that failed the BDT cut was not a good model of the combinatoric background in the signal region, therefore the systematic error was taken to be the average shift on the central value from the different $m_{ES}$ sidebands.

The signal model error was obtained from the Run 5 analysis. The Run 5 analysis only made measurements in two bins of $q^2$ whereas the Run 6 analysis measured $F_L$ and $A_{FB}$ in four bins of $q^2$. Since the Wilson coefficients vary as a function of $q^2$, the Run 6 analysis will have a smaller error associated with the signal model, to be conservative the value from the Run 5 analysis will be used.

The fit bias systematic error was found by performing pure signal toys with the original fit values of $F_L$ and $A_{FB}$ used as input values for the toys. Then any deviation from a mean of zero will be multiplied by the statistical error and used to correct the fit values of $F_L$ and $A_{FB}$. This value will also be assigned as a systematic error.

The inclusive crossfeed shape error was found varying the normalisation of the crossfeed by $\pm 1\sigma$ and rerunning the 1D fits and the 2D fit. Any change in the central values with respect to the original fit results are used as the systematic.

The systematic associated with the efficiency histogram is found by performing the fits using histograms with a different number of bins. The original fit is performed using a 20x20 histogram, the fits were rerun using a 10x10 histogram and any shift in the central value was used as the systematic error.

### 7.2.1 Total Systematic Error

The total systematic error for the 1D fits are shown in Tables 7.4 and 7.5, for $A_{FB}$ and $F_L$ . The systematic errors from the 2D fit are listed in Tables 7.6 and 7.7, for $A_{FB}$ and $F_L$.

| Source of Error | $q0$ | $q1$ | $q2$ | $q3$ |
|---|---|---|---|---|
| $m_{ES}$ fit yields | 0.003 | 0.006 | 0.012 | 0.013 |
| $F_L$ fit error | 0.022 | 0.057 | 0.035 | 0.034 |
| Background shape | 0.029 | 0.020 | 0.076 | 0.051 |
| Signal model | 0.036 | 0.034 | 0.030 | 0.038 |
| Fit bias | 0.012 | 0.020 | 0.023 | 0.052 |
| Efficiency/cross-feed | 0.010 | 0.010 | 0.020 | 0.020 |
| Total | 0.054 | 0.073 | 0.095 | 0.092 |

Table 7.4: Total systematic errors for $A_{FB}$ for the 1D fits.

| Source of Error | $q0$ | $q1$ | $q2$ | $q3$ |
|---|---|---|---|---|
| $m_{ES}$ fit yields | 0.000 | 0.001 | 0.001 | 0.003 |
| Background shape | 0.001 | 0.045 | 0.051 | 0.058 |
| Signal model | 0.036 | 0.034 | 0.030 | 0.038 |
| Fit bias | 0.012 | 0.020 | 0.023 | 0.052 |
| Efficiency/cross-feed | 0.010 | 0.010 | 0.020 | 0.020 |
| Total | 0.039 | 0.061 | 0.067 | 0.089 |

Table 7.5: Total systematic errors for $F_L$ for the 1D fits.

## 7.3 Conclusion

This analysis produced the first measurement of $F_L$ and $A_{FB}$ in four $q^2$ bins using the full BABAR dataset. The 2D fit technique was used to model the $(\cos\theta_{K*}, \cos\theta_l)$ distribution for the first time. The final results for the 1D and 2D fits are listed in Tables 7.8 and 7.9, respectively. In $q0$ the 1D fit result was $A_{FB} = -0.29 \pm 0.30 \pm 0.05$ and $F_L = 0.54 \pm 0.18 \pm 0.04$, and the 2D fit result was $A_{FB} = -0.09 \pm 0.12 \pm 0.04$ and $F_L = 0.35 \pm 0.13 \pm 0.08$, where the first error is statistical and the second is systematic. The expected SM values of $A_{FB}$ and $F_L$ in that bin are $A_{FB} = -0.10$ and $F_L = 0.57$. The measured values are consistent with the SM and with a zero-crossing in $A_{FB}$, however, the Run 5 analysis measured a positive $A_{FB}$ in this $q^2$ region.

In the $q1$ bin the 1D fits measured $A_{FB} = 0.02 \pm 0.23 \pm 0.07$ and $F_L = 0.68 \pm 0.20 \pm 0.06$ and for the 2D fits $A_{FB} = 0.07 \pm 0.11 \pm 0.05$ and $F_L = 0.37 \pm 0.13 \pm 0.08$. The SM expected values are $A_{FB} = 0.15$ and $F_L = 0.68$.

| Source of Error | $q0$ | $q1$ | $q2$ | $q3$ |
|---|---|---|---|---|
| $m_{ES}$ fit yields | 0.000 | 0.001 | 0.000 | 0.001 |
| Background shape | 0.009 | 0.018 | 0.018 | 0.022 |
| Signal model | 0.036 | 0.034 | 0.030 | 0.038 |
| Fit bias | 0.003 | 0.009 | 0.032 | 0.020 |
| Efficiency/cross-feed | 0.010 | 0.028 | 0.020 | 0.017 |
| Total | 0.039 | 0.048 | 0.044 | 0.051 |

Table 7.6: Total systematic errors for $A_{FB}$ for the 2D fit.

| Source of Error | $q0$ | $q1$ | $q2$ | $q3$ |
|---|---|---|---|---|
| $m_{ES}$ fit yields | 0.000 | 0.001 | 0.000 | 0.001 |
| Background shape | 0.022 | 0.014 | 0.011 | 0.047 |
| Signal model | 0.036 | 0.034 | 0.030 | 0.038 |
| Fit bias | 0.014 | 0.015 | 0.029 | 0.012 |
| Efficiency/cross-feed | 0.063 | 0.064 | 0.015 | 0.020 |
| Total | 0.077 | 0.075 | 0.046 | 0.065 |

Table 7.7: Total systematic errors for $F_L$ for the 2D fit.

| $q^2$ bin (GeV$^2/c^4$) | $F_L$ | $A_{FB}$ |
|---|---|---|
| $q0$ | $0.54 \pm 0.18 \pm 0.04$ | $-0.29 \pm 0.30 \pm 0.05$ |
| $q1$ | $0.68 \pm 0.20 \pm 0.06$ | $0.02 \pm 0.23 \pm 0.07$ |
| $q2$ | $0.70 \pm 0.18 \pm 0.07$ | $0.37 \pm 0.25 \pm 0.10$ |
| $q3$ | $0.26 \pm 0.24 \pm 0.09$ | $0.37 \pm 0.22 \pm 0.09$ |

Table 7.8: $B \rightarrow K^* l^+ l^-$ $F_L$ and $A_{FB}$ results from the 1D fits to $\cos\theta_{K*}$ and $\cos\theta_l$.

| $q^2$ bin (GeV$^2/c^4$) | $F_L$ | $A_{FB}$ |
|---|---|---|
| $q0$ | $0.46 \pm 0.13 \pm 0.08$ | $-0.07 \pm 0.12 \pm 0.04$ |
| $q1$ | $0.49 \pm 0.13 \pm 0.08$ | $0.10 \pm 0.11 \pm 0.05$ |
| $q2$ | $0.66 \pm 0.10 \pm 0.05$ | $0.22 \pm 0.08 \pm 0.04$ |
| $q3$ | $0.15 \pm 0.11 \pm 0.07$ | $0.40 \pm 0.14 \pm 0.05$ |

Table 7.9: $B \rightarrow K^* l^+ l^-$ $F_L$ and $A_{FB}$ results from the 2D fit to $(\cos\theta_{K*}, \cos\theta_l)$.

In the $q2$ bin the 1D fits result was $A_{FB} = 0.37 \pm 0.25 \pm 0.10$ and $F_L = 0.70 \pm 0.18 \pm 0.07$ and for the 2D fit $A_{FB} = 0.12 \pm 0.08 \pm 0.04$ and $F_L = 0.32 \pm 0.10 \pm 0.05$. The SM expected result was $A_{FB} = 0.38$ and $F_L = 0.45$.

In the $q3$ bin the 1D fits measured $A_{FB} = 0.37 \pm 0.22 \pm 0.09$ and $F_L = 0.26 \pm 0.24 \pm 0.09$ and the 2D fit obtained $A_{FB} = 0.33 \pm 0.14 \pm 0.05$ and $F_L = 0.22 \pm 0.11 \pm 0.07$. The SM values for $A_{FB}$ and $F_L$ are $A_{FB} = 0.36$ and $F_L = 0.39$. In all $q^2$ bins there is good agreement between the SM and the $A_{FB}$ results. The results for $F_L$ are also consistent with the SM, however, a much larger $B \rightarrow K^* l^+ l^-$ sample would be required to precisely test the SM.

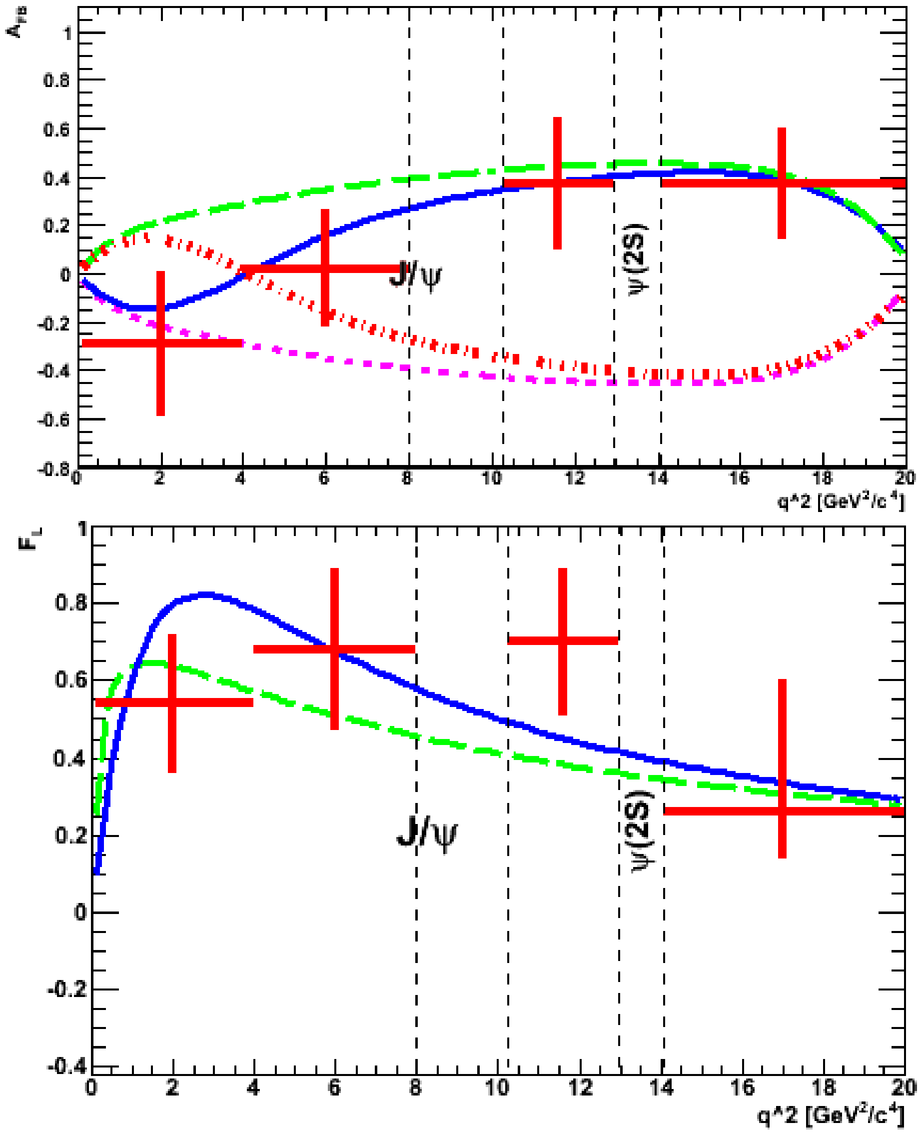

Figure 7.6: $A_{FB}$ and $F_L$ results from the 1D fits as a function of $q^2$ for the Run 6 analysis. SM (blue), $C_7 = -C_7(SM)$ (green), $C_9C_{10} = -C_9C_{10}(SM)$ (magenta) and $C_7 = -C_7(SM), C_9C_{10} = -C_9C_{10}(SM)$ (red).

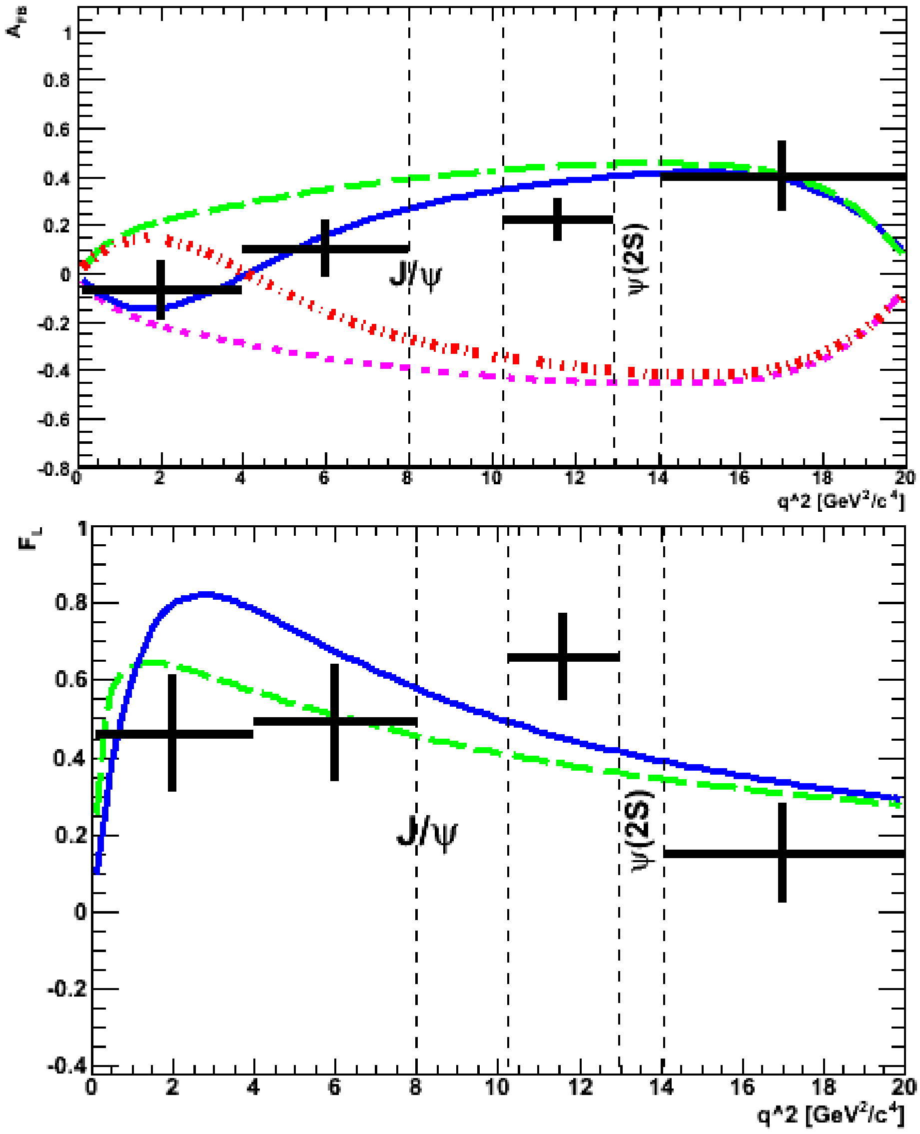

Figure 7.7: $A_{FB}$ and $F_L$ results from the 2D fits as a function of $q^2$ for the Run 6 analysis. SM (blue), $C_7 = -C_7(SM)$ (green), $C_9C_{10} = -C_9C_{10}(SM)$ (magenta) and $C_7 = -C_7(SM), C_9C_{10} = -C_9C_{10}(SM)$ (red).

# 8

# Conclusion

## 8.1 Summary of Run 5 and Run 6 Analyses

This thesis presented two analyses that measured $F_L$ and $A_{FB}$. The Run 5 analysis made measurements in two $q^2$ regions, 0.1< $q^2$ < 6.5 GeV$^2/c^4$ and $q^2 >$ 10.24 GeV$^2/c^4$, using a dataset of 384 million $B\overline{B}$ pairs collected by the BABAR detector. In this analysis two one-dimensional fits to $\cos\theta_{K^*}$ and $\cos\theta_l$ were performed in order to extract $F_L$ and $A_{FB}$. The results in both $q^2$ regions are consistent with the SM. The Run 5 analysis was published in PRL in 2009 [86].

The Run 6 analyses made measurements using using BABAR's full $\Upsilon(4S)$ dataset of 468 million $B\overline{B}$ pairs in four regions of $q^2$: 0.10 - 4.00 GeV$^2/c^4$, 4.00 - 8.00 GeV$^2/c^4$, 10.24 - 12.96 GeV$^2/c^4$ and >14.06 GeV$^2/c^4$. In this analysis two different fitting techniques were used to extract $F_L$ and $A_{FB}$. The two one- dimensional fits to $\cos\theta_{K^*}$ and $\cos\theta_l$ from the Run 5 analysis were used and in addition a two-dimensional fit to ($\cos\theta_{K^*}, \cos\theta_l$) was also developed. This thesis presents the first measurement of $F_L$ and $A_{FB}$ using the two-dimensional fitting technique. Figure 8.1 shows the comparison of the Run 5 and Run 6 analysis for the one-dimensional fitting technique. The larger dataset enabled the Run 6 analysis to measure $F_L$ and $A_{FB}$ in twice as many $q^2$ as the Run 5 analysis. Figure 8.2 shows the Run 6 comparison between the one-dimensional and two-dimensional fitting techniques. The error on the two-dimensional fit

| $q^2$ bin (GeV$^2/c^4$) | $F_L$ | $A_{FB}$ |
|---|---|---|
| 0.00-2.00 | $0.29^{+0.21}_{-0.18} \pm 0.02$ | $0.47^{+0.26}_{-0.32} \pm 0.03$ |
| 2.00-4.30 | $0.71^{+0.24}_{-0.24} \pm 0.05$ | $0.11^{+0.31}_{-0.36} \pm 0.07$ |
| 4.30-8.68 | $0.64^{+0.23}_{-0.24} \pm 0.07$ | $0.45^{+0.15}_{-0.21} \pm 0.15$ |
| 10.09-12.86 | $0.17^{+0.17}_{-0.15} \pm 0.03$ | $0.43^{+0.18}_{-0.20} \pm 0.03$ |
| 14.18-16.00 | $-0.15^{+0.27}_{-0.23} \pm 0.07$ | $0.70^{+0.16}_{-0.22} \pm 0.10$ |
| $> 16.00$ | $0.12^{+0.15}_{-0.13} \pm 0.02$ | $0.66^{+0.11}_{-0.15} \pm 0.04$ |

Table 8.1: $B \rightarrow K^*l^+l^-$ $F_L$ and $A_{FB}$ results from Belle with a dataset of 657 million $B\overline{B}$.

is at least ~20% smaller in each $q^2$ bin than the one-dimensional fits. The improvement is pivotal for maximising the physics potential of this statistically challenged analysis.

## 8.2 Comparison with Current Experimental Measurements

The Belle Collaboration measured $F_L$ and $A_{FB}$ in six bins of $q^2$ using a dataset of 657 million $B\overline{B}$ pairs [87]. They observed that the $A_{FB}$ distribution was positively shifted in this region, however, within the large statistical error all results are consistent with the SM. The Belle results are shown in Figure 8.3 and Table 8.1 lists the results. Figure 8.4 shows the Run 6 results with the Belle results for comparison.

The CDF Collaboration measured $F_L$ and $A_{FB}$ in six bins of $q^2$ using a dataset of 4.4 fb$^{-1}$ [88]. They have a very large statistical error at low $q^2$ therefore no strong conclusions can be drawn. The CDF results are shown in Figure 8.5 and Table 8.2 lists the results. The final results from the Run 6 analysis are plotted in Figure 8.2 as a function of $q^2$ with the SM, $C_7 = -C_7(SM)$, $C_9C_{10} = -C_9C_{10}(SM)$ and $C_7 = -C_7(SM), C_9C_{10} = -C_9C_{10}(SM)$ predictions. Figure 8.6 shows the Run 6 results with the CDF results for comparison.

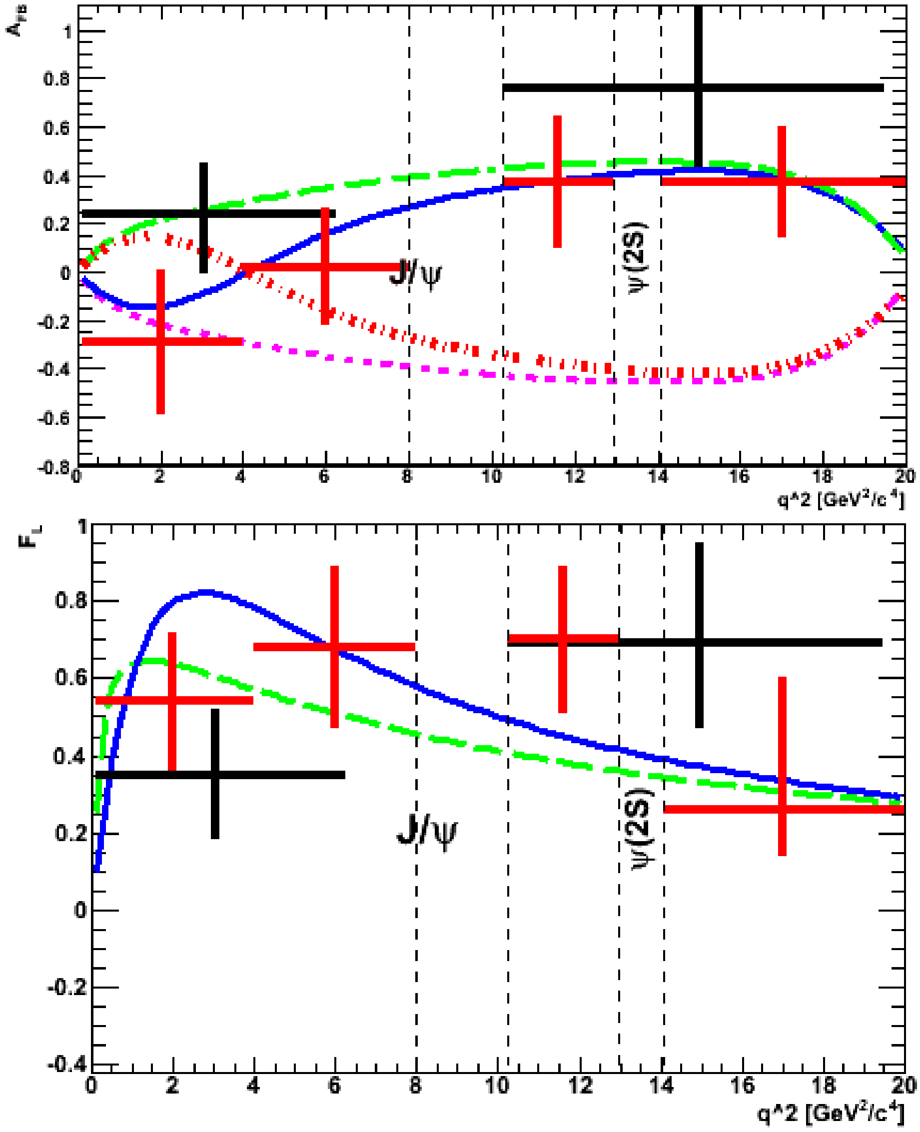

Figure 8.1: Comparison of Run 5 and Run 6 $A_{FB}$ and $F_L$ results as a function of $q^2$ for the 1D fitting technique. SM (blue), $C_7 = -C_7(SM)$ (green), $C_9C_{10} = -C_9C_{10}(SM)$ (magenta) and $C_7 = -C_7(SM), C_9C_{10} = -C_9C_{10}(SM)$ (red). The red points are the Run 5 result and the black points are the Run 6 result.

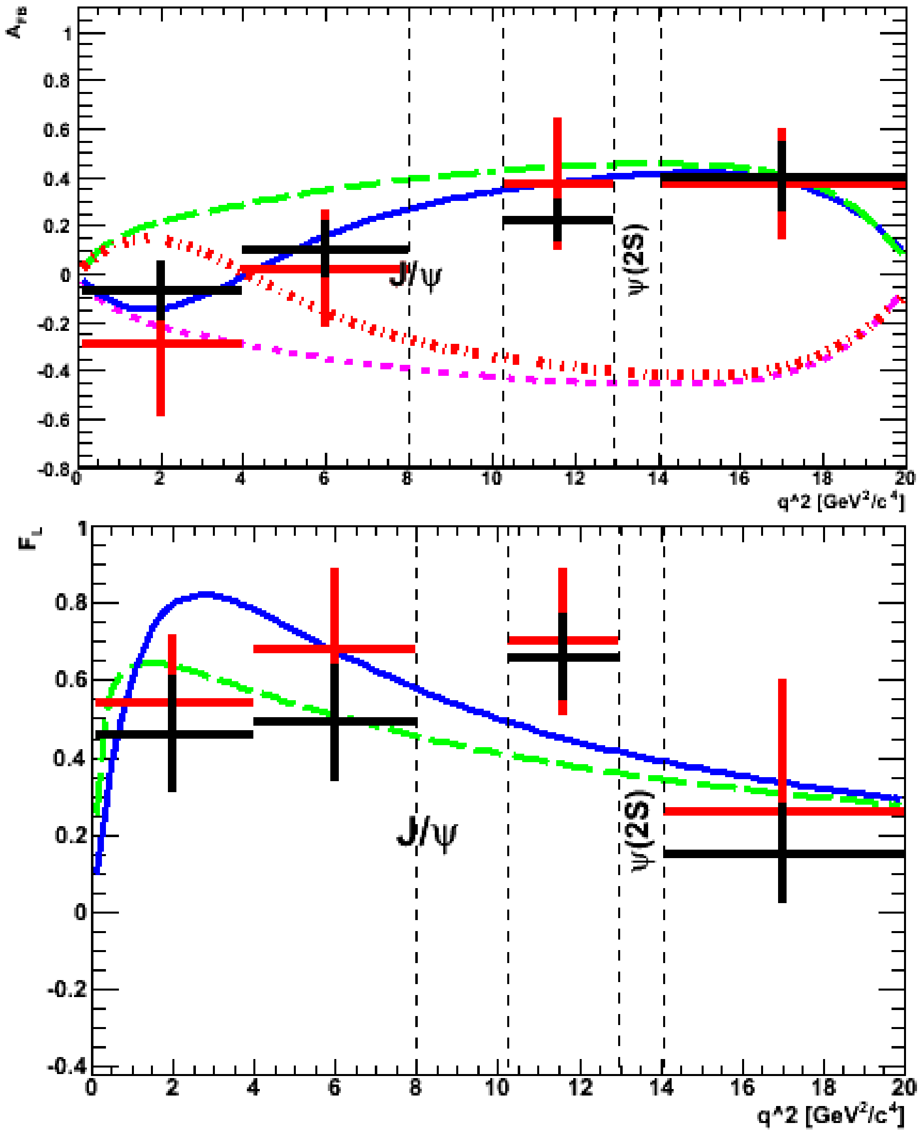

Figure 8.2: Comparison of 1D and 2D $A_{FB}$ and $F_L$ results as a function of $q^2$ for the Run 6 analysis. SM (blue), $C_7 = -C_7(SM)$ (green), $C_9C_{10} = -C_9C_{10}(SM)$ (magenta) and $C_7 = -C_7(SM), C_9C_{10} = -C_9C_{10}(SM)$ (red). The red points are the 1D fit result and the black points are the 2D fit result.

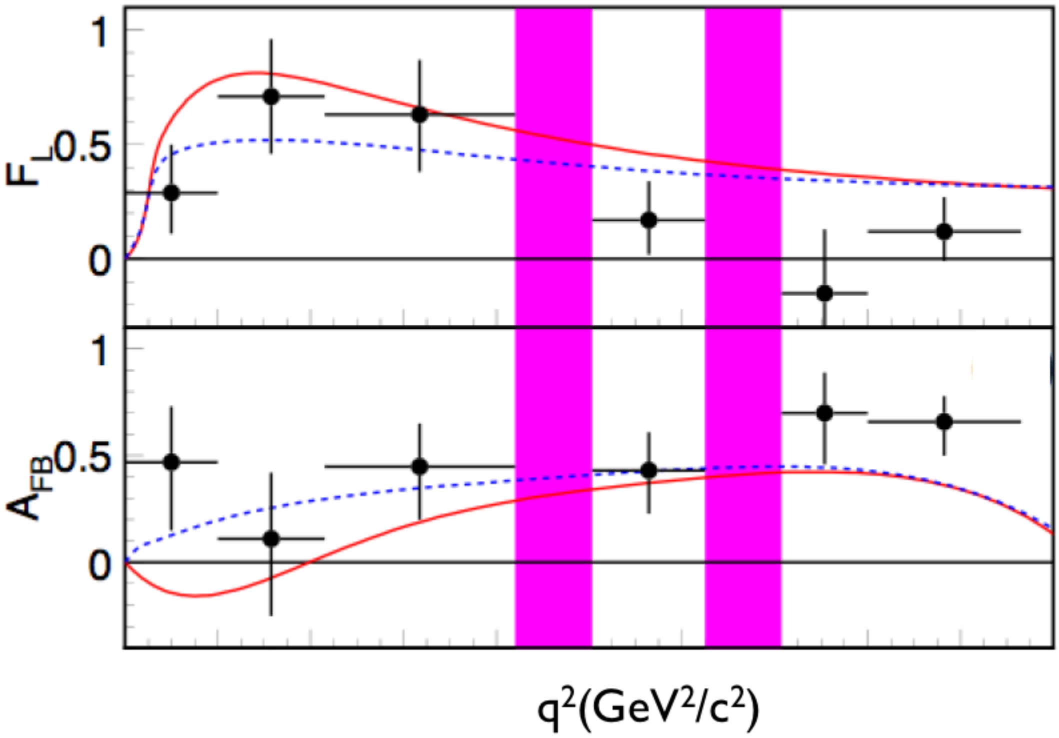

Figure 8.3: $F_L$ and $A_{FB}$ results as a function of $q^2$ from Belle. The solid red line is the SM expectation and the dashed line is for $C_7 = -C_7^{SM}$.

| $q^2$ bin (GeV$^2/c^4$) | $F_L$ | $A_{FB}$ |
|---|---|---|
| 0.00-2.00 | $0.53^{+0.32}_{-0.34} \pm 0.07$ | $0.13^{+1.65}_{-0.75} \pm 0.25$ |
| 2.00-4.30 | $0.40^{+0.32}_{-0.33} \pm 0.08$ | $0.19^{+0.40}_{-0.41} \pm 0.14$ |
| 4.30-8.68 | $0.82^{+0.19}_{-0.23} \pm 0.07$ | $-0.06^{+0.30}_{-0.28} \pm 0.05$ |
| 10.09-12.86 | $0.31^{+0.19}_{-0.18} \pm 0.02$ | $0.66^{+0.23}_{-0.20} \pm 0.07$ |
| 14.18-16.00 | $0.55^{+0.17}_{-0.18} \pm 0.02$ | $0.42^{+0.16}_{-0.16} \pm 0.09$ |
| $> 16.00$ | $0.09^{+0.18}_{-0.14} \pm 0.03$ | $0.70^{+0.16}_{-0.25} \pm 0.10$ |

Table 8.2: $B \to K^* l^+ l^-$ $F_L$ and $A_{FB}$ results from CDF with a dataset of 4.4 fb$^{-1}$.

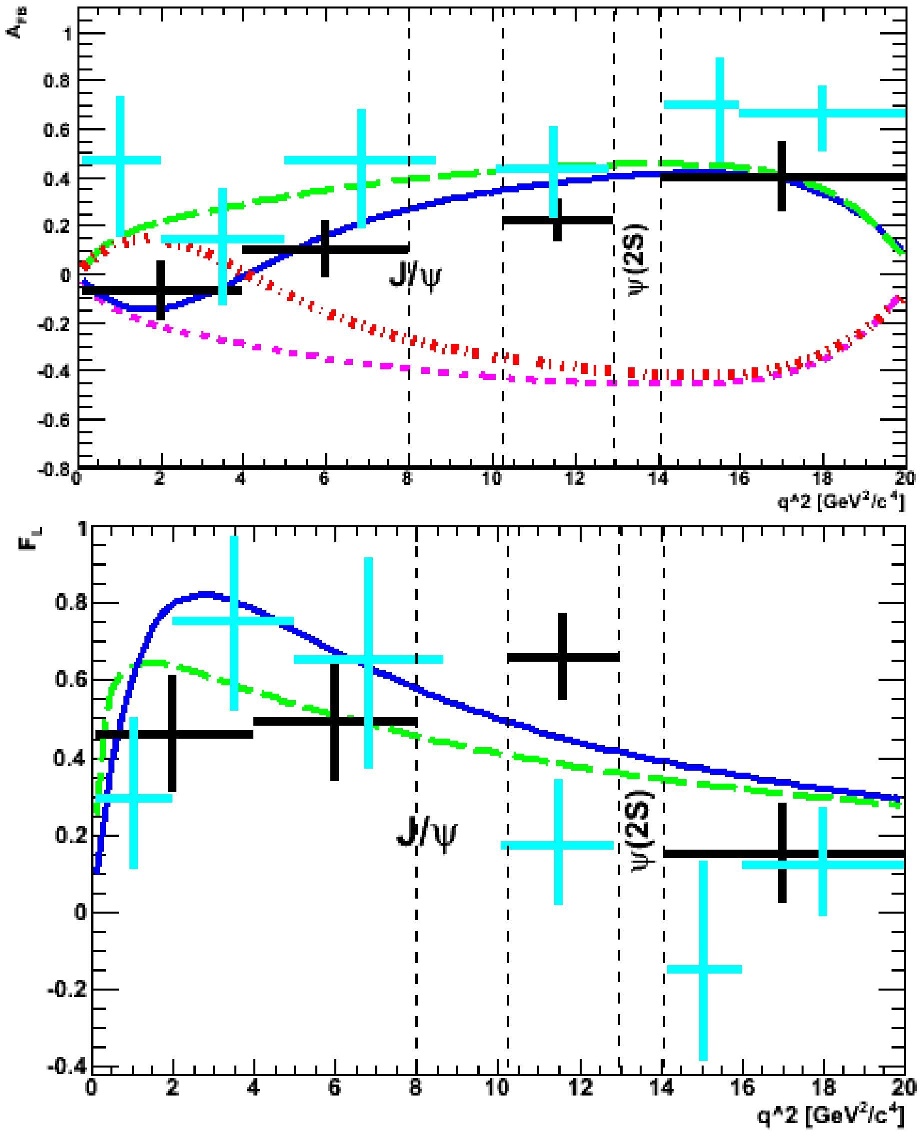

Figure 8.4: $A_{FB}$ and $F_L$ results as a function of $q^2$ for the Run 6 analysis and the Belle result. SM (blue), $C_7 = -C_7(SM)$ (green), $C_9C_{10} = -C_9C_{10}(SM)$ (magenta) and $C_7 = -C_7(SM), C_9C_{10} = -C_9C_{10}(SM)$ (red). The black points are the Run 6 result and the blue points are the results from Belle.

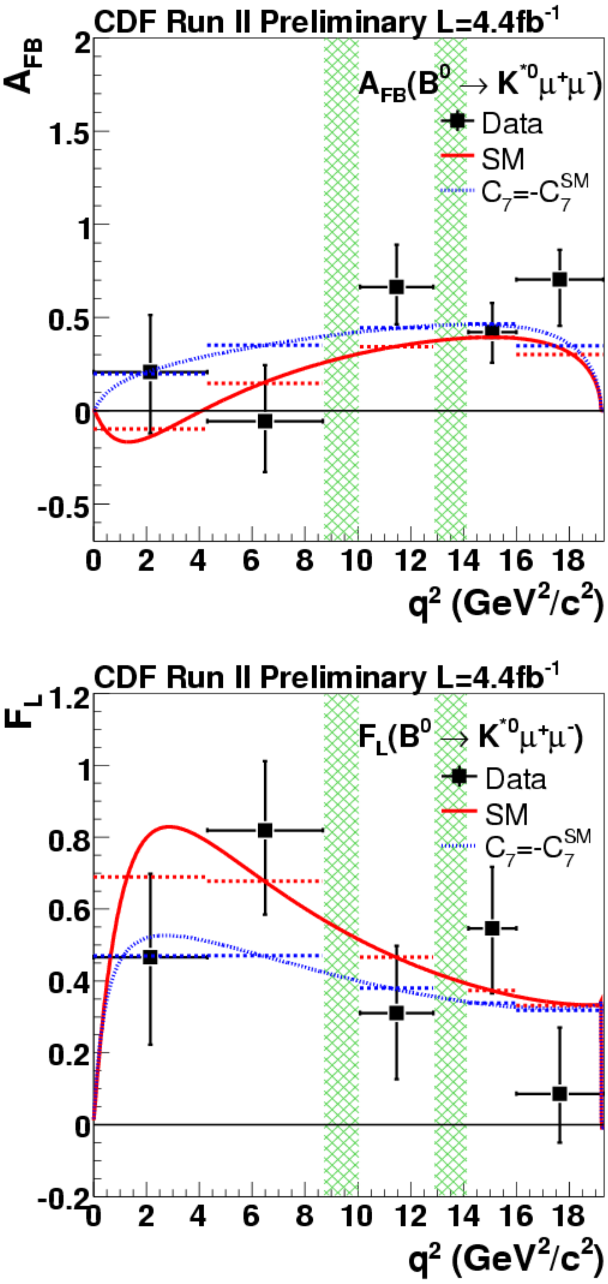

Figure 8.5: $F_L$ and $A_{FB}$ results as a function of $q^2$ from CDF. The solid red line is the SM expectation and the dashed line is for $C_7 = -C_7^{SM}$.

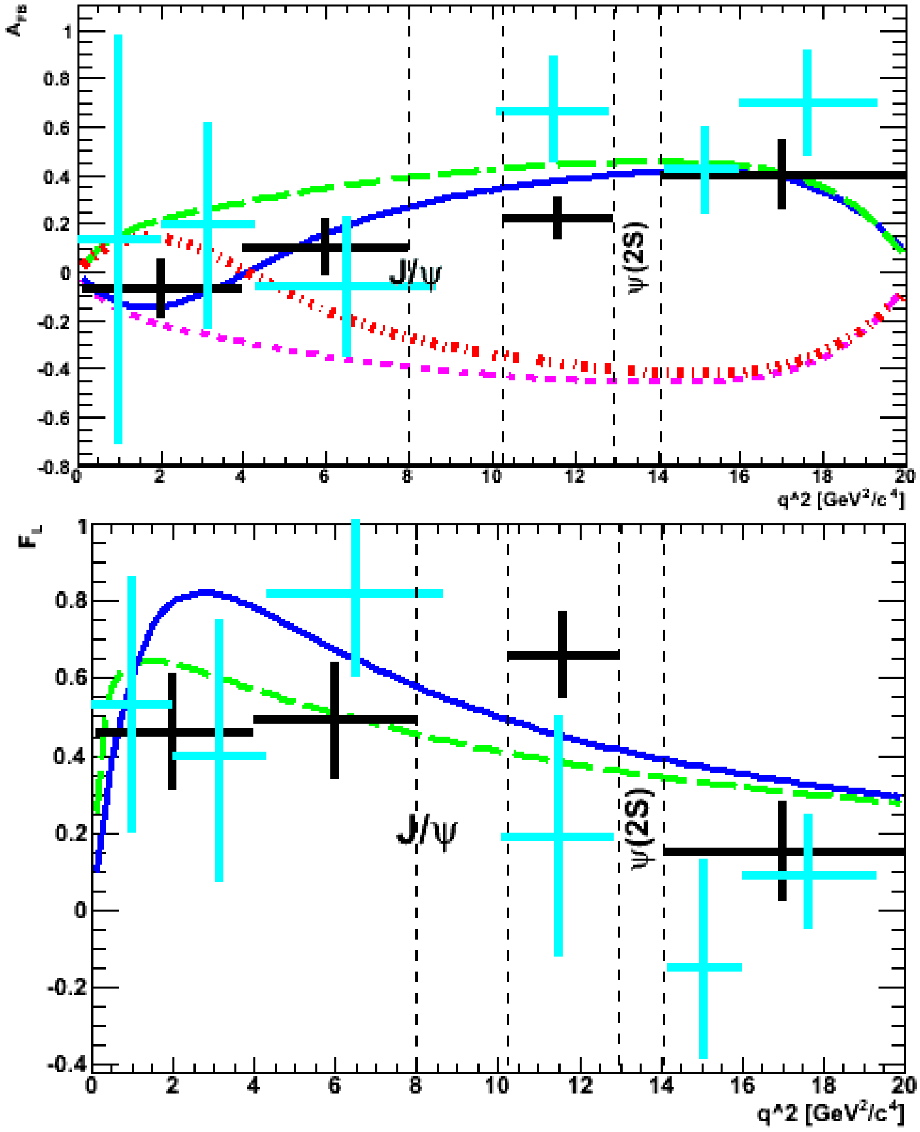

Figure 8.6: $A_{FB}$ and $F_L$ results as a function of $q^2$ for the Run 6 analysis and the CDF result. SM (blue), $C_7 = -C_7(SM)$ (green), $C_9C_{10} = -C_9C_{10}(SM)$ (magenta) and $C_7 = -C_7(SM), C_9C_{10} = -C_9C_{10}(SM)$ (red). The black points are the Run 6 result and the blue points are the results from CDF.

## 8.3 Future Work at *BABAR*

The angular analysis of $B \to K^{(*)}l^+l^-$ has provided an excellent probe to search for NP and there are many more topics still to be studied at *BABAR*.

### 8.3.1 The $\phi$ Fit

$\phi$ is the angle between the $K^*$ and the di-lepton decay planes. In Section 1.3.2 it was found that by integrating over $\cos\theta_{K^*}$ and $\cos\theta_l$ the angular distribution for $\phi$ was found to be:

$$\frac{d\Gamma}{d\phi} \propto (|A_0|^2 + |A_\perp|^2 + |A_\parallel|^2) - Re(A_\parallel A_\perp^*)\cos 2\phi - Im(A_\parallel A_\perp^*)\sin 2\phi$$

and can be simplified to:

$$\frac{1}{\Gamma}\frac{d\Gamma}{d\phi} \propto A + B\cos 2\phi.$$

It was noted that in the SM $C_{7R}$ is predicted to be small therefore leading to a flat distribution at low $q^2$. At high $q^2$ the $\cos 2\phi$ term becomes significant due to the $C_9$ and $C_{10}$ contributions. Therefore, fitting the $\phi$ distribution can be used as a search for NP.

### 8.3.2 $B \to K^+l^+l^-$ $A_{FB}$ measurement

The fit to extract $A_{FB}$ from $B \to K^+l^+l^-$ was performed in the Run 5 analysis but it was not carried out in the Run 6 analysis. This is an interesting measurement that fell outside the scope of this thesis, however it will be measured at a later date.

## 8.4 The LHC and Beyond

### 8.4.1 The LHCb Experiment

The LHCb experiment is a dedicated B-physics experiment that is expected to match the B-factories statistics in $B \to K^{*}\mu^{+}\mu^{-}$ events [89] by August 2010. From Equation 1.3.4, the full angular distribution is described in terms of twelve angular coefficients. There are many angular observables in addition to $F_L$ and $A_{FB}$ that can be constructed and will be sensitive to one or more of the Wilson coefficients. By measuring the full set of angular observables as a function of dilepton mass squared, $q^2$, the value of the Wilson coefficients can be constrained further.

The most precisely predicted feature for the SM decay of $B \to K^{*}\mu^{+}\mu^{-}$ is the presence of a "zero-crossing" in the $A_{FB}$ distribution at $q^2$ = 4 GeV$^2/c^4$. It is expected that within one nominal year of running at the design luminosity of $5 \times 10^{32}$ cm$^{-2}s^{-1}$, ∼2 fb$^{-1}$ of data will have been collected and the "zero-crossing" for $A_{FB}$ can be extracted to an accuracy of ∼10%.

Lastly at the LHCb experiment, it is predicted that with a dataset of ∼10 fb$^{-1}$ the full angular analysis can be studied to obtain more complete information on the transversity amplitudes.

### 8.4.2 The ATLAS and CMS Experiments

The primary goal of the ATLAS and CMS experiments is to investigate the origin of matter in the universe, however, they are general purpose detectors and have the ability to detect the decay $B \to K^{*}\mu^{+}\mu^{-}$. After three years of low luminosity running of 30 fb$^{-1}$, ATLAS expects to have collected approximately 2000 $B_d^0 \to K^{*}\mu^{+}\mu^{-}$ signal events [90]. With a data sample of this size, $A_{FB}$ can be extracted with an accuracy of ∼5%. The CMS experiment is expected to obtain a similar level of precision [91].

### 8.4.3 SuperB Factory

The SuperB Factory [92] is expected to come into operation in the first half of the next decade and will have a peak luminosity in excess of $10^{36}$ cm$^{-2}s^{-1}$ at the $\Upsilon(4S)$ resonance. The SuperB factory will be an essential partner to the LHC in understanding potential NP observations. It also has the ability to access extremely rare decays that are undetectable at the LHC. The $A_{FB}$ for $B \to K^{*}l^{*}l^{-}$ is expected to be measured to a precision of 9% with 75 ab$^{-1}$ of data. Although the LHC experiments have the ability to precisely measure $B^0 \to K^{*0}\mu^+\mu^-$, the SuperB Factory will also have the ability to measure the equivalent mode with $e^+e^-$ pairs, the corresponding mode for charged decays and the inclusive channel $b \to sl^+l^-$.

## 8.5 Conclusion

The first measurement of $A_{FB}$ from BABAR, Belle and CDF caused a lot of excitement in the scientific community due to the indication that the zero-crossing point might not exist, therefore hinting at a NP contribution. The Run 5 analysis presented in this thesis, using the 1D fit strategy, also suggested the SM zero-crossing point did not exist. However, the results from the Run 6 analysis presented in this thesis, for both the 1D fits and the 2D fit, are consistent with the SM zero-cossing point at 4.2 $\pm$ 0.6 GeV$^2/c^4$. At present, it is impossible to draw any strong conclusions about the underlying physics model from the $F_L$ and $A_{FB}$ distributions due to the large statistical error. However, with the LHC in operation and the planned SuperB Factory, $B \to K^{*}l^{+}l^{-}$ is a key analysis that will play a leading role in the search for NP over the next decade.

# Appendix

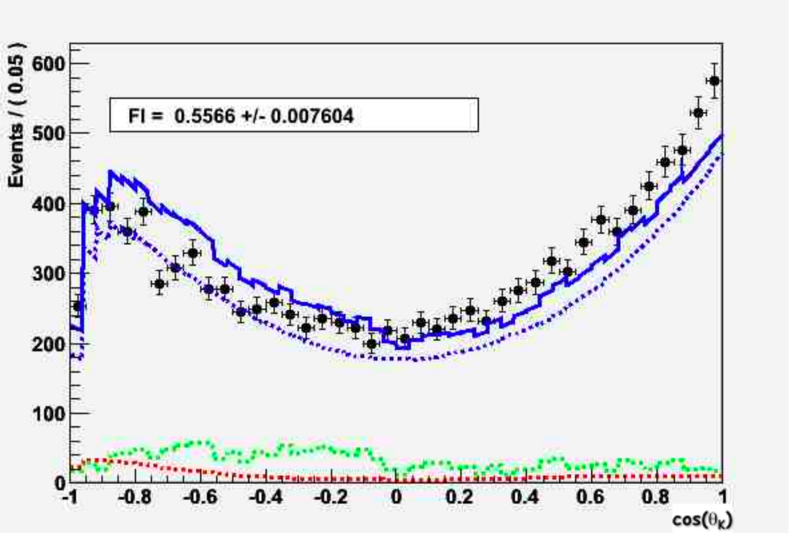

Figure 8.7: Fit to $F_L$ for the $B \to J/\Psi K^*$ combined dataset. Total fit (solid blue line), signal (dashed blue), combinatoric background (dashed green), total crossfeed (dashed red).

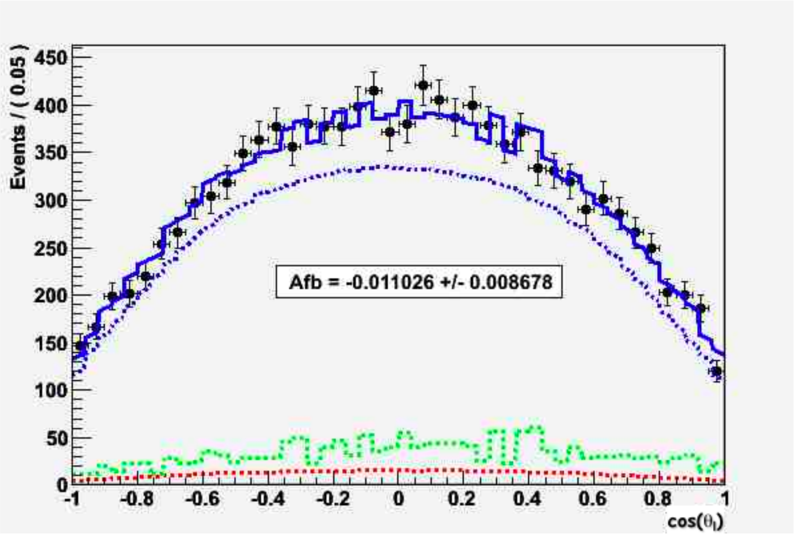

Figure 8.8: Fit to $A_{FB}$ for the $B \to J/\Psi K^*$ combined dataset. Total fit (solid blue line), signal (dashed blue), combinatoric background (dashed green), total crossfeed (dashed red).

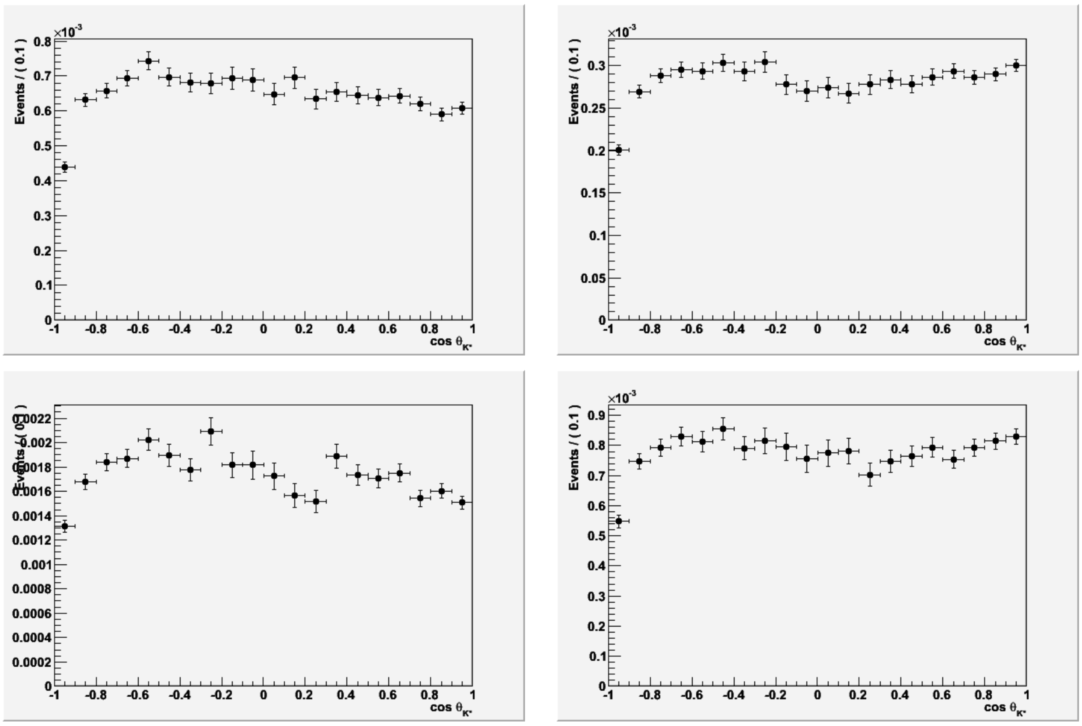

Figure 8.9: One dimensional projection of $B \to K^{*} l^{+} l^{-}$ efficiency for $\cos\theta_{K^{*}}$ for each of the modes in $q0$. Top: $B^{+} \to K_{s}^{0}\pi^{+}\mu^{+}\mu^{-}$ (left), $B^{0} \to K^{+}\pi^{-}\mu^{+}\mu^{-}$ (right). Bottom: $B^{+} \to K_{s}^{0}\pi^{+}e^{+}e^{-}$ (left), $B^{0} \to K^{+}\pi^{-}e^{+}e^{-}$ (right).

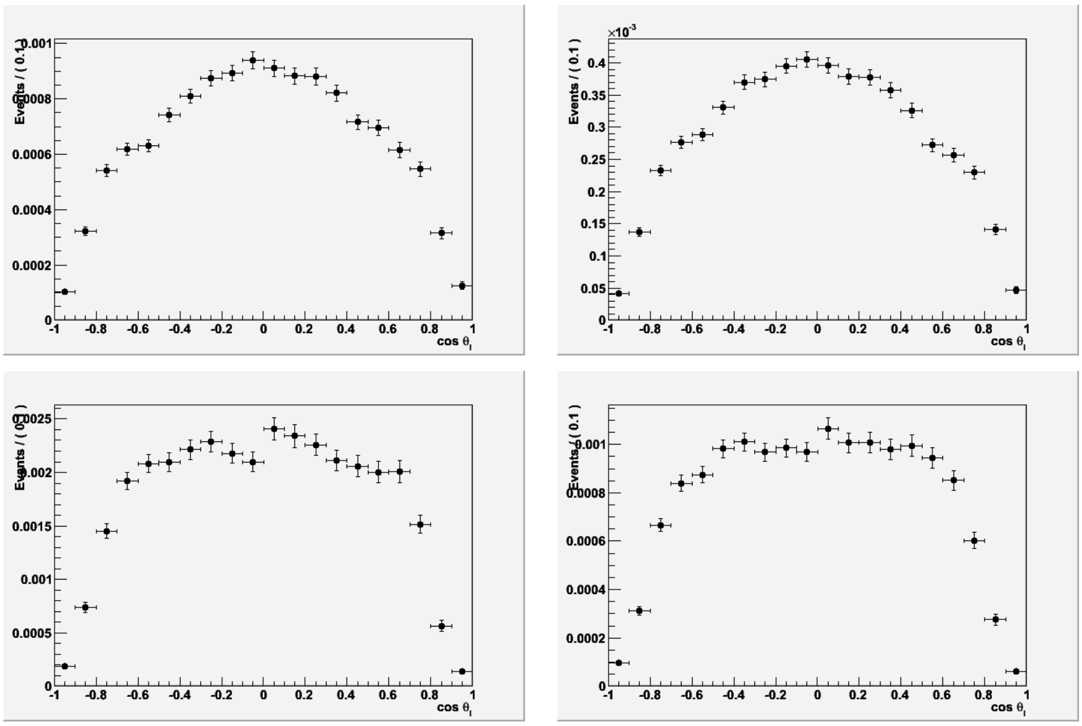

Figure 8.10: One dimensional projection of $B \to K^{*}l^{+}l^{-}$ efficiency for $\cos\theta_l$ for each of the modes in $q0$. Top: $B^{+} \to K_s^{0}\pi^{+}\mu^{+}\mu^{-}$ (left), $B^{0} \to K^{+}\pi^{-}\mu^{+}\mu^{-}$ (right). Bottom: $B^{+} \to K_s^{0}\pi^{+}e^{+}e^{-}$ (left), $B^{0} \to K^{+}\pi^{-}e^{+}e^{-}$ (right).

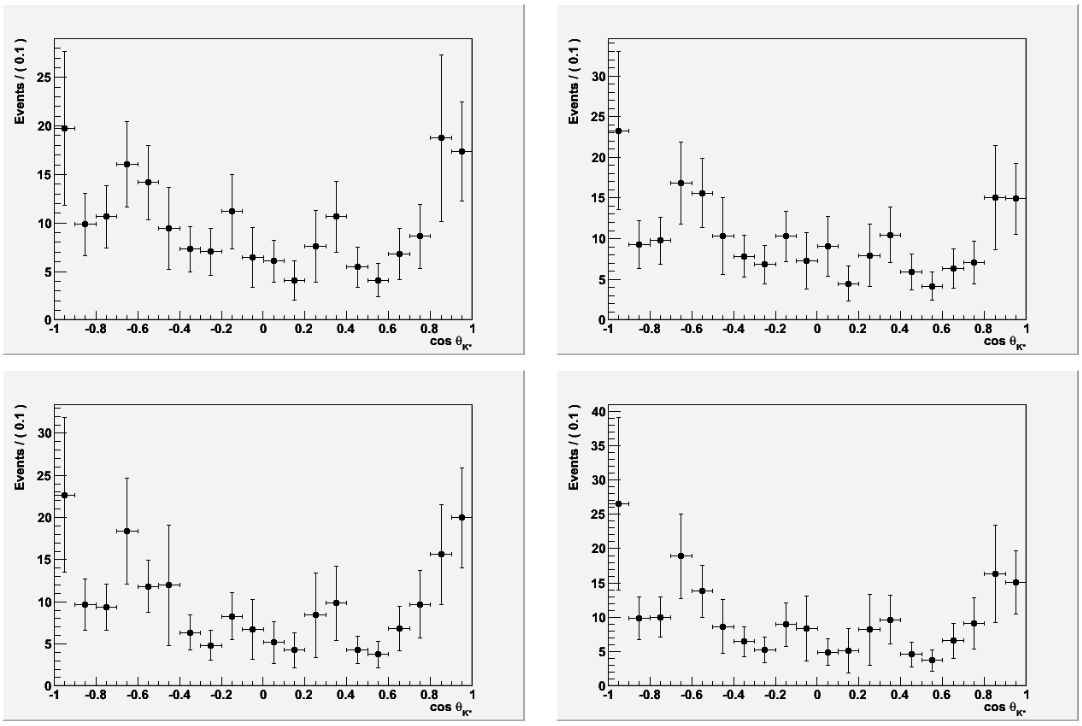

Figure 8.11: One dimensional projection of $B \to K^{*}l^{+}l^{-}$ combinatoric background for $\cos\theta_{K^*}$ for each of the modes in $q0$. Top: $B^{+} \to K_{s}^{0}\pi^{+}\mu^{+}\mu^{-}$ (left), $B^{0} \to K^{+}\pi^{-}\mu^{+}\mu^{-}$ (right). Bottom: $B^{+} \to K_{s}^{0}\pi^{+}e^{+}e^{-}$ (left), $B^{0} \to K^{+}\pi^{-}e^{+}e^{-}$ (right).

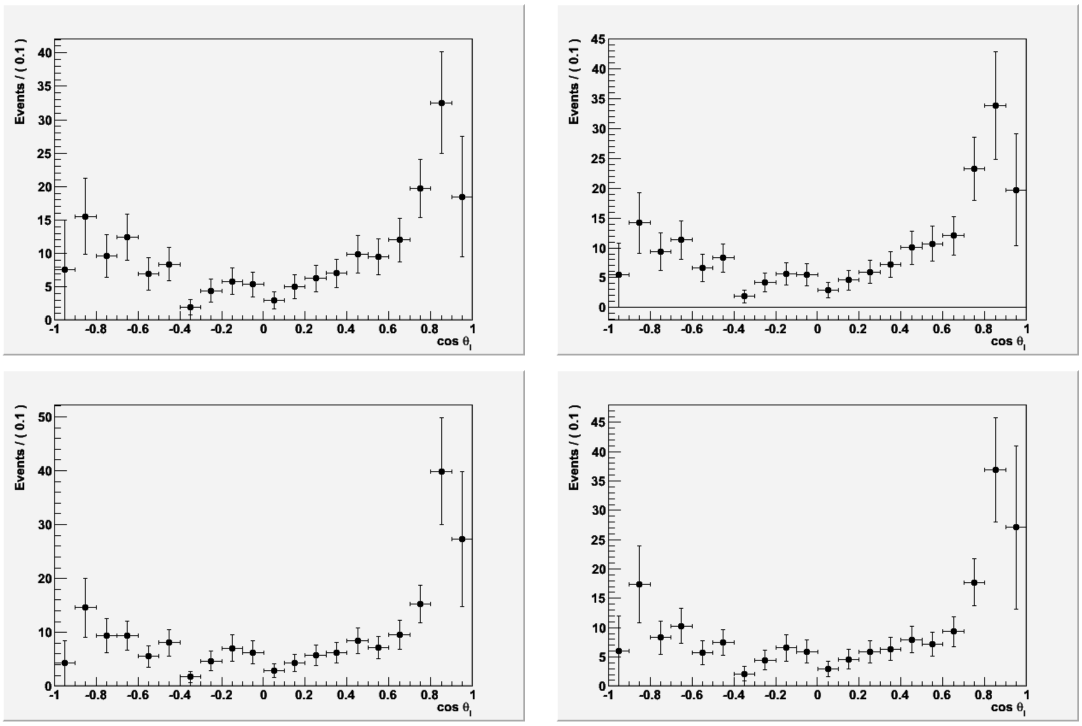

Figure 8.12: One dimensional projection of $B \rightarrow K^{*}l^{+}l^{-}$ combinatoric background for $\cos\theta_l$ for each of the modes in $q0$. Top: $B^{+} \rightarrow K_s^0\pi^{+}\mu^{+}\mu^{-}$ (left), $B^{0} \rightarrow K^{+}\pi^{-}\mu^{+}\mu^{-}$ (right). Bottom: $B^{+} \rightarrow K_s^0\pi^{+}e^{+}e^{-}$ (left), $B^{0} \rightarrow K^{+}\pi^{-}e^{+}e^{-}$ (right).

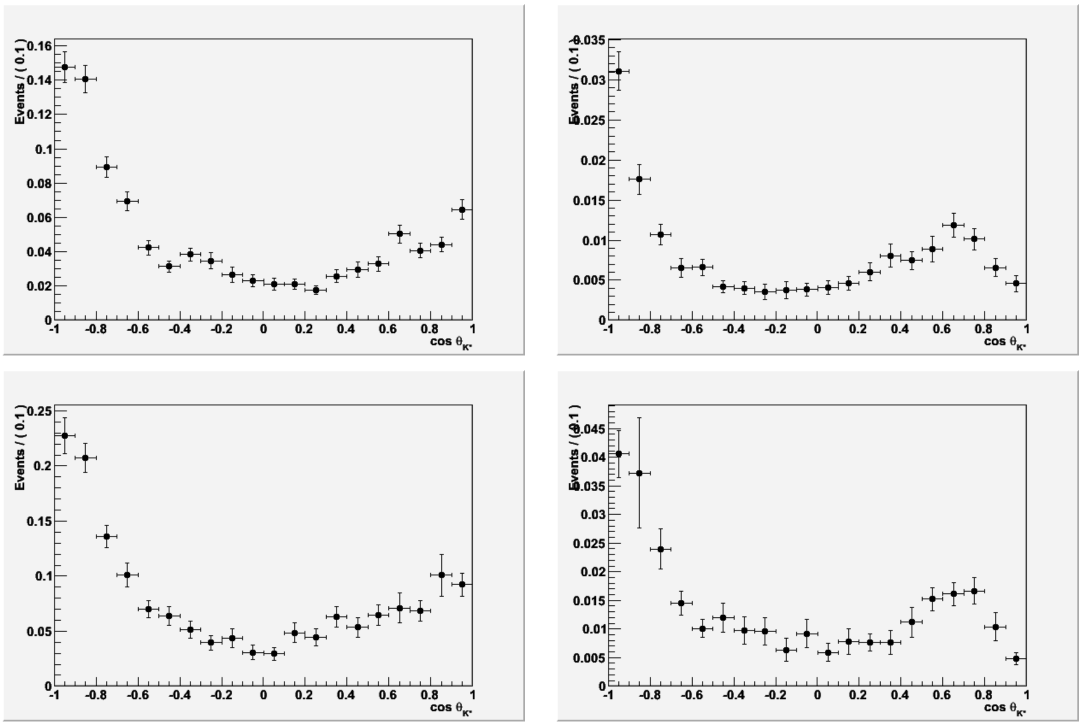

Figure 8.13: One dimensional projection of $B \to K^{*}l^{+}l^{-}$ inclusive crossfeed background for $\cos\theta_{K^{*}}$ for each of the modes in $q0$. Top: $B^{+} \to K_{s}^{0}\pi^{+}\mu^{+}\mu^{-}$ (left), $B^{0} \to K^{+}\pi^{-}\mu^{+}\mu^{-}$ (right). Bottom: $B^{+} \to K_{s}^{0}\pi^{+}e^{+}e^{-}$ (left), $B^{0} \to K^{+}\pi^{-}e^{+}e^{-}$ (right).

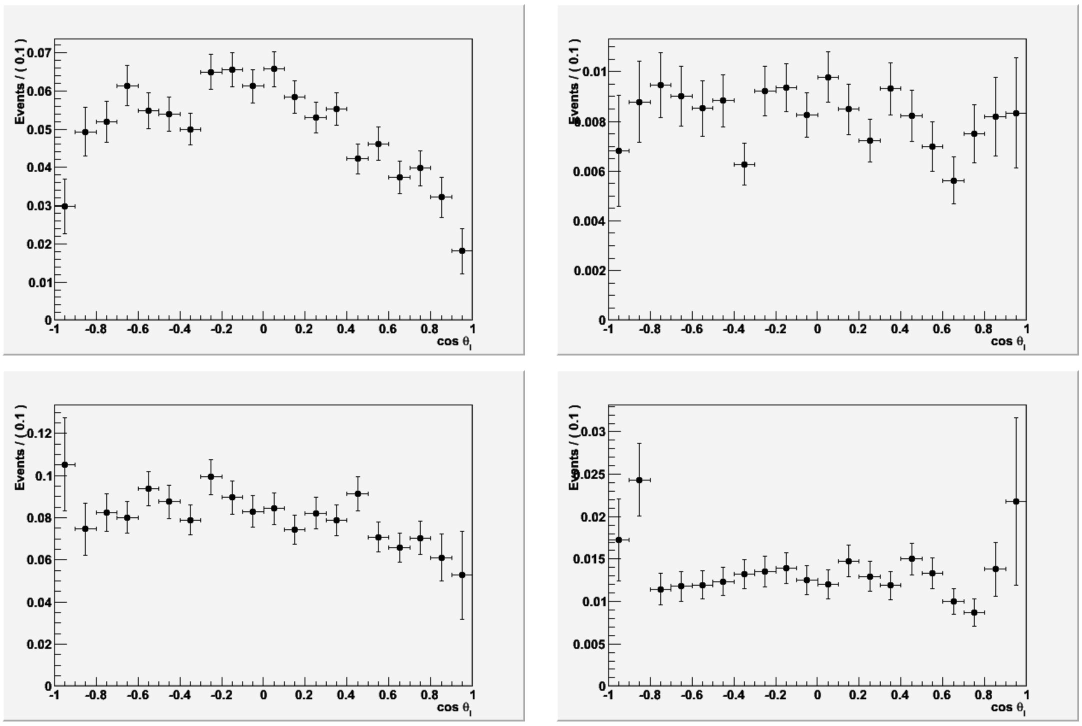

Figure 8.14: One dimensional projection of $B \rightarrow K^{*}l^{+}l^{-}$ inclusive crossfeed background background for $\cos\theta_{l}$ for each of the modes in $q0$. Top: $B^{+} \rightarrow K_{s}^{0}\pi^{+}\mu^{+}\mu^{-}$ (left), $B^{0} \rightarrow K^{+}\pi^{-}\mu^{+}\mu^{-}$ (right). Bottom: $B^{+} \rightarrow K_{s}^{0}\pi^{+}e^{+}e^{-}$ (left), $B^{0} \rightarrow K^{+}\pi^{-}e^{+}e^{-}$ (right).

# Bibliography

[1] (Particle Data Group) W.M. Yao et al. *J. Phys. G,* 33(1), 2006.

[2] S. Weinberg *Phys. Rev. Lett.*, 19(1264), 1967.

[3] A. Salam. *Elementary Particle Physics.* Almquist and Wiksell, Stockholm, 1968.

[4] P.W. Higgs. *Phys. Lett.*, 12(132), 1964.

[5] P.W. Higgs *Phys. Rev.*, 130(439), 1963.

[6] P. Teixeira-Dias. *arXiv:0804.4146*, 2007

[7] N. Krumnack. *arXiv:0910.3353*, 2009.

[8] N. Cabibbo. *Phys. Rev. Lett.*, 10(531), 1963

[9] M. Kabayashi and K. Maskawa. *Progress of Theoretical Physics*, 49(652), 1973.

[10] P.F. Harrison and H.R. Quinn *The BABAR Physics Book*

[11] N. Cabbibo. *Phys. Rev. Lett.*, 10(531), 1963.

[12] M. Kobayashi and T. Maskawa. *Prog. Theor. Phys*, 49(652), 1973.

[13] A. Seiden *Particle Physics, A Comprehensive Introduction* 2005.

[14] D. Griffiths *Introduction into Elementary Particle Physics*

[15] L. Wolfenstein. *Phys. Rev. Lett.*, 51(1945), 1983.

[16] M. Bona et al. (UTfit Collaboration). *JHEP*, 028(0507), 2005.

[17] J. Charles et al. (CKMFitter Collabotation). *Eur. Phys. J. C*, 41(1), 2005.

[18] S.L. Glashow, J.Iliopoulos, and L. Maini. *Phys. Rev. Lett.*, 2(1285), 1970.

[19] Super-Kamiokande *arXiv:1002.3471* [hep-ex].

[20] E. Kh. Akhmedov, G. C. Branco, M. N. Rebelo. *Phys. Lett. B*, 478(215), 2000.

[21] B. Roe *Particle Physics at the New Millennium*

[22] M. B. Gavela, P. Hernandez, J. Orloff, O. Pene. *arXiv:9312215v1* [hep-ph], 1993.

[23] A. H. G. Peter, C. E. Moody and M. Kamionkowski *arXiv:1003.0419* [astro-ph.CO], 2010.

[24] C. Clarkson and C. Zunckel *arXiv:1002.5004* [astro-ph.CO], 2010.

[25] P. Ramond *Journeys Beyond the Standard Model*

[26] M. Kaku and K. Kikkawa *Phys. Rev. D*, 10(1110), 1974.

[27] V. Kaplunovsky *Phys. Rev. Lett.*, 55(1036), 1985.

[28] D. Z. Freedman, P. van Nieuwenhuizen and S. Ferrara *Phys. Rev. D*, 13(3214), 1975.

[29] G. Buchalla, A.J. Buras and M.E. Lautenbacher. *Rev. Mod. Phys.*, 68(1125), 1996.

[30] K.G.Wilson. *Phys. Rev.*, 179(1499), 1969.

[31] K.G. Wilson and W. Zimmermann. *Commun. Math. Phys.*, 24(87), 1972.

[32] W.A. Bardeen, A.J. Buras, D.W. Duke and T.Muta. *Phys. Rev. D*, 18(3998),1978.

[33] N. Isgur and M.B. Wise. *Adv. Ser. Direct. High Energy Phys.*, 10(549), 1992.

[34] A. Ali et al. *Phys. Rev. D*, 66(034002), 2002.

[35] P. Avery et al. (CLEO Collaboration). *Phys. Lett. B*, 223(470), 1989.

[36] R. Ammar et al. (CLEO Collaboration). *Phys. Rev. Lett.*, 71(674), 1993.

[37] S. Anderson et al. (CLEO Collaboration). *Phys. Rev. Lett.*, 87(181803), 2001.

[38] F. Abe et al. (CDF Collaboration). *Phys. Rev. Lett.*, 76(4675), 1996.

[39] T. Affolder et al. (CDF Collaboration). *Phys. Rev. Lett.*, 83(3378), 1999

[40] K. Abe et al. (Belle Collaboration). *Phys. Rev. Lett.*, 88(021801), 2002.

[41] B. Aubert et al. (*BABAR* Collaboration). *Phys. Rev. Lett.*, 91(221802), 2003.

[42] B. Aubert et al. (*BABAR* Collaboration). *Phys. Rev. Lett.*, 91(221801), 2003.

[43] A. Ishikawa et al. (Belle Collaboration). *Phys. Rev. Lett.*, 91(261601), 2003.

[44] P. Koppenburg et al. (Belle Collaboration). *Phys. Rev. Lett.*, 93(061803), 2004.

[45] K. Abe et al. (Belle Collaboration). *Phys. Rev. Lett. B*, 511(151), 2001.

[46] S. Chen et al. (CLEO Collaboration). *Phys. Rev. Lett.*, 87(251801), 2001.

[47] B. Aubert et al. (*BABAR* Collaboration). *Phys. Rev. Lett.*, 93(261601), 2004.

[48] M. Iwasaki et al. (Belle Collaboration). *Phys. Rev. D*, 72(092005), 2005.

[49] *http://www.slac.stanford.edu/xorg/hfag/rare/leppho09/radll/OUTPUT/HTML/kll.html*

[50] G. Buchalla, G. Hiller, and G. Isidori. *Phys. Rev. D*, 63(014015), 2001.

[51] A. Ali et al. *Phys. Rev. D*, 61(074024), 2000.

[52] F. Kruger and J. Matias. *Phys. Rev. D*, 71(094009), 1990.

[53] A. Lipiniacka. *arXiv:hep-ph/0210356*, 2002.

[54] S. Heinemeyer. *arXiv:0906.4677*, 2009.

[55] T. Feldmann and J. Matias. *JHEP*, 0302(074), 2003.

[56] G. Eilam, J.L. Hewett, and T.G. Rizzo. *Phys. Rev. D*, 34(2773), 1986.

[57] C. Bobeth, G.Hiller and G. Piranishvili. *arXiv:0709:4147*, 2007.

[58] T. M. Aliev, A. Ozpineci, and M. Savci. *Eur. Phys. J*, C29(265), 2003.

[59] C. Bobeth et al. *Nucl. Phys. B*, 726(252), 2005.

[60] C. Bobeth, T. Ewerth, F. Kruger, and J. Urban. *Phys. Rev. D*, 64(074014), 2001.

[61] A. Ali, P. Ball, L. T. Handoko and G. Hiller. *Phys. Rev. D*, 61(074024), 2000.

[62] B. Aubert et al. (*BABAR* Collaboration). *Phys. Rev. D*, 72(052004), 2005.

[63] B. Aubert et al. (*BABAR* Collaboration), *Nucl. Inst. Meth.*, A479, 1, 2002.

[64] A. Gritsan and Z. Guo. (*BABAR* Analysis Document 1879)

[65] D.A. Demir and K. Olive. *Phys. Rev. D*, 66(034015), 2002.

[66] D. Asgeirsson and M. Kelsey. (*BABAR* Analysis Document 1677)

[67] D. Bard and R. Barlow. (*BABAR* Analysis Document 1724)

[68] A. Denig and V. Druzhinin. (*BABAR* Analysis Document 1908)

[69] *http://www.slac.stanford.edu/BFROOT/www/Detector/IFR/IFR.html*

[70] S. Agostinelli et al. *Nucl. Inst. and Math.*, 506(3), 2003.

[71] D.L. Lange, *Nucl. Inst. Meth.*, A462, 152, 2001.

[72] Piotr Golonka and Zbigniew Was. *Eur. Phys. J*, C45(1), 2006.

[73] B. Aubert et al. (*BABAR* Collaboration) *Phys. Rev. D*, 79(031102), 2009.

[74] *http://www.slac.stanford.edu/BFROOT/www/Physics/Tools/Pid/PidSelectors/index.htmlperf*

[75] *http://neuralnets.web.cern.ch/NeuralNets/nnwInHep.html*

[76] B. Aubert et al. (*BABAR* Collaboration) *BABAR Analysis Document* 1494v15

[77] G.C. Fox and S. Wolfram. *Phys. Rev. Lett.*, 41(1581), 1978.

[78] A.M. Legendre. *Mm. Math. et Phys.*, 10, 1785.

[79] B. Aubert et al. (*BABAR* Collaboration) *Phys. Rev. D*, 73(092001), 2006.

[80] arXiv:physics/0408124v2 [physics.data-an]

[81] Fred James. *http://www.cern.ch/minuit*, 1978.

[82] ARGUS Collaboration. *Z. Phys.*, C48(543), 1990.

[83] T. Skwarnicki. *Ph.D. Thesis, Institute of Nuclear Physics, Cracow*, (DESY Report No. DESY F31-86-32), 1986.

[84] Y. Xie, P. Clarke, G. Cowan and F Muheim. *JHEP 0909:074*, 2009.

[85] B. Aubert et al. (*BABAR* Collaboration) *Phys. Rev. D*, 76(032002), 2007.

[86] B. Aubert et al. (*BABAR* Collaboration) *Phys. Rev. D79: 031102*, 2009.

[87] J. -T. Wei, P. Chang, et al (The Belle Collaboration) *Phys.Rev.Lett.103:171801*, 2009.

[88] T. Aaltonen, et al. (The CDF Collaboration) *Phys. Rev. D79, 011104(R)*, 2009.

[89] W. Reece and U. Egede *LHCb Note* LHCb-2008-041

[90] S. Gadomski. *ALT-CONF-2002-007*, 2002.

[91] The CMS Collaboration. *J. Phys. G: Nucl. Part. Phys. 34 995*, 2007.

[92] SuperB Collaboration. *arXiv:0709.0451*, 2007.

[93] B. Aubert et al. (*BABAR* Collaboration) *BABAR Analysis Document* 2182